

UNIVERSITY OF SOUTHAMPTON

**Disc Winds Matter: Modelling
Accretion and Outflow on All Scales**

by

James Matthews

A thesis submitted in partial fulfillment for the
degree of Doctor of Philosophy

in the
Faculty of Physical Sciences and Engineering
Department of Physics & Astronomy

May 2016

“Here, on the edge of what we know, in contact with the ocean of the unknown, shines the mystery and the beauty of the world.

And it’s breathtaking.”

Seven Brief Lessons on Physics, Carlo Rovelli

“Good enough for government work.”

Christian Knigge

UNIVERSITY OF SOUTHAMPTON

Abstract

Faculty of Physical Sciences and Engineering
Department of Physics & Astronomy

Doctor of Philosophy

by James Matthews

Outflows are ubiquitous in accreting systems across 10 orders of magnitude in mass. They can take the form of highly collimated radio jets, or less collimated, mass loaded winds emanating from the accretion disc. Perhaps the most spectacular evidence for accretion disc winds is the blue-shifted, broad absorption lines (BALs) in UV resonance lines, seen in cataclysmic variables (CVs) and approximately 20% of quasars. In addition to directly producing absorption in the spectrum, it is possible that accretion disc winds may significantly affect the line and continuum *emission* from CVs and quasars – as a result, they may even dominate the spectral appearance of such objects. When one considers that disc winds are also a possible mechanism for AGN feedback, it becomes clear that understanding the physics and true spectral imprint of these winds is of wide-ranging astrophysical significance.

In this thesis I use the confusingly named Monte Carlo radiative transfer (MCRT) code, PYTHON, to conduct a series of MCRT and photoionization simulations designed to test simple biconical disc wind models. I provide a detailed description of these methods, focusing particularly on the macro-atom implementation developed by Leon Lucy. First, I apply them to the optical spectra of CVs. Second, I conduct tests of quasar unification models. Finally, informed by the previous study, I use Sloan Digital Sky Survey and Hubble Space Telescope data to test the models in an empirical way, by using emission line equivalent widths as a probe of unification geometries.

Overall, the work presented here suggests that *disc winds matter*. They not only act as a spectral ‘filter’ for the underlying accretion continuum, but may actually dominate the emergent spectrum from accreting objects. As a result, unveiling their driving mechanisms, mass-loss rates, and ionization structure is an important goal for the astronomical community.

Contents

Abstract	ii
List of Figures	v
List of Tables	vii
1 The Impact of Accretion Disc Winds on the Optical Spectra of Cataclysmic Variables	1
1.1 Introduction	1
1.1.1 Sources and Sinks of Radiation	2
1.1.1.1 Accretion disc	3
1.1.1.2 White Dwarf	3
1.1.1.3 Boundary Layer	4
1.1.1.4 Secondary Star	4
1.2 A Benchmark disc Wind Model	5
1.2.1 Physical Structure and Ionization State	6
1.2.2 Synthetic Spectra	7
1.3 A Revised Model Optimized for Optical Wavelengths	11
1.3.1 Synthetic Spectra	12
1.3.2 Continuum Shape and the Balmer Jump	15
1.3.3 Line Profile Shapes: Producing Single-Peaked Emission	17
1.3.4 Sensitivity to Model Parameters	19
1.3.5 Comparison to RW Tri	19
1.4 Discussion: Collision Strengths and Boundary Layers	21
1.4.1 Model Sensitivity to Collision Strengths	21
1.4.1.1 Collisions Between Radiatively Forbidden Transitions . .	21
1.4.1.2 Line Heating and Cooling	21
1.4.2 Improving Collision Strengths	22
1.4.3 Introducing a Boundary Layer	22
1.5 Conclusions	22
2 Testing Quasar Unification: Radiative Transfer In Clumpy Winds	24
2.1 Introduction	24
2.2 A Clumpy Biconical Disk Wind Model for Quasars	25
2.2.1 Photon Sources	25

2.2.2	A Simple Approximation for Clumping	27
2.2.3	The Simulation Grid	30
2.3	Results and Analysis From A Fiducial Model	31
2.3.1	Physical Conditions and Ionization State	31
2.3.2	Synthetic Spectra: Comparison to Observations	34
2.3.2.1	Broad absorption lines ('BALQSO-like' angles)	36
2.3.2.2	Broad emission lines ('quasar-like' angles)	39
2.3.3	X-ray Properties	40
2.3.4	LoBALs and Ionization Stratification	41
2.4	Discussion	43
2.4.1	Parameter Sensitivity	43
2.4.2	Inclination Trends: FWHM and EW	43
2.4.2.1	FWHM and Black Hole Mass Estimates	46
2.5	Summary And Conclusions	47
3	Quasar Emission Lines as Probes of Orientation and Unification	49
3.1	Introduction	49
3.2	Data Sample	50
3.3	The Angular Distribution of Emission from an Accretion Disc	54
3.3.1	Standard Thin Disc Models	54
3.3.2	Including GR, Comptonisation and Opacity Effects	55
3.4	Predicted EW Distributions Compared to Observations	55
3.4.1	Fitting the Quasar Distribution	55
3.4.2	A Monte Carlo Approach	57
3.4.3	EW[O III] in LoBAL quasars	61
3.4.4	Broad Emission Lines in HiBAL quasars	62
3.5	Discussion	62
3.5.1	Eigenvector 1	65
3.5.2	Radio Observations	66
3.5.3	Polarisation	67
3.5.4	Theoretical Considerations	67
3.6	Conclusions	69
4	Conclusions and Future Work	71
4.1	Suggestions for Future Work	72
4.1.1	CVs as Accretion and Outflow Laboratories	72
4.1.2	Improving the Treatment of Clumping	72
4.1.3	Expanding the Capabilities of PYTHON	72
4.1.4	Obtaining Reliable Orientation Indicators	72
4.2	Closing Remarks	72
Bibliography		73

List of Figures

1.1	Cartoon illustrating the geometry and kinematics of the benchmark CV wind model.	2
1.2	The spectral energy distribution of the accretion disc and white dwarf used in the ionization cycles for the CV modelling.	4
1.3	The physical properties of the wind in the benchmark CV model.	6
1.4	UV and optical synthetic spectra from the benchmark CV model	8
1.5	Optical synthetic spectra from the benchmark CV model divided by the continuum.	10
1.6	Total packet-binned spectra across all viewing angles from the benchmark CV model.	11
1.7	UV and optical synthetic spectra from CV model B	13
1.8	Optical synthetic spectra from CV model B divided by the continuum.	16
1.9	Total packet-binned spectra across all viewing angles from CV model B.	17
1.10	$H\alpha$ line profiles from CV models A, B and X	18
1.11	In and out of eclipse spectra from model B compared to the high inclination NL RW Tri	20
2.1	A cartoon showing the geometry and some key parameters of the biconical quasar wind model.	26
2.2	The input spectrum used for the quasar modelling.	27
2.3	Some typical length scales for the fiducial model.	29
2.4	Contour plots showing the logarithm of some important physical properties of the quasar outflow.	32
2.5	The electron density in the fiducial model on linear axes.	33
2.6	Synthetic spectra at four viewing angles for the fiducial quasar model.	35
2.7	A schematic showing the broad classes of sightline in the fiducial model.	36
2.8	Synthetic spectra at two viewing angles compared to the non-BAL SDSS quasar composite.	37
2.9	X-ray properties of the clumped quasar model compared to H13 and samples from the literature.	40
2.10	$C\text{ IV}$, $Mg\text{ II}$, $Al\text{ III}$ and $Fe\text{ II}$ line profiles for wind viewing angles.	42
2.11	Equivalent widths and BALnicities of some important lines for the quasar wind grid.	44
2.12	$W_{\lambda,RW}$ as a function of inclination in the fiducial model.	45
2.13	f_{FWHM} as a function of inclination	47
3.1	BH mass and Eddington fraction for the BAL samples plotted over the overall quasar sample from S11.	51

3.2	Histograms of equivalent widths for three emission lines from the two different samples.	52
3.3	Monochromatic continuum luminosities from AGNSPEC and classical thin disc models.	56
3.4	EW distribution	58
3.5	The EW distribution of quasars in the R11 sample (red errorbars) and the best fit model with a maximum viewing angle of 84°	59
3.6	The geometry of the toy model used to carry out the Monte Carlo simulations	60
3.7	Contour plots from the Monte Carlo simulations.	62
3.8	Contour plots from the Monte Carlo simulations.	63
3.9	Contour plots from the Monte Carlo simulations.	64
3.10	Eigenvector 1 for BAL and non-BAL quasars.	66
3.11	LoBAL fraction compared to mean LoBAL fraction in Eigenvector 1 space.	67
3.12	<i>Top:</i> Polarisation percentages as a function of measured inclination from Marin et al. (2015) for Type I and Type II AGN. <i>Bottom:</i> Histograms of polarisation percentages for BAL quasars from Schmidt et al. (1999) together with the Marin et al. (2015) AGN sample.	68

List of Tables

1.1	Model parameters for the CV wind models	5
2.1	The grid points used in the parameter search for quasar wind models	31
2.2	Model parameters for the fiducial quasar model.	33
2.3	Some derived spectral properties of the fiducial model compared to observations.	38
3.1	Eigenvector 1 correlation coefficients	65

Dedicated to my family. Thanks for being awesome....

Chapter 1

The Impact of Accretion Disc Winds on the Optical Spectra of Cataclysmic Variables

This chapter is based on the publication:

Matthews J. H., Knigge C., Long K. S., Sim S. A., Higginbottom N., ‘The impact of accretion disc winds on the optical spectra of cataclysmic variables’, 2015, MNRAS, 450, 3331.

Due to the collaborative nature of the papers in this thesis, the reader will notice a switch of pronouns for the next three chapters.

1.1 Introduction

Here, I present Monte Carlo radiative transfer simulations designed to assess the likely impact of accretion disc winds on the optical spectra of high-state CVs. More specifically, the goal is to test whether disc winds of the type developed to account for the UV resonance lines would also naturally produce significant amounts of optical line and/or continuum emission. In order to achieve this, I use the ‘macro-atom’ approach described in chapter 3 into the Monte Carlo ionization and radiative transfer code PYTHON. With

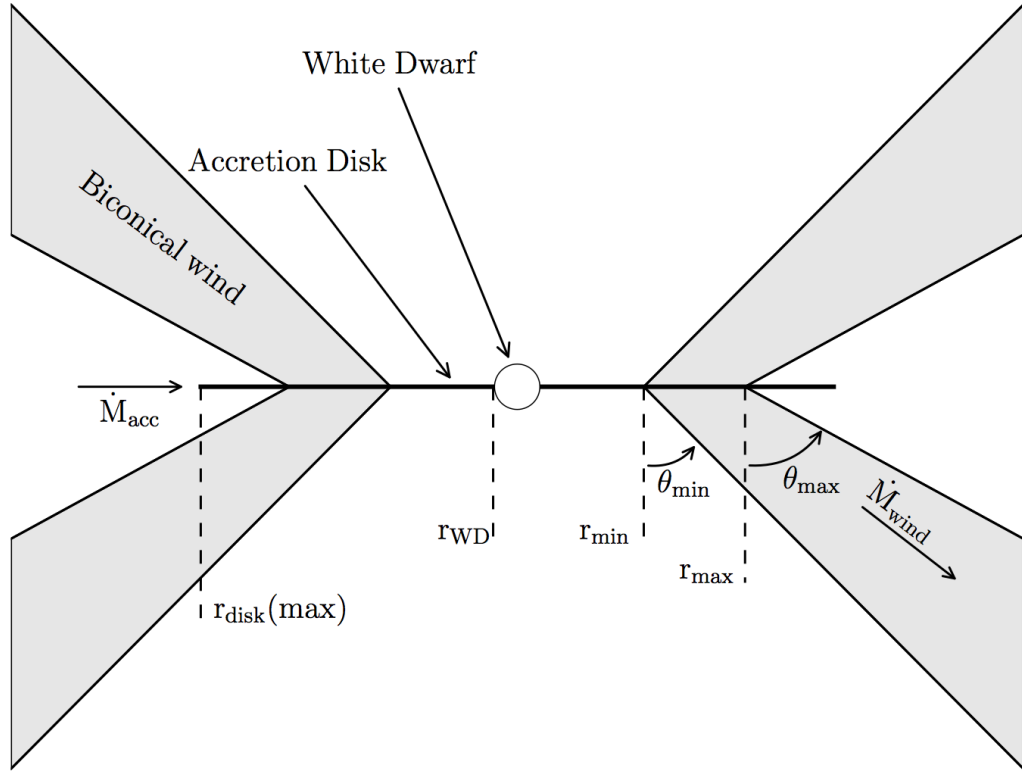


FIGURE 1.1: Cartoon illustrating the geometry and kinematics of the benchmark CV wind model.

this upgrade, the code is able to deal correctly with processes involving excited levels, such as the recombination emission produced by CV winds.

The remainder of this paper is organized as follows. In Section 2, we briefly describe the code and the newly implemented macro-atom approach. In Section 3, we describe the kinematics and geometry of our disc wind model. In Section 4, we present spectra simulated from the benchmark model employed by LK02, and, in Section 5, we present a revised model optimized for the optical waveband. In Section 6, we summarize our findings.

1.1.1 Sources and Sinks of Radiation

The net photon sources in our CV model are the accretion disc, the WD and, in principle, a boundary layer with user-defined temperature and luminosity. All of these radiating bodies are taken to be optically thick, and photons striking them are assumed to be destroyed instantaneously. The secondary star is not included as a radiation source, but

is included as an occulting body. This allows us to model eclipses. Finally, emission from the wind itself is also accounted for, but note that this assumes the outflow is in radiative equilibrium. Thus all of the heating of the wind, as well as its emission, is ultimately powered by the radiation field of the net photon sources in the simulation. In the following sections, we will describe our treatment of these system components in slightly more detail.

1.1.1.1 Accretion disc

PYTHON has some flexibility when treating the accretion disc as a source of photons. The disc is broken down into annuli such that each annulus contributes an equal amount to the bolometric luminosity. We take the disc to be geometrically thin, but optically thick, and thus adopt the temperature profile of a standard [Shakura & Sunyaev \(1973\)](#) α -disc. An annulus can then be treated either as a blackbody with the corresponding effective temperature or as a stellar atmosphere model with the appropriate surface gravity and effective temperature. Here, blackbodies are used during the ionization cycles and to compute our Monte Carlo estimators. The input SED for the ionization cycles is shown in Fig. ?? However, during the spectral synthesis stage of the simulation stellar atmosphere models are used. This produces more realistic model spectra and allows us to test if recombination emission from the wind base can fill in the Balmer jump, which is always in absorption in these models. Our synthetic stellar atmosphere spectra are calculated with SYNSPEC¹ from either Kurucz ([Kurucz 1991](#)) atmospheres (for $T_{eff} \leq 50,000$ K) or from TLUSTY ([Hubeny & Lanz 1995](#)) models (for $T_{eff} > 50,000$ K).

1.1.1.2 White Dwarf

The WD at the center of the disc is always present as a spherical occulting body with radius R_{WD} in PYTHON CV models, but it can also be included as a source of radiation. In the models presented here, the WD is treated as a blackbody radiator with temperature T_{WD} and luminosity $L_{WD} = 4\pi R_{WD}^2 \sigma T_{WD}^4$.

¹<http://nova.astro.umd.edu/Synspec43/synspec.html>

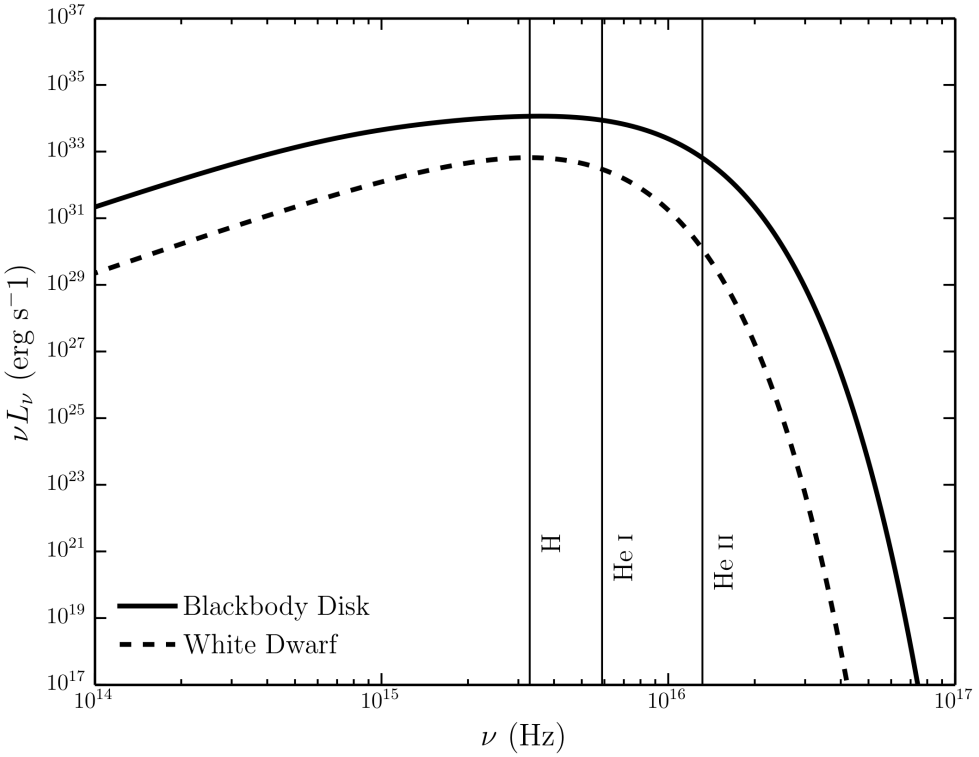


FIGURE 1.2: The spectral energy distribution of the accretion disc and white dwarf used in the ionization cycles for the CV modelling.

1.1.1.3 Boundary Layer

It is possible to include radiation from a boundary layer (BL) between the disc and the WD. In PYTHON, the BL is described as a blackbody with a user-specified effective temperature and luminosity. The models presented here initially follow LK02 in setting the BL luminosity to zero. However, the influence of the BL on the heating and cooling balance in the wind, as well as the emergent spectrum, is discussed further in section 1.4.

1.1.1.4 Secondary Star

The donor star is included in the system as a pure radiation sink, i.e. it does not emit photons, but absorbs any photons that strike its surface. The secondary is assumed to be Roche-lobe filling, so its shape and relative size are defined by setting the mass ratio of the system, $q = M_2/M_{WD}$. The inclusion of the donor star as an occulting body allows us to model eclipses of the disc and the wind. For this purpose, we assume a

Parameter	Model Parameters	
	Model A	Model B
M_{WD}	$0.8 M_{\odot}$	
R_{WD}	7×10^8 cm	
T_{WD}	40,000 K	
M_2	-	$0.6 M_{\odot}$
q	-	0.75
P_{orb}	-	5.57 hr
a	-	$194.4 R_{WD}$
R_2	-	$69.0 R_{WD}$
\dot{M}_{acc}	$10^{-8} M_{\odot} yr^{-1}$	
\dot{M}_{wind}	$10^{-9} M_{\odot} yr^{-1}$	
r_{min}	$4 R_{WD}$	
r_{max}	$12 R_{WD}$	
$r_{disc}(\text{max})$	$34.3 R_{WD}$	
θ_{min}	20.0°	
θ_{max}	65.0°	
γ	1	
v_{∞}	$3 v_{esc}$	
R_v	$100 R_{WD}$	$142.9 R_{WD}$
α	1.5	4

TABLE 1.1: Parameters used for the geometry and kinematics of the benchmark CV model (model A), which is optimized for the UV band, and a model which is optimized for the optical band and described in section 5 (model B). For model B, only parameters which are altered are given - otherwise the model A parameter is used. P_{orb} is the orbital period (the value for RW Tri from Walker 1963 is adopted, see section 5.4) and R_2 is the radius of a sphere with the volume of the secondary's Roche lobe. Other quantities are defined in the text or Fig. 1.2. Secondary star parameters are only quoted for model B as we do not show eclipses with the benchmark model (see section 5.4).

circular orbit with a semi-major axis a and specify orbital phase such that $\Phi_{orb} = 0$ is the inferior conjunction of the secondary (i.e. mid-eclipse for $i \simeq 90^\circ$).

1.2 A Benchmark disc Wind Model

Our main goal is to test whether the type of disc wind model that has been successful in explaining the UV spectra of CVs could also have a significant impact on the optical continuum and emission line spectra of these systems. In order to set a benchmark, we therefore begin by investigating one of the fiducial CV wind models that was used by SV93 and LK02 to simulate the UV spectrum of a typical high-state system. The specific parameters for this model (model A) are listed in Table 1. A key point is that the wind mass-loss rate in this model is set to 10% of the accretion rate through the disc.

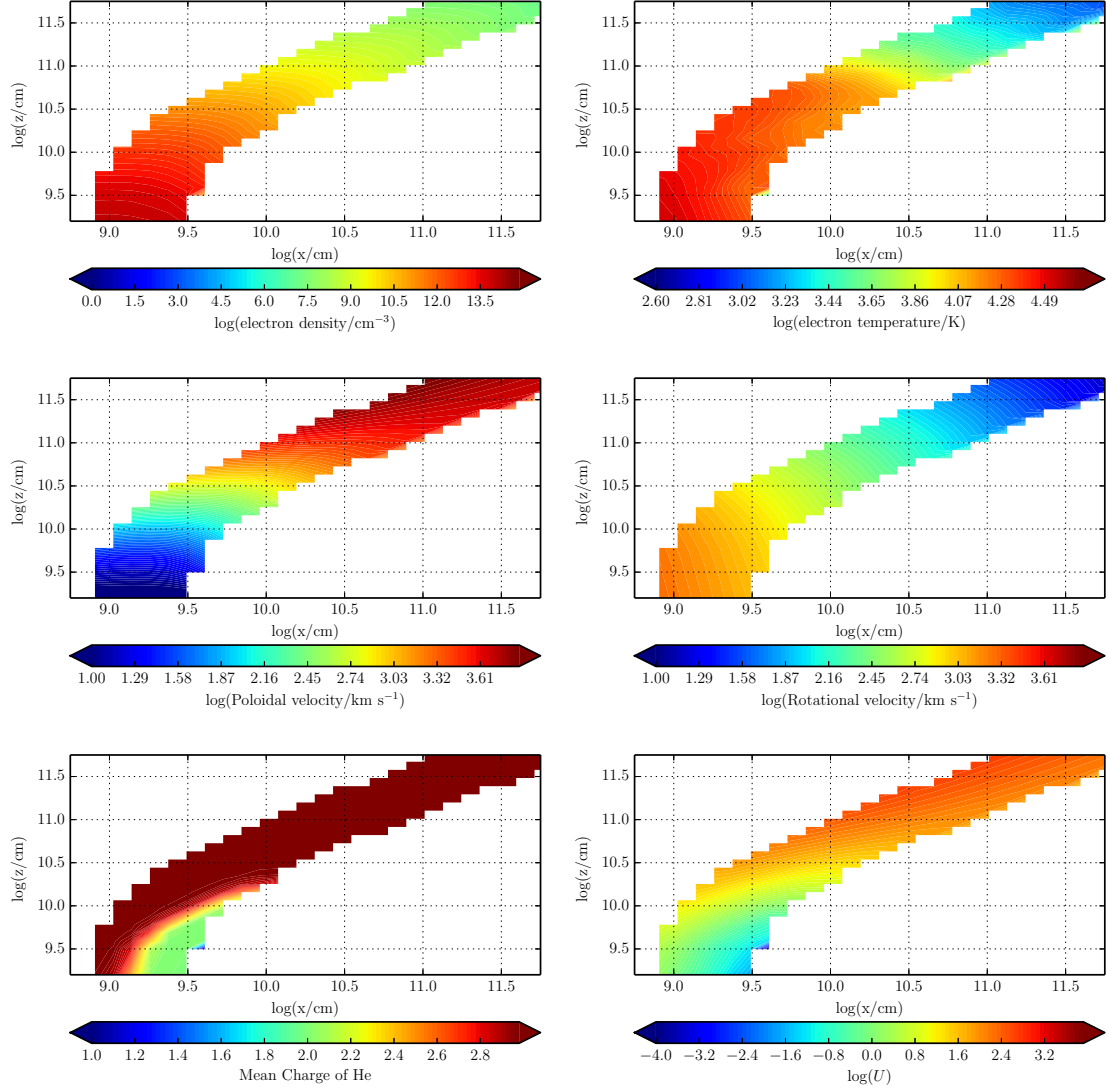


FIGURE 1.3: The physical properties of the wind – note the logarithmic scale. Near the disc plane the wind is dense, with low poloidal velocities. As the wind accelerates it becomes less dense and more highly ionized. The dominant He ion is almost always He III, apart from in a small portion of the wind at the base, which is partially shielded from the inner disc.

We follow SV93 in setting the inner edge of the wind (r_{min}) to $4 R_{WD}$. The sensitivity to some of these parameters is briefly discussed in section 5.

1.2.1 Physical Structure and Ionization State

Fig. 1.3 shows the physical and ionization structure of the benchmark disc wind model. The ionization parameter shown in the bottom right panel is given by equation ?? The ionization parameter is a useful measure of the ionization state of a plasma, as it evaluates the ratio of the number density of ionizing photons to the local H density.

There is an obvious drop-off in density and temperature with distance away from the disc, so any line formation process that scales as ρ^2 – i.e. recombination and collisionally excited emission – should be expected to operate primarily in the dense base of the outflow. Moreover, a comparison of the rotational and poloidal velocity fields shows that rotation dominates in the near-disc regime, while outflow dominates further out in the wind.

The ionization equation used in the ‘simple atom’ approach used by LK02 (see section ??) should be a reasonable approximation to the photoionization equilibrium in the benchmark wind model. Even though the macro-atom treatment of H and He does affect the computation of the overall ionization equilibrium, we would expect the resulting ionization state of the wind to be quite similar to that found by LK02. The bottom panels in Fig. 1.3 confirm that this is the case. In particular, He is fully ionized throughout most of the outflow, except for a small region near the base of the wind, which is shielded from the photons produced by the hot inner disc. In line with the results of LK02, CIV is the dominant C ion throughout the wind, resulting in a substantial absorbing column across a large range of velocities. As we shall see, this produces the broad, deep and blue-shifted CIV $\lambda 1550$ absorption line that is usually the most prominent wind-formed feature in the UV spectra of low-inclination nova-like CVs.

1.2.2 Synthetic Spectra

We begin by verifying that the benchmark model still produces UV spectra that resemble those observed in CVs. We do expect this to be the case, since the ionization state of the wind has not changed significantly from that computed by LK02 (see section 1.2.1). The left column of panels in Fig. 1.4 shows that this expectation is met: all of the strong metal resonance lines – notably N V $\lambda 1240$, Si IV $\lambda 1400$ and C IV $\lambda 1550$ – are present and exhibit clear P-Cygni profiles at intermediate inclinations. In addition, however, we now also find that the wind produces significant Ly α and He II $\lambda 1640$ emission lines.

Fig. 1.4 (right-hand panel) and Fig. 1.5 show the corresponding optical spectra produced for the benchmark model, and these do exhibit some emission lines associated with H and He. We see a general trend from absorption lines to emission lines with increasing inclination, as one might expect from our wind geometry. This trend is consistent with observations, as can be seen in Fig. 1. However, it is clear that this particular

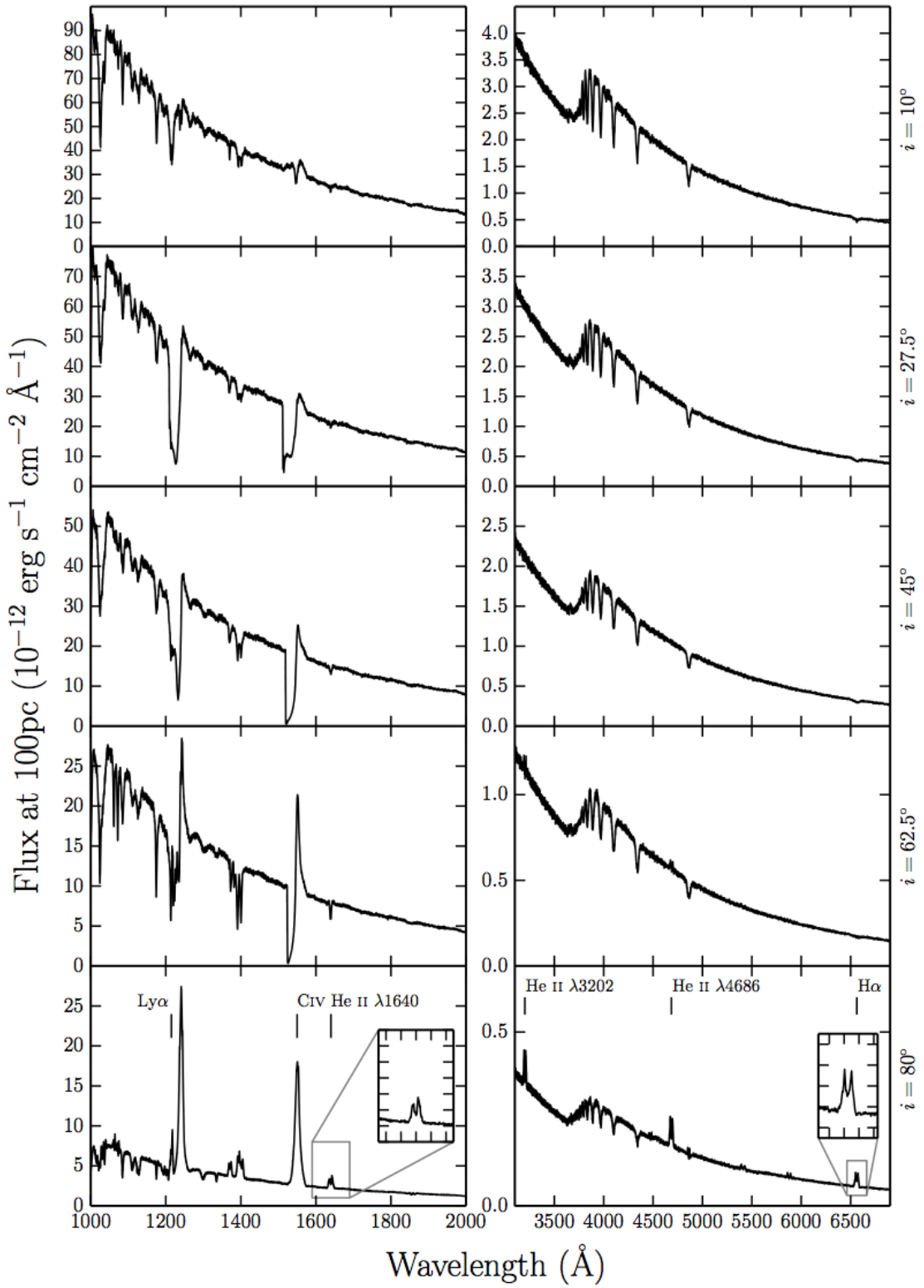


FIGURE 1.4: UV (left) and optical (right) synthetic spectra for model A, our benchmark model, computed at sightlines of 10, 27.5, 45, 62.5 and 80 degrees. The inset plots show zoomed-in line profiles for He II $\lambda 1640$ and H α . Double-peaked line emission can be seen in He II $\lambda 1640$, He II $\lambda 4686$, H α and some He I lines, but the line emission is not always sufficient to overcome the absorption cores from the stellar atmosphere models.

The model also produces a prominent He II $\lambda 3202$ line at high inclinations.

model does not produce all of the lines seen in observations of high-state CVs. The higher-order Balmer series lines are too weak to overcome the intrinsic absorption from the disc atmosphere, and the wind fails to produce any observable emission at low and intermediate inclinations. This contrasts with the fact that emission lines are seen in the optical spectra of (for example) V3885 Sgr ([Hartley et al. 2005](#)) and IX Vel ([Beuermann & Thomas 1990](#), see also Fig. 1).

The emissivity of these recombination features scales as ρ^2 , meaning that they form almost entirely in the dense base of the wind, just above the accretion disc. Here, the velocity field of the wind is still dominated by rotation, rather than outflow, which accounts for the double-peaked shape of the lines. In principle, lines formed in this region can still be single peaked, since the existence of a poloidal velocity *gradient* changes the local escape probabilities (MC96). However, as discussed further in section 5.3, the radial velocity shear in our models is not high enough for this radiative transfer effect to dominate the line shapes.

The Balmer jump is in absorption at all inclinations for our benchmark model. This is due to the stellar atmospheres used to model the disc spectrum; it is not a result of photoabsorption in the wind. In fact, the wind spectrum exhibits the Balmer jump in *emission*, but this is not strong enough to overcome the intrinsic absorption edge in the disc spectrum. This is illustrated in Fig. 1.6, which shows the angle-integrated spectrum of the system, i.e. the spectrum formed by all escaping photons, separated into the disc and wind contributions. Even though the wind-formed Balmer recombination continuum does not completely fill in the Balmer absorption edge in this model, it does already contribute significantly to the total spectrum. This suggests that modest changes to the outflow kinematics might boost the wind continuum and produce emergent spectra with weak or absent Balmer absorption edges.

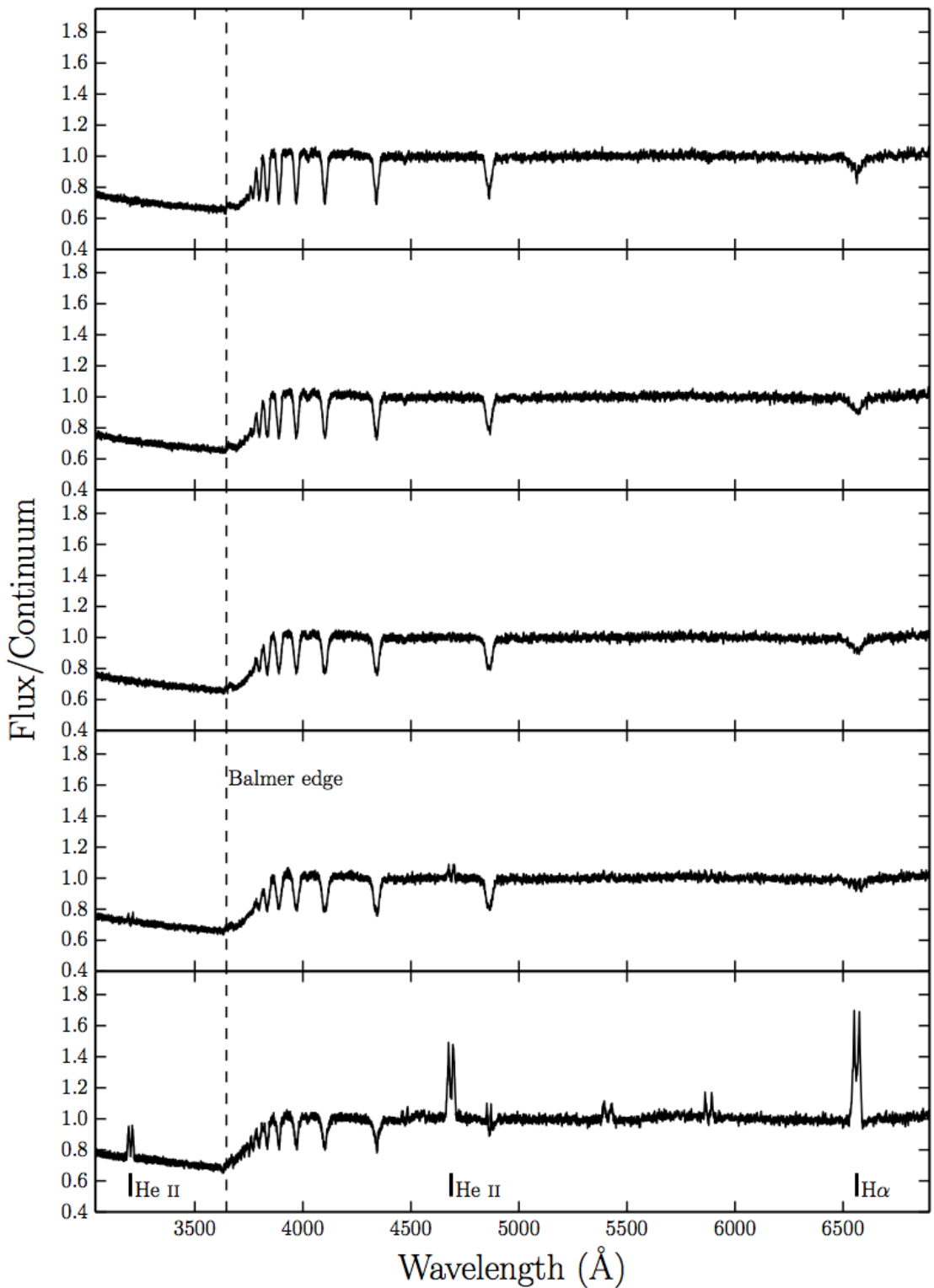


FIGURE 1.5: Synthetic optical spectra from model A computed for sightlines of 10, 27.5, 45, 62.5 and 80 degrees. In these plots the flux is divided by a polynomial fit to the underlying continuum redward of the Balmer edge, so that line-to-continuum ratios and the true depth of the Balmer jump can be shown.

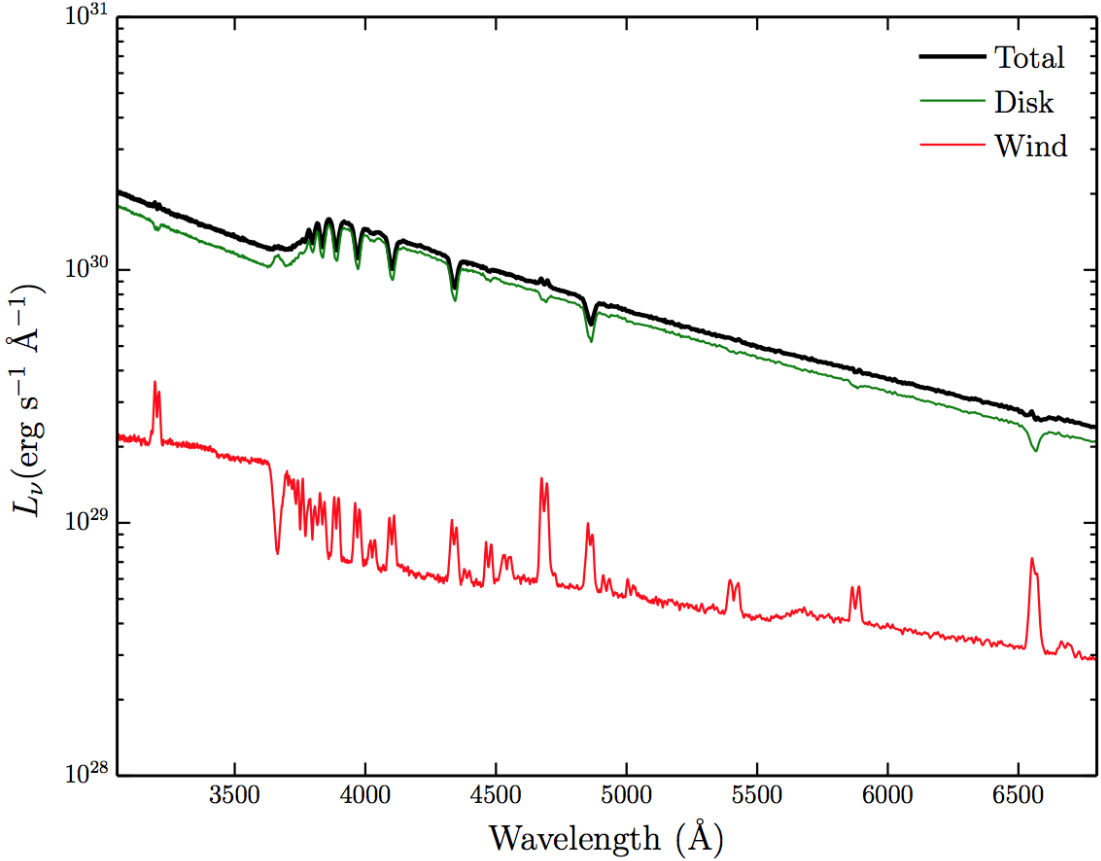


FIGURE 1.6: Total packet-binned spectra across all viewing angles, in units of monochromatic luminosity. The thick black line shows the total integrated escaping spectrum, while the green line shows disc photons which escape without being reprocessed by the wind. The red line show the contributions from reprocessed photons. Recombination continuum emission blueward of the Balmer edge is already prominent relative to other wind continuum processes, but is not sufficient to fill in the Balmer jump in this specific model

1.3 A Revised Model Optimized for Optical Wavelengths

The benchmark model discussed in section 1.2 was originally designed to reproduce the wind-formed lines seen in the UV spectra of high-state CVs. This model does produce some observable optical emission, but we can now attempt to construct a model that more closely matches the observed optical spectra of CVs.

Specifically, we aim to assess whether a revised model can:

- account for all of the lines seen in optical spectra of CVs while preserving the UV behaviour;
- produce single-peaked Balmer emission lines;

- generate enough of a wind-formed recombination continuum to completely fill in the disc’s Balmer absorption edge for reasonable outflow parameters.

The emission measure of a plasma is directly proportional to its density. The simplest way to simultaneously affect the density in the wind (for fixed mass-loss rate), as well as the velocity gradients, is by modifying the poloidal velocity law. Therefore, we focus on just two kinematic variables:

- the acceleration length, R_v , which controls the distance over which the wind accelerates to $\frac{1}{2} v_\infty$;
- the acceleration exponent, α , which controls the rate at which the poloidal velocity changes near R_v .

The general behaviour we might expect is that outflows with denser regions near the wind base – i.e. winds with larger R_v and/or larger α – will produce stronger optical emission signatures. However, this behaviour may be moderated by the effect of the increasing optical depth through this region, which can also affect the line profile shapes. In addition, modifying R_v also increases the emission *volume*. Based on a preliminary exploration of models with different kinematics, we adopt the parameters listed in table 1.1 for our ‘optically optimized’ model (model B).

1.3.1 Synthetic Spectra

Fig. 1.7 shows the UV and optical spectra for the optically optimized model for the full range of inclinations. As expected, the trend from absorption to emission in the optical is again present, but in this revised model emission lines in the entire Balmer series are produced at high inclinations, as well as the observed lines in He II and He I. This can be seen more clearly in the continuum-normalized spectrum in Fig. 1.8.

Two other features are worth noting in the optical spectrum. First, the collisionally excited Ca II emission line at 3934 Å becomes quite prominent in our densest models. Second, our model predicts a detectable He II recombination line at 3202 Å. This is the He equivalent of Paschen β and should be expected in all systems that feature a strong He II $\lambda 4686$ line (the He equivalent of Paschen α). This line is somewhat unfamiliar

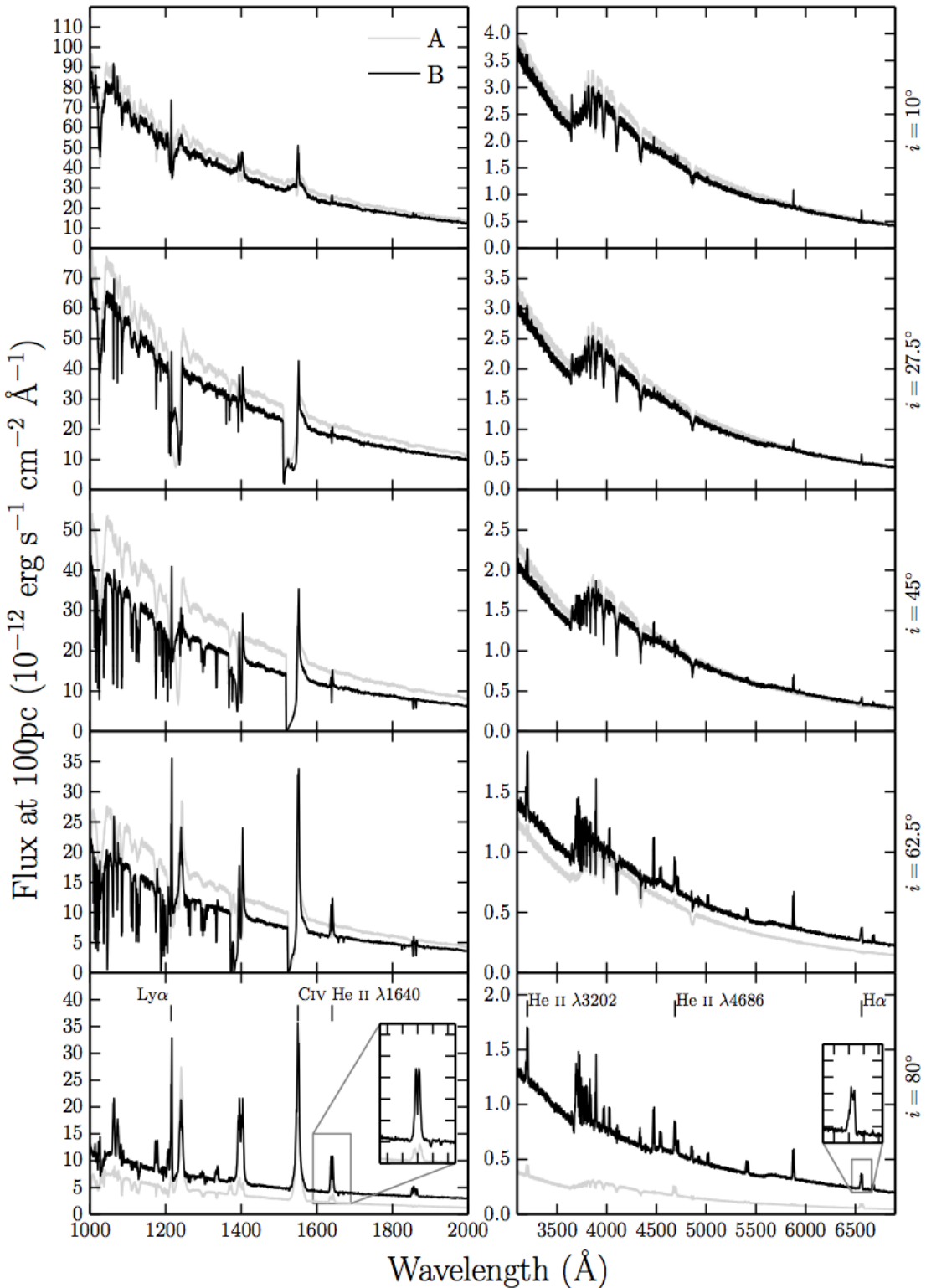


FIGURE 1.7: UV (left) and optical (right) synthetic spectra for model B computed at sightlines of 10, 27.5, 45, 62.5 and 80 degrees. Model A is shown in grey for comparison. The inset plots show zoomed-in line profiles for He II $\lambda 1640$ and H α . The Balmer and He are double-peaked, albeit with narrower profiles. Strong He II $\lambda 4686$ emission can be seen, as well as a trend of a deeper Balmer jump with decreasing inclination.

observationally, because it lies bluewards of the atmospheric cut-off, but also redwards of most ultraviolet spectra.

Our models do not exhibit P-Cygni profiles in the optical lines. This is perhaps not surprising. LK02 and SV93 originally designed such models to reproduce the UV line profiles. Thus, most of the wind has an ionization parameter of $\log U \sim 2$ (see Fig. 1.3). This means H and He are fully ionized throughout much of the wind and are successful in producing recombination features. However, the line opacity throughout the wind is too low to produce noticeable blue shifted absorption. We suspect that the systems that exhibit such profiles must possess a higher degree of ionization stratification, although the lack of contemporary observations means it is not known for certain if the P-Cygni profiles in UV resonance lines and optical H and He lines exist simultaneously. Ionization stratification could be caused by a clumpy flow, in which the ionization state changes due to small scale density fluctuations, or a stratification in density and ionizing radiation field over larger scales. Invoking clumpiness in these outflows is not an unreasonable hypothesis. Theories of line-driven winds predict an unstable flow (MacGregor et al. 1979; Owocki & Rybicki 1984, 1985), and simulations of CV disc winds also produce density inhomogeneities (Proga et al. 1998, 2002). Tentative evidence for clumping being directly related to P-Cygni optical lines comes from the fact that Prinja et al. (2000) found the dwarf nova BZ Cam’s outflow to be unsteady and highly mass-loaded in outburst, based on observations of the UV resonance lines. This system has also exhibited P-Cygni profiles in He I $\lambda 5876$ and H α when in a high-state (Patterson et al. 1996; Ringwald & Naylor 1998). The degree of ionization and density variation and subsequent line opacities may be affected by our model parameters and the specific parameterisation adopted.

In the UV, the model still produces all the observed lines, and deep P-Cygni profiles are produced in the normal resonance lines, as discussed in section 4.2. However, the UV spectra also display what is perhaps the biggest problem with this revised model, namely the strength of resonance line emission at low and intermediate inclinations. In order to generate strong optical wind signatures, we have adopted wind parameters that lead to very high densities at the base of the wind ($n_e \sim 10^{13} - 10^{14} \text{ cm}^{-3}$). This produces the desired optical recombination emission, but also increases the role of collisional excitation in the formation of the UV resonance lines. This explains the pronounced increase in the emission component of the CIV $\lambda 1550$ resonance line, for example, relative to what

was seen in the benchmark model (compare Figures 1.4 and 1.7). The strength of this component in the revised model is probably somewhat too high to be consistent with UV observations of high-state CVs (see e.g. Long et al. 1991, 1994; Noebauer et al. 2010).

1.3.2 Continuum Shape and the Balmer Jump

The wind now also has a clear effect on the continuum shape, as shown by Fig. 1.9. In fact, the majority of the escaping spectrum has been reprocessed in some way by the wind, either by electron scattering (the wind is now moderately Thomson-thick), or by bound-free processes. This is demonstrated by the flatter spectral shape and the slight He photoabsorption edge present in the optical spectrum (marked in Fig. 1.8). This reprocessing is also responsible for the change in continuum level between models A and B. In addition, Figures 1.7, 1.8 and 1.9 clearly demonstrate that the wind produces a recombination continuum sufficient to completely fill in the Balmer jump at high inclinations.² This might suggest that Balmer continuum emission from a wind can be important in shaping the Balmer jump region, as originally suggested by Knigge et al. (1998b; see also Hassall et al. 1985).

It should be acknowledged, however, that the Balmer jump in high-state CVs would naturally weaken at high inclinations due to limb darkening effects (La Dous 1989b,a). Although simple limb darkening law which affects the emergent flux at each inclination is included, it is not a *frequency dependent* opacity in our model. As a result, the efficiency of filling in the Balmer jump should really be judged at low and medium inclinations, where, although prominent, the recombination continuum does not overcome the disc atmosphere absorption. In addition, this effect could mean that any model which successfully fills in the jump at low inclinations could lead to a Balmer jump in emission at high inclinations. In any case, to properly understand this phenomenon, a fully self-consistent radiative transfer calculation of both the disc atmosphere and connected wind is required.

²Note that the apparent absorption feature just redward of the Balmer jump in these models is artificial. It is caused by residual line blanketing in the stellar atmospheres, which our models cannot fill in since they employ a 20-level H atom.

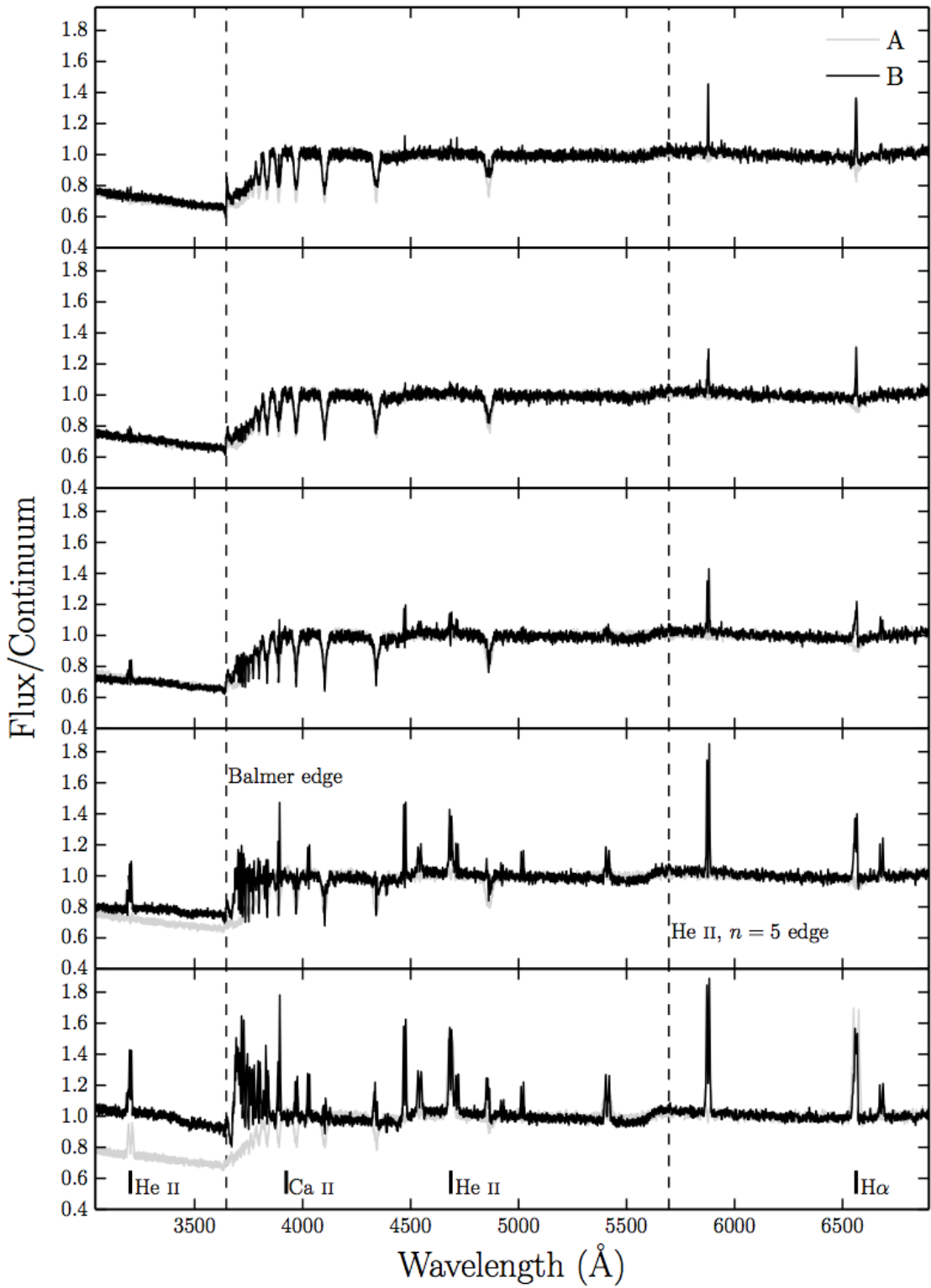


FIGURE 1.8: Synthetic optical spectra from model B computed for sightlines of 10, 27.5, 45, 62.5 and 80 degrees. Model A is shown in grey for comparison. In these plots the flux is divided by a polynomial fit to the underlying continuum redward of the Balmer edge, so that line-to-continuum ratios and the true depth of the Balmer jump can be shown.

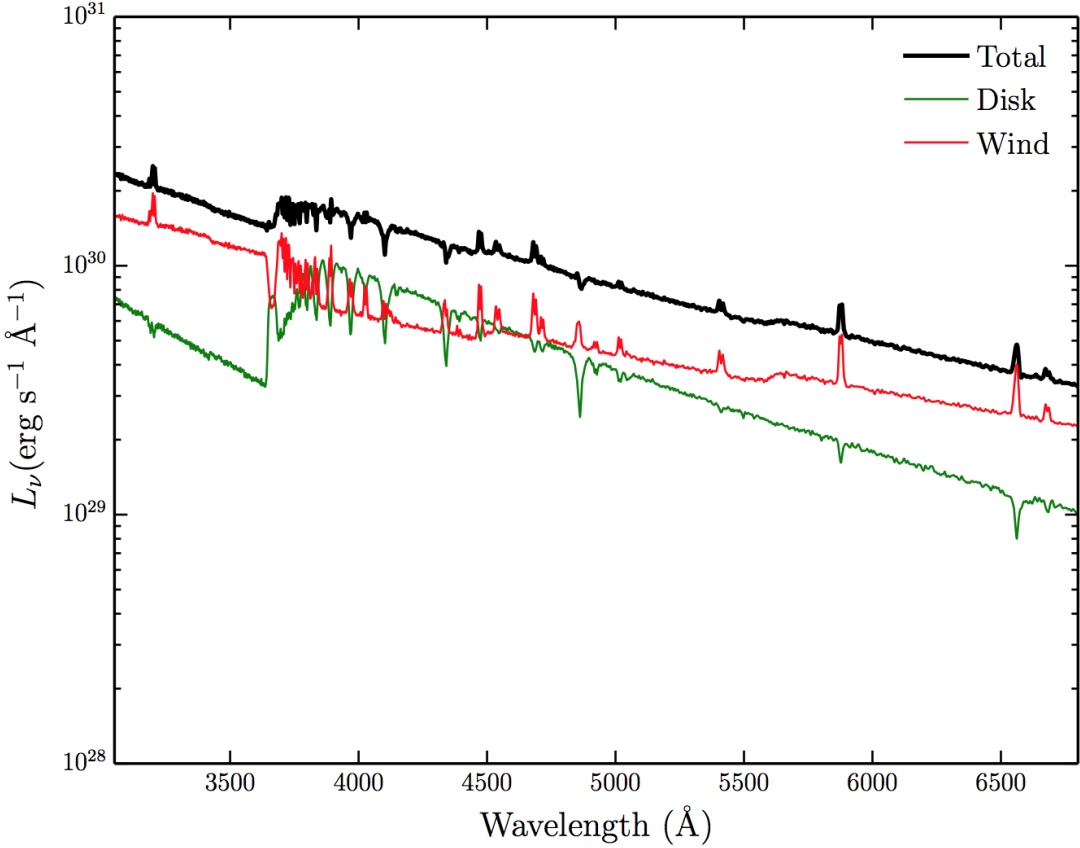


FIGURE 1.9: Total packet-binned spectra across all viewing angles, in units of monochromatic luminosity. The thick black line shows the total integrated escaping spectrum, while the green line shows disc photons which escape without being reprocessed by the wind. The red line show the contributions from reprocessed photons. In this denser model the reprocessed contribution is significant compared to the escaping disc spectrum. The Balmer continuum emission is prominent, and the wind has a clear effect on the overall spectral shape.

1.3.3 Line Profile Shapes: Producing Single-Peaked Emission

Fig. 1.10 shows how the H α profile changes with the kinematics of the wind for an inclination of 80°. The main prediction is that dense, slowly accelerating wind models produce narrower emission lines. This is *not* due to radial velocity shear. As stated by MC96, that mechanism can only work if poloidal and rotational velocity gradients satisfy $(dv_l/dr)/(dv_\phi/dr) \gtrsim 1$; in our models, this ratio is always $\lesssim 0.1$. Instead, the narrow lines predicted by our denser wind models can be traced to the base of the outflow becoming optically thick in the continuum, such that the line emission from the base of the wind cannot escape to the observer. In such models, the ‘line photosphere’ (the $\tau \simeq 1$ surface of the line-forming region) moves outwards, towards larger vertical and

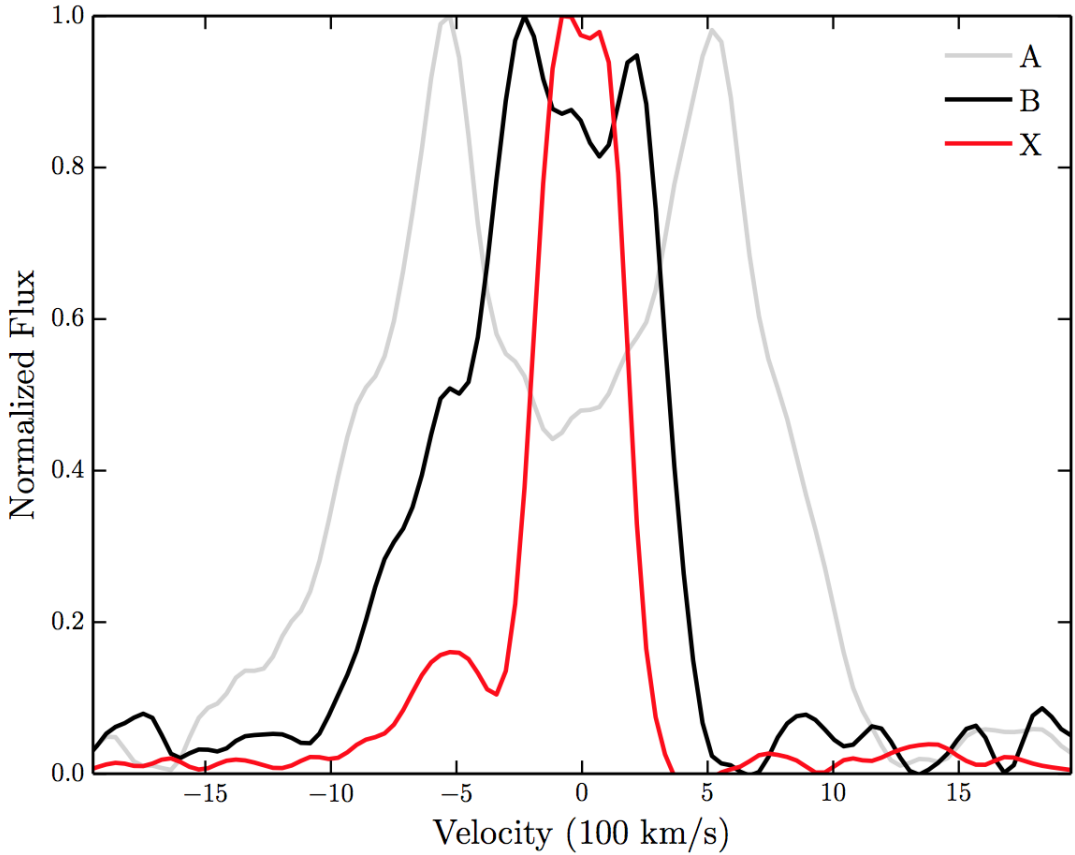


FIGURE 1.10: H α line profiles, normalized to 1, plotted in velocity space for three models with varying kinematic properties, computed at an inclination of 80°. The benchmark model and the improved optical model described in section 6 are labeled as A and B respectively, and a third model (X) which has an increased acceleration length of $R_v = 283.8 R_{WD}$, and $\alpha = 4$ is also shown. The x -axis limits correspond to the Keplerian velocity at $4R_{WD}$, the inner edge of the wind. We observe a narrowing of the lines, and a single-peaked line in model X. This is not due to radial velocity shear (see section 5.3).

cylindrical distances. This reduces the predicted line widths, since the rotational velocities – which normally provide the main line broadening mechanism at high inclination – drop off as $1/r$. This is not to say that the MC96 mechanism could not be at work in CV winds. For example, it would be worth investigating alternative prescriptions for the wind velocity field, as well as the possibility that the outflows may be clumped. An inhomogeneous flow (which has been predicted in CVs; see section 5.2) might allow large radial velocity shears to exist while still maintaining the high densities needed to produce the required level of emission. However, such an investigation is beyond the scope of the present paper.

In our models, single-peaked line profiles are produced once the line forming region has been pushed up to $\sim 10^{11}$ cm ($\sim 150 R_{WD}$) above the disc plane. This number may

seem unrealistically large, but the vertical extent of the emission region is actually not well constrained observationally. In fact, multiple observations of eclipsing NLs show that the H α line is only moderately eclipsed compared to the continuum (e.g. Baptista et al. 2000; Groot et al. 2004; see also section 5.4), implying a significant vertical extent for the line-forming region. This type of model should therefore not be ruled out *a priori*, but this specific model was not adopted as our optically optimized model due to its unrealistically high continuum level in eclipse.

1.3.4 Sensitivity to Model Parameters

This revised model demonstrates that one can achieve a more realistic optical spectrum by altering just two kinematic parameters. However, it may also be possible to achieve this by modifying other free parameters such as \dot{M}_{wind} , the opening angles of the wind and the inner and outer launch radii. For example, increasing the mass-loss rate of the wind increases the amount of recombination emission (which scales as ρ^2), as well as lowering the ionization parameter and increasing the optical depth through the wind. Larger launching regions and covering factors tend to lead to a larger emitting volume, but this is moderated by a decrease in density for a fixed mass-loss rate. We also note that the inner radius of $4 R_{WD}$ adopted by SV93 affects the emergent UV spectrum seen at inclinations $< \theta_{min}$ as the inner disc is uncovered. This causes less absorption in the UV resonance lines, but the effect on the optical spectrum is negligible. We have verified this general behaviour, but we suggest that future work should investigate the effect of these parameters in more detail, as well as incorporating a treatment of clumping. If a wind really does produce the line and continuum emission seen in optical spectra of high-state CVs, then understanding the true mass-loss rate and geometry of the outflow is clearly important.

1.3.5 Comparison to RW Tri

Fig. 1.11 shows a comparison of the predicted out-of-eclipse and mid-eclipse spectra against observations of the high-inclination nova-like RW Tri. The inclination of RW Tri is somewhat uncertain, with estimates including 70.5° (Smak 1995), 75° (Groot et al. 2004), 80° (Longmore et al. 1981) and 82° (Frank & King 1981). Here, we adopt $i = 80^\circ$, but our qualitative conclusions are not particularly sensitive to this choice. We

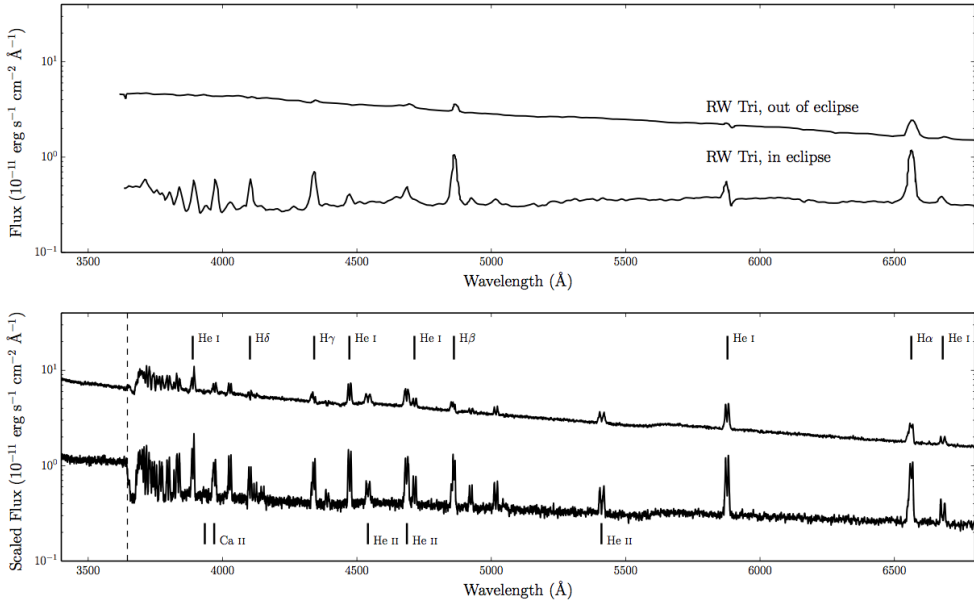


FIGURE 1.11: *Top Panel:* In and out of eclipse spectra of the high inclination NL RW Tri. *Bottom Panel:* In and out of eclipse synthetic spectra from model B. The artificial ‘absorption’ feature just redward of the Balmer jump is caused for the reasons described in section 5.2.

follow LK02 is setting the value of r_{disc} (the maximum radius of the accretion disc) to $34.3 R_{WD}$. When compared to the semi-major axis of RW Tri, this value is perhaps lower than one might typically expect for NLs ([Harrop-Allin & Warner 1996](#)). However, it is consistent with values inferred by [Rutten et al. \(1992\)](#). We emphasize that this model is in no sense a fit to this – or any other – data set.

The similarity between the synthetic and observed spectra is striking. In particular, the revised model produces strong emission in all the Balmer lines, with line-to-continuum ratios comparable to those seen in RW Tri. Moreover, the line-to-continuum contrast increases during eclipse, as expected for emission produced in a disc wind. This trend is in line with the observations of RW Tri, and it has also been seen in other NLs, including members of the SW Sex class ([Neustroev et al. 2011](#)). As noted in section 5.2, the majority of the escaping radiation has been reprocessed by the wind in some way (particularly the eclipsed light).

However, there are also interesting differences between the revised model and the RW Tri data set. For example, the model exhibits considerably stronger He II features than the observations, which suggests that the overall ionization state of the model is

somewhat too high. As discussed in section 5.3, the optical lines are narrow, but double-peaked. This is in contrast to what is generally seen in observations of NLs, although the relatively low resolution of the RW Tri spectrum makes a specific comparison difficult. In order to demonstrate the double-peaked nature of the narrower lines, we do not smooth the synthesized data to the resolution of the RW Tri dataset. If the data was smoothed, the H α line would appear single-peaked.

1.4 Discussion: Collision Strengths and Boundary Layers

The van Regemorter approximation uses an effective gaunt factor, of order unity. To conduct these simulations a value of $\bar{g} = 1$ was adopted. There are two main concerns when using this approach. The first is related to accuracy, as poorly estimating collision strengths could lead to incorrect heating and cooling balance in the flow, with knock-on effects on the emergent spectrum. The second is that collisions between radiatively forbidden transitions are not taken into account when one splits levels into l - and s -subshells, as well as principal quantum number, n (as we have done with He I; see section ??). Although this approximation is, in general, a poor one, the effect is quantified in section 1.4.1.1.

1.4.1 Model Sensitivity to Collision Strengths

1.4.1.1 Collisions Between Radiatively Forbidden Transitions

1.4.1.2 Line Heating and Cooling

Fig. ?? shows four important heating and cooling mechanisms in the wind for model B. Line heating and cooling

1.4.2 Improving Collision Strengths

1.4.3 Introducing a Boundary Layer

1.5 Conclusions

We have investigated whether a disc wind model designed to reproduce the UV spectra of high-state CVs would also have a significant effect on the optical spectra of these systems. We find that this is indeed the case. In particular, the model wind produces H and He recombination lines, as well as a recombination continuum blueward of the Balmer edge. We do not produce P-Cygni profiles in the optical H and He lines, which are seen in a small fraction of CV optical spectra. Possible reasons for this are briefly discussed in section 5.2.

We have also constructed a revised benchmark model which is designed to more closely match the optical spectra of high-state CVs. This optically optimized model produces all the prominent optical lines in and out of eclipse, and achieves reasonable verisimilitude with the observed optical spectra of RW Tri. However, this model also has significant shortcomings. In particular, it predicts stronger-than-observed He II lines in the optical region and too much of a collisionally excited contribution to the UV resonance lines. Incorporating more accurate collisional data into PYTHON will help assess this discrepancy in more detail.

Based on our results, we argue that recombination emission from outflows with sufficiently high densities and/or optical depths might produce the optical lines observed in CVs, and may also fill in the Balmer absorption edge in the spectrum of the accretion disc, thus accounting for the absence of a strong edge in observed CV spectra. In section 5.3, we demonstrated that although the double peaked lines narrow and single-peaked emission can be formed in our densest models, this is not due to the radial velocity shear mechanism proposed by MC96. We suggest that ‘clumpy’ line-driven winds or a different wind parameterization may nevertheless allow this mechanism to work. We also note the possibility that, as in our denser models, the single-peaked lines are formed well above the disc, where rotational velocities are lower.

It is not yet clear whether a wind model such as this can explain all of the observed optical features of high-state CVs – further effort is required on both the observational and modelling fronts. However, our work demonstrates that disc winds may not just be responsible for creating the blue-shifted absorption and P-Cygni profiles seen in the UV resonance lines of high-state CVs, but can also have a strong effect on the optical appearance of these systems. In fact, most of the optical features characteristic of CVs are likely to be affected – and possibly even dominated – by their disc winds. Given that optical spectroscopy plays the central role in observational studies of CVs, it is critical to know where and how these spectra are actually formed. We believe it is high time for a renewed effort to understand the formation of spectra in accretion discs and associated outflows.

Chapter 2

Testing Quasar Unification: Radiative Transfer In Clumpy Winds

This chapter is based on the publication:

Matthews J. H., Knigge C., Long K. S., Sim S. A., Higginbottom N., Mangham S. W., ‘Testing quasar unification: radiative transfer in clumpy winds’, 2016, MNRAS, 458, 293.

2.1 Introduction

In the earlier chapters I presented the evidence for accretion disc winds in quasars and luminous AGN, and showed how they may be responsible for more than just the broad absorption lines and P-Cygni profiles seen in quasar spectra. In particular, they offer a natural way to *unify* much of the complex phenomenology into one simple picture.

Here, I aim to test that picture using PYTHON, with the specific aim of determining whether it is possible to simulate the properties of the spectra of AGN, including BALQSOs, using simple kinematic prescriptions for biconical disc winds. Past results have been encouraging; H13 produced simulated spectra that resembled that of BALQSOs, as long as the luminosity of the X-ray source was relatively low, of order 10^{43} erg s⁻¹ and the

mass loss rate was relatively high, of order the mass accretion rate. However, at higher X-ray luminosities, the wind was so ionized that UV absorption lines were not produced. In addition, and in part due to limitations inherent in the radiative transfer methods, the model failed to produce spectra with strong emission lines at any inclination angle.

Here I attempt to address both of these issues, by introducing clumping into PYTHON and a more complete treatment of H and He into the radiative transfer calculations. Thus, the simulations presented in this chapter treat H & He as full macro-atoms, and model metals as simple-atoms as described extensively in chapter 3. In order to correctly model the ionizing spectrum for simple-atoms I dispense with the ML93 modified Saha approach and fully solve the ionization balance using the spectral modelling approach described in section ???. Macro-atoms still have their ionization and excitation states calculated from MC estimators.

The kinematic model used once again follows the SV93 prescription, and is described, together with the clumping implementation, in section 2.2. Section 2.3 contains the results from a clumped model, with comparisons to observational data, as well as some discussion. Further discussion and examination of sensitivity to model parameters and viewing angle can be found in section 2.4, which expands somewhat on the work presented in (Matthews et al. 2016). Finally, I summarise the findings in section 2.5.

2.2 A Clumpy Biconical Disk Wind Model for Quasars

Here, I once again adopt the SV93 kinematic prescription for a biconical disc wind model described in section ?? LK02, H13 and M15. A schematic is shown in Fig. 3.6, with key aspects marked. The general biconical geometry is similar to that invoked by Murray et al. (1995) and Elvis (2000) to explain the phenomenology of quasars and BALQSOs.

2.2.1 Photon Sources

Two sources of r-packets are included in the model: An accretion disc and a central X-ray source. The accretion disc is assumed to be geometrically thin, but optically thick. Accordingly, the disc is modelled as an ensemble of blackbodies with a Shakura &

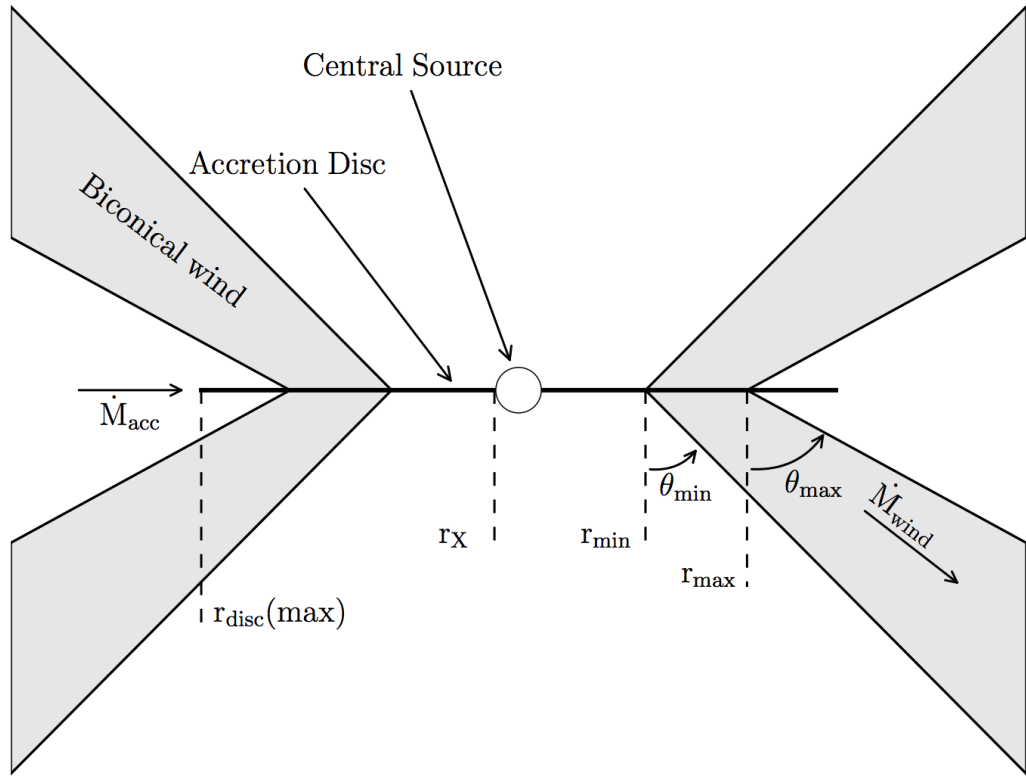


FIGURE 2.1: A cartoon showing the geometry and some key parameters of the biconical quasar wind model.

[Sunyaev \(1973\)](#) effective temperature profile. The emergent SED is then determined by the specified accretion rate (\dot{m}) and central BH mass (M_{BH}). All photon sources in the model are opaque, meaning that r -packets that strike them are destroyed. The inner radius of the disc extends to the innermost stable circular orbit (ISCO) of the BH. I assume a Schwarzschild BH with an ISCO at $6 r_G$, where $r_G = GM_{BH}/c^2$ is the gravitational radius. For a $10^9 M_\odot$ BH, this is equal to 8.85×10^{14} cm or $\sim 10^{-4}$ pc.

The X-ray source is treated as an isotropic sphere at the ISCO, which emits r -packets according to a power law in flux with index α_X , of the form

$$F_X(\nu) = K_X \nu^{\alpha_X}. \quad (2.1)$$

The normalisation, K_X of this power law is such that it produces the specified 2-10 keV luminosity, L_X . The input spectrum for the simulations is therefore a simple combination of a power law X-ray component and accretion disc spectrum; an example input spectrum is shown in Fig. 2.2. In actual fact, this spectrum will be angle dependent due to the

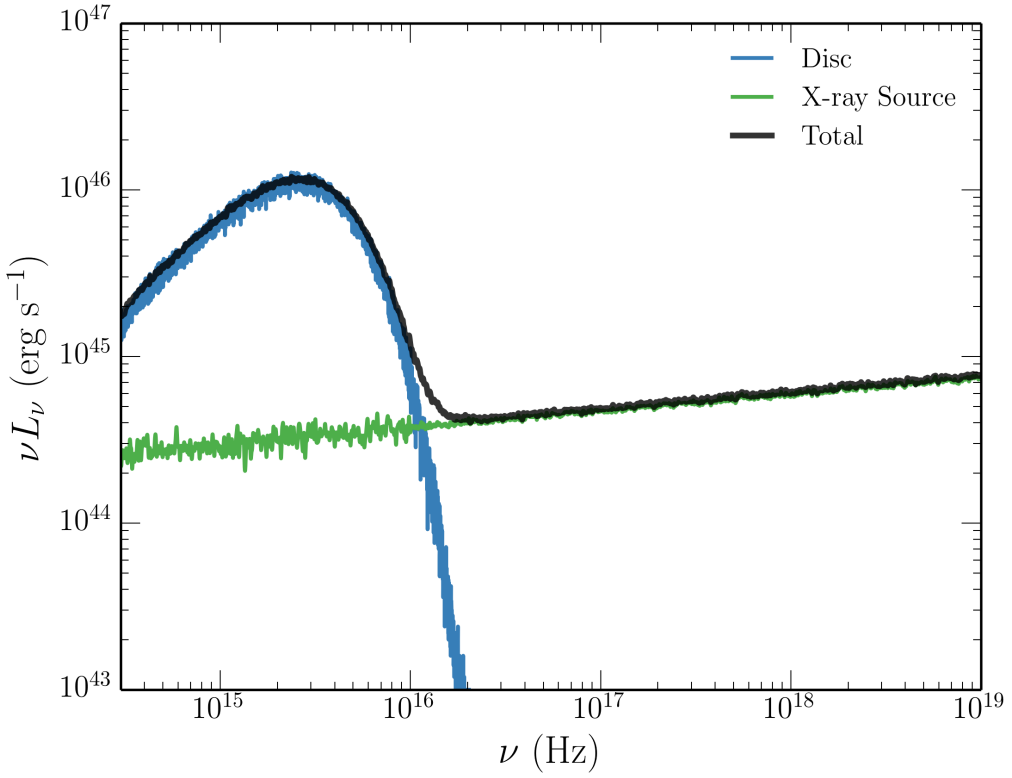


FIGURE 2.2: The input spectrum used for the quasar modelling.

geometry of the system and the angular emissivity profile of the accretion disc (see sections 2.3.3 and 2.4.2. Photons, or r -packets, produced by the accretion disc and central X-ray source are reprocessed by the wind. This reprocessing is dealt with by enforcing strict radiative equilibrium (*modulo* adiabatic cooling; see section 2.3) via an indivisible energy packet constraint (see Lucy 2002, M15).

2.2.2 A Simple Approximation for Clumping

In previous modelling efforts with PYTHON, a smooth outflow was assumed, such that the density at a given point was determined only by the kinematic parameters and mass loss rate. However, as already discussed, AGN winds exhibit significant substructure – the outflow is expected to be *clumpy*, rather than smooth, and probably on a variety of scales. A clumpy outflow offers a possible solution to the so-called ‘over-ionization problem’ in quasar and AGN outflows (e.g. ??Hamann et al. 2013). This is the main motivation for incorporating clumping into the model.

Deciding on how to implement clumping into the existing wind models was not straightforward. First, and most importantly, the physical scale lengths and density contrasts in AGN outflows are not well-constrained from observations or theory. As a result, while one could envision in principle, clouds with a variety of sizes and density contrasts varying perhaps as function of radius, there would have been very little guidance on how to set nominal values of the various parameters of such a model. Second, there are significant computational difficulties associated with adequately resolving and realistically modelling a series of small scale, high density regions with a MCRT – or for that matter, a hydrodynamical – code. Given the lack of knowledge about the actual type of clumping, I have implemented a simple approximation used successfully in stellar wind modelling, known as *microclumping* (e.g. [Hamann & Koesterke 1998](#); [Hillier & Miller 1999](#); [Hamann et al. 2008](#)).

The underlying assumption of microclumping is that clump sizes are much smaller than the typical photon mean free path, and thus the clumps are both geometrically and optically thin. This approach allows one to treat clumps only in terms of their volume filling factor, f_V , instead of having to specify separately their size and density distributions. In this model, f_V is independent of position (see section 4.4). The inter-clump medium is modeled as a vacuum, although the outflow is still non-porous and axisymmetric. This approach therefore assumes that the inter-clump medium is unimportant in determining the output spectrum, which is expected to be true only when density constraints are large and the inter-clump medium is both very ionized and of low emissivity and opacity. The density of the clumps is multiplied by the “density enhancement” $D = 1/f_V$. Opacities, κ , and emissivities, ϵ , can then be expressed as

$$\kappa = f_V \kappa_C(D); \quad \epsilon = f_V \epsilon_C(D). \quad (2.2)$$

Here the subscript C denotes that the quantity is calculated using the enhanced density in the clump. The resultant effect is that, *for fixed temperature*, processes that are linear in density, such as electron scattering, are unchanged, as f_V and D will cancel out. However, any quantity that scales with the square of density, such as collisional excitation or recombination, will increase by a factor of D . In PYTHON, the temperature is not fixed, and is instead set by balancing heating and cooling in a given cell. In the presence of an X-ray source, this thermal balance is generally dominated by bound-free heating and line cooling. The main effect of including clumping in this modelling is that

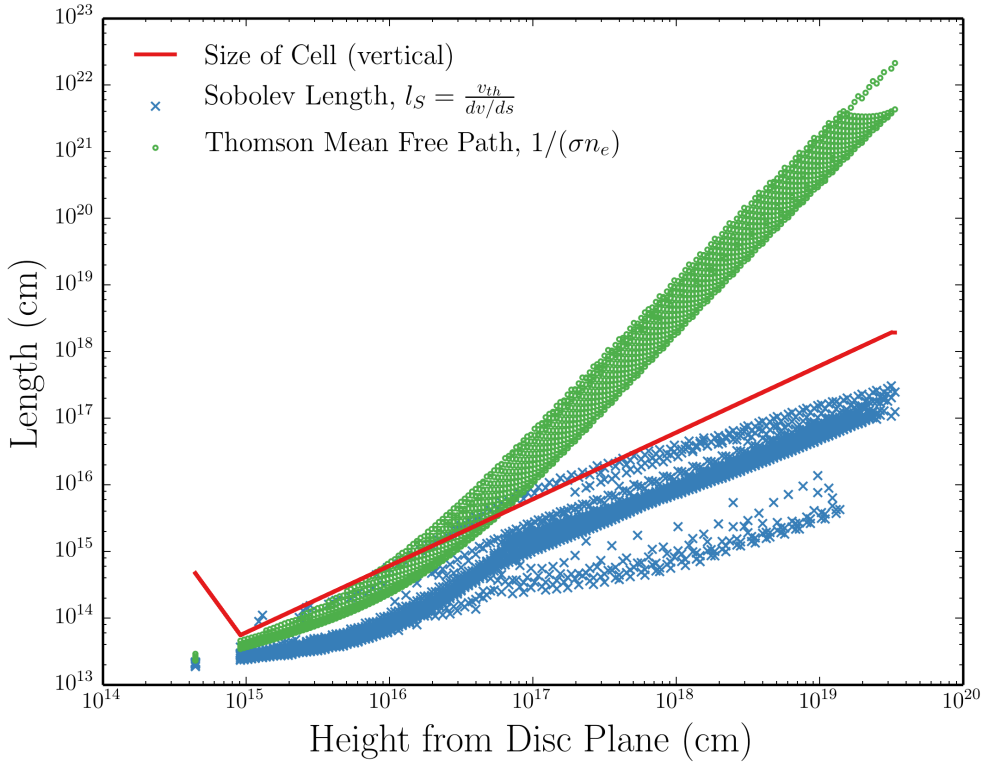


FIGURE 2.3: Some typical length scales for the fiducial model. This places a formal limit of $\sim 10^{12}$ cm on clump sizes in the microclumping framework, and confirms that the cells are sufficiently larger than the Sobolev length in almost all cases.

it moderates the ionization state due to the increased density. This allows an increase in the ionizing luminosity, amplifying the amount of bound-free heating and also increasing the competing line cooling term (thermal line emission).

The shortest length scale in a Sobolev MCRT treatment such as ours is normally the Sobolev length, given by

$$l_S = \frac{v_{th}}{|dv/ds|} \quad (2.3)$$

This is typically $\sim 10^{13}$ cm near the disc plane, increasing outwards. The Sobolev length is shown, together with the size of the cell and Thomson mean free path, in Fig. 2.3. The mean density is used to calculate the Sobolev optical depth, which assumes that l_S is greater than the typical clump size. Thus for the microclumping assumption to be formally correct, clumps should be no larger than $\sim 10^{12}$ cm. This size scale is not unreasonable for quasar outflows, as [de Kool & Begelman \(1995\)](#) suggest that BAL flows may have low filling factors with clump sizes of $\sim 10^{11}$ cm.

Our clumping treatment is necessarily simple; it does not adequately represent the complex substructures and stratifications in ionization state expected in AGN outflows. Nevertheless, this parameterization allows simple estimates of the effect clumping has on the ionization state and emergent line emission.

2.2.3 The Simulation Grid

Using this prescription, I conducted a limited parameter search over a 5-dimensional parameter space involving the variables r_{min} , θ_{min} , f_V , α and R_v . The grid points are shown in Table 1. The aim here was to first fix M_{BH} and \dot{m} to their H13 values, and increase L_X to 10^{45} erg s $^{-1}$ (a more realistic value for a quasar of $10^9 M_\odot$ and an Eddington fraction of 0.2; see section 2.3.3).

These models were then evaluated based on how closely their synthetic spectra reproduced the following properties of quasars and BALQSOs:

- UV absorption lines with $BI > 0$ at $\sim 20\%$ of viewing angles (e.g. Knigge et al. 2010);
- Line emission emerging at low inclinations, with $EW \sim 40\text{\AA}$ in C IV 1550\AA (e.g. Shen et al. 2011);
- H recombination lines with $EW \sim 50\text{\AA}$ in Ly α (e.g. Shen et al. 2011);
- Mg II and Al III (LoBAL) absorption features with $BI > 0$ at a subset of BAL viewing angles;
- Verisimilitude with quasar composite spectra.

Here BI is the ‘Balnicity Index’ (Weymann et al. 1991), given by

$$BI = \int_{3000 \text{ km s}^{-1}}^{25000 \text{ km s}^{-1}} C \left(1 - \frac{f(v)}{0.9} \right) dv. \quad (2.4)$$

The constant $C = 0$ everywhere, unless the normalized flux has satisfied $f(v) < 0.9$ continuously for at least 2000 km s 1 , whereby C is set to 1.

In the next section, I present one of the most promising models, which I refer to as the fiducial model, and discuss the various successes and failures with respect to the

Parameter	Grid Point Values		
r_{min}	$60r_g$	$180r_g$	$300r_g$
θ_{min}	55°	70°	
R_v	10^{18}cm	10^{19}cm	
α	0.5	0.6	0.75
f_V	0.01	0.1	1.5

TABLE 2.1: The grid points used in the parameter search. The sensitivity to some of these parameters is discussed further in section 2.4.1

above criteria. This allows us to gain insight into fundamental geometrical and physical constraints and assess the potential for unification. I then discuss the sensitivity to key parameters in section 2.4.1. The full grid, including output synthetic spectra and plots can be found at jhmatthews.github.io/quasar-wind-grid/.

2.3 Results and Analysis From A Fiducial Model

Here I describe the results from a fiducial model, and discuss these results in the context of the criteria presented in section 3.4. The parameters of this model are shown in Table 2. Parameters differing from the benchmark model of H13 are highlighted with an asterisk. In this section, I examine the physical conditions of the flow, and present the synthetic spectra, before comparing the X-ray properties of this particular model to samples of quasars and luminous AGN.

2.3.1 Physical Conditions and Ionization State

Fig. 2.4 shows the physical properties of the wind. The wind rises slowly from the disc at first, with densities within clumps of $n_H \sim 10^{11} \text{ cm}^{-3}$ close to the disc plane, where n_H is the local number density of H. To illustrate the degree of scale and density ranges in the model I also show n_e in the wind on a linear scale in Fig. 2.5. The flow then accelerates over a scale length of $R_V = 10^{19} \text{ cm}$ up to a terminal velocity equal to the escape velocity at the streamline base ($\sim 10,000 \text{ km s}^{-1}$). This gradual acceleration results in a wind that exhibits a stratified ionization structure, with low ionization material in the base of the wind giving way to highly ionized plasma further out. This is illustrated in Fig. 2.4 by the panels showing the ion fraction $F = n_j/n_{tot}$ of some important ions. The clumped wind produces the range of ionization states observed

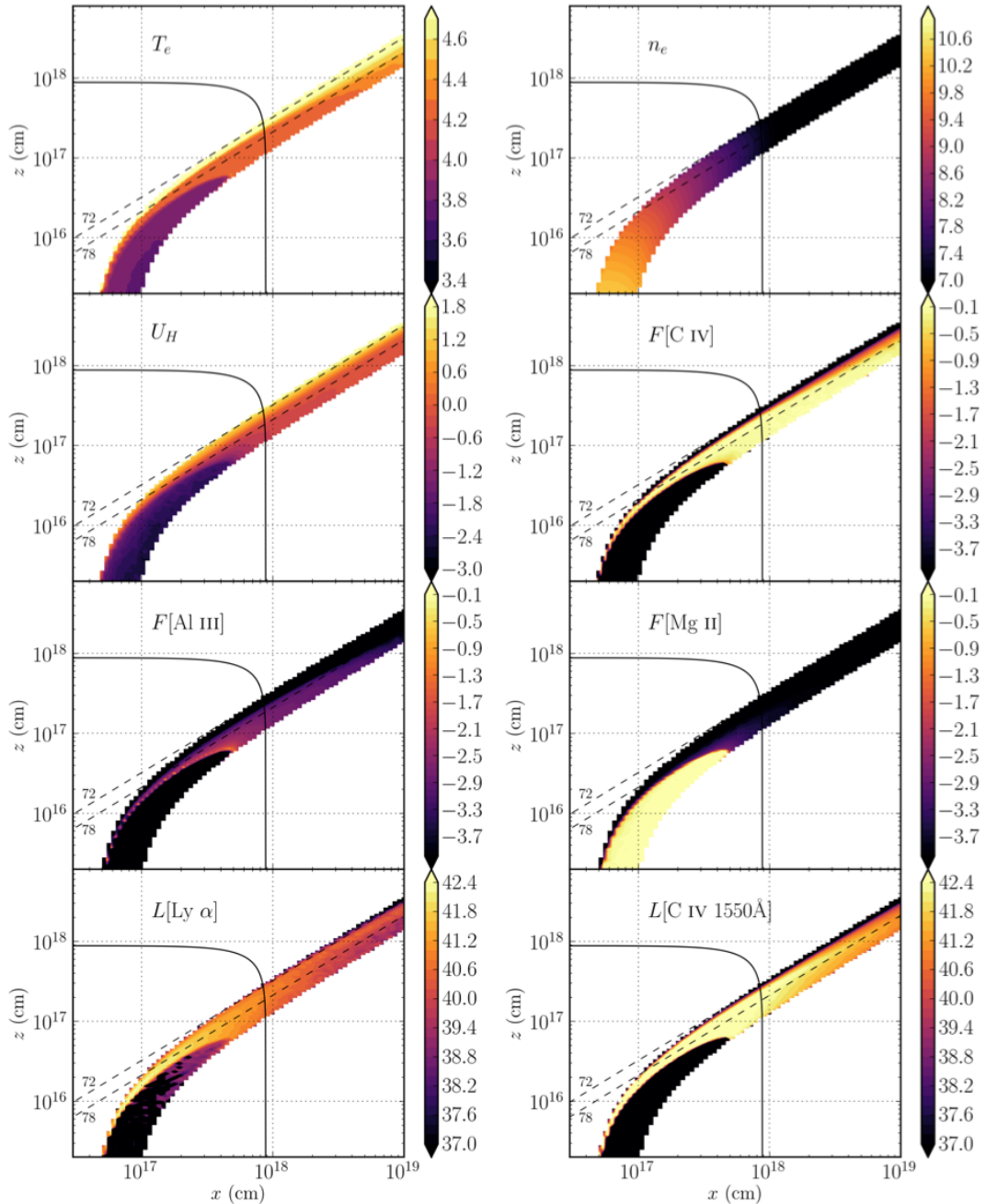


FIGURE 2.4: Contour plots showing the logarithm of some important physical properties of the outflow. The spatial scales are logarithmic and the x and z scales are not the same. Symbols are defined in the text. The solid black line marks a sphere at $1000 r_G$. The dotted lines show the 72° and 78° sightlines to the centre of the system, and illustrate that different sightlines intersect material of different ionization states. The line luminosities, L , represent the luminosity of photons escaping the Sobolev region for each line. These photons do not necessarily escape to infinity.

Fiducial Parameters	Model	Value
M_{BH}		$1 \times 10^9 M_\odot$
\dot{m}_{acc}		$5 M_\odot yr^{-1} \simeq 0.2 \dot{M}_{Edd}$
α_X		-0.9
L_X		$10^{45} \text{ erg s}^{-1}$
$r_{disc}(\min) = r_X$		$6r_g = 8.8 \times 10^{14} \text{ cm}$
$r_{disc}(\max)$		$3400r_g = 5 \times 10^{17} \text{ cm}$
\dot{m}_{wind}		$5 M_\odot yr^{-1}$
r_{min}		$300r_g = 4.4 \times 10^{16} \text{ cm}$
r_{max}		$600r_g = 8.8 \times 10^{16} \text{ cm}$
θ_{min}		70.0°
θ_{max}		82.0°
$v_\infty(r_0)$		$v_{esc}(r_0)$
R_v		10^{19} cm^*
α		0.5*
f_V		0.01*
n_x		100
n_z		200

TABLE 2.2: Wind geometry parameters used in the fiducial model, as defined in the text and figure 1. Parameters differing from the benchmark model of H13 are highlighted with an asterisk.

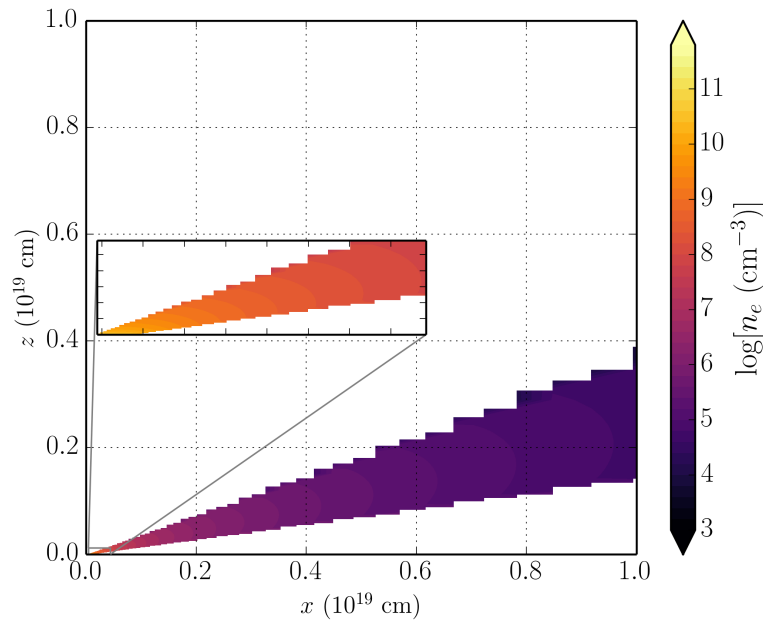


FIGURE 2.5: The electron density in the model, this time on linear axes in order to illustrate the density contrasts and scale of the system. The plot is on the scale of the acceleration length, whereas the inset is a box of $2700 \times 800r_G$, where the bottom left corner corresponds to the base of the innermost streamline.

in quasars and BALQSOs, while adopting a realistic $2 - 10$ keV X-ray luminosity of $L_X = 10^{45}$ erg s $^{-1}$. Without clumping, this wind would be over-ionized to the extent that opacities in e.g., C IV would be entirely negligible (see H13).

One common way to quantify the ionization state of a plasma is through the ionization parameter, U_H , given by equation ???. Shown in Fig. 2.4, the ionization parameter is a useful measure of the global ionization state, as it represents the ratio of the number density of H ionizing photons to the local H density. It is, however, a poor representation of the ionization state of species such as C IV as it encodes no information about the shape of the SED. In this case, the X-ray photons are dominant in the photoionization of the UV resonance line ions. This explains why a factor of 100 increase in X-ray luminosity requires a clumping factor of 0.01, even though the value of U_H decreases by only a factor of ~ 10 compared to H13.

The total line luminosity also increases dramatically compared to the unclumped model described by H13. This is because the denser outflow can absorb the increased X-ray luminosity without becoming over-ionized, leading to a hot plasma which produces strong collisionally excited line emission. This line emission typically emerges on the edge of the wind nearest the central source. The location of the line emitting regions is dependent on the ionization state, as well as the incident X-rays. The radii of these emitting regions is important, and can be compared to observations. The line luminosities, L , shown in the figure correspond to the luminosity in erg s $^{-1}$ of photons escaping the Sobolev region for each line. As shown in Fig. 2.4, the C IV 1550Å line in the fiducial model is typically formed between $100 - 1000 r_G$ ($\sim 10^{17} - 10^{18}$ cm). This is in rough agreement with the reverberation mapping results of Kaspi et al. (2007) for the $2.6 \times 10^9 M_\odot$ quasar S5 0836+71, and also compares favourably with microlensing measurements of the size of the C IV 1550Å emission line region in the BALQSO H1413+117 (O'Dowd et al. 2015).

2.3.2 Synthetic Spectra: Comparison to Observations

Fig. 2.6 shows the synthetic spectrum in the UV from the fiducial model. To assess the ability of the synthetic spectra to match real quasar spectra, I also show *Sloan Digital Sky Survey* (SDSS) quasar composites from Reichard et al. (2003), normalised to the flux at 2000Å for low inclinations. Unfortunately, the wide variety of line profile shapes and internal trough structure in BALQSOs tends to ‘wash out’ BAL troughs in composite

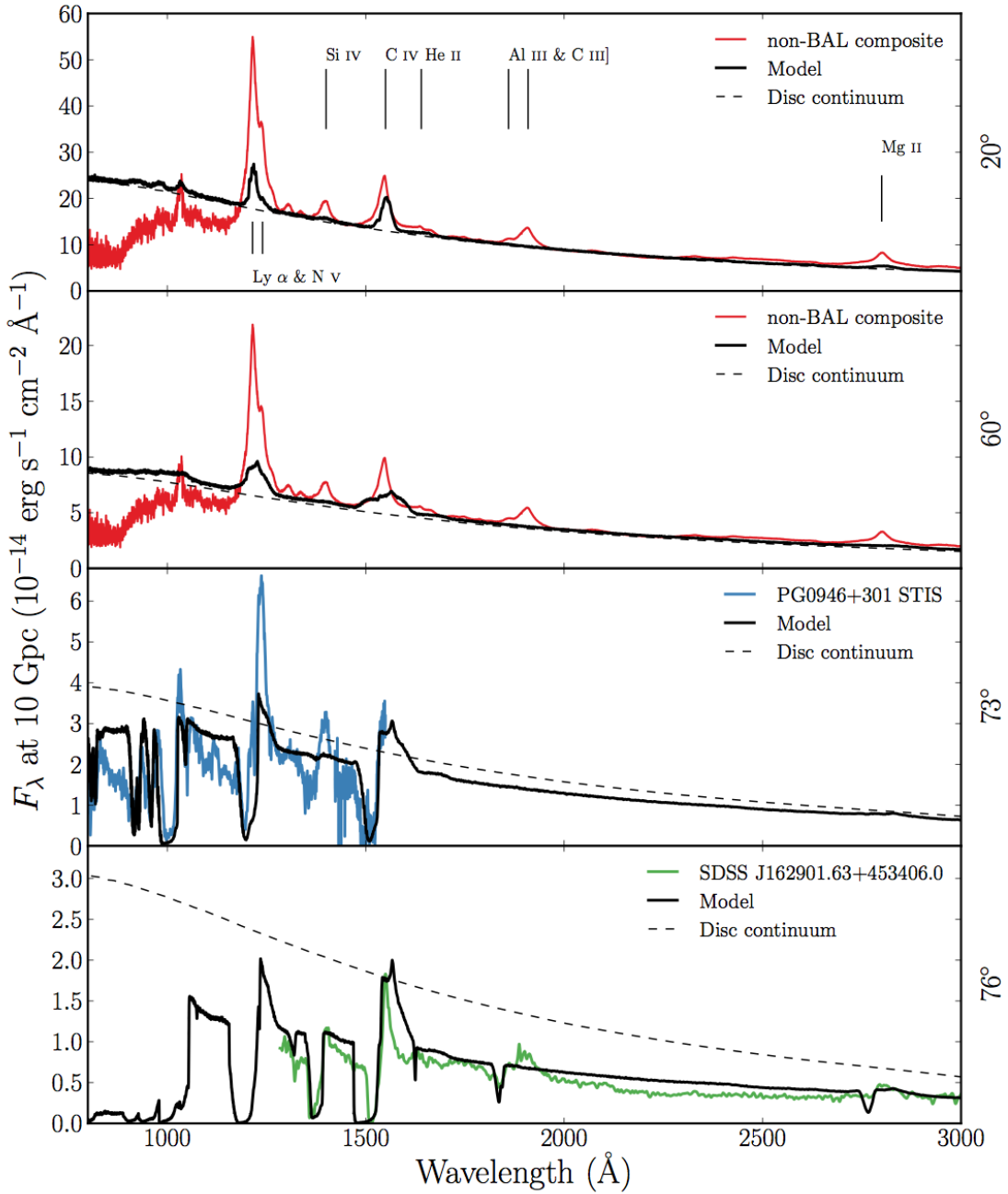


FIGURE 2.6: Synthetic spectra at four viewing angles for the fiducial model. At 20° and 60° I show a comparison to an SDSS quasar composite from Recihard et al. (2003). At 73° and 76° I show a comparison to an *HST* STIS spectrum of the high BALnicity BALQSO PG0946+301 (Arav et al. 2000), and an SDSS spectrum of the LoBAL quasar SDSS J162901.63+453406.0, respectively. The dotted line shows a disc only continuum to show the effect of the outflow on the continuum level. All the spectra are scaled to the model flux at 2000\AA , except for the *HST* STIS spectrum of PG0946+301, which is scaled to 1350\AA due to the incomplete wavelength coverage.

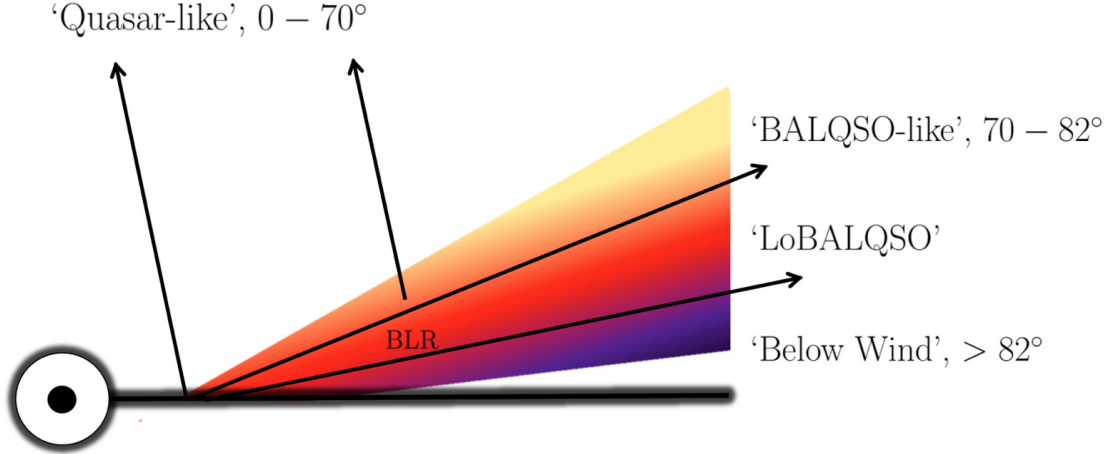


FIGURE 2.7: A cartoon describing the broad classes of sightline in the fiducial model, illustrating how geometric effects lead to the different emergent spectra. The colour gradient is approximate, but indicates the stratified ionization structure, from highly ionized (yellow) to low ionization (purple) material.

spectra to the extent that BALQSO composites do not resemble typical BALQSOs. Because of this, I instead compare to a *Hubble Space Telescope* STIS spectrum of the high BALnicity BALQSO PG0946+301 (Arav et al. 2000), and an SDSS spectrum of the LoBAL quasar SDSS J162901.63+453406.0, for the angles of 73° and 76° , respectively. A cartoon illustrating how geometric effects determine the output spectra is shown in Fig. 2.7.

2.3.2.1 Broad absorption lines ('BALQSO-like' angles)

The UV spectrum is characterised by strong BAL profiles at high inclinations ($> 70^\circ$). This highlights the first success of the model: clumping allows the correct ionization state to be maintained in the presence of strong X-rays, resulting in large resonance line opacities. At the highest inclinations, the cooler, low ionization material at the base of the wind starts to intersect the line of sight. This produces multiple absorption lines in species such as Mg II, Al III and Fe II. The potential links to LoBALQSOs and FeLoBALQSOs are discussed in section 2.4.

The high ionization BAL profiles are often saturated, and the location in velocity space of the strongest absorption in the profile varies with inclination. At the lowest inclination BAL sight lines, the strongest absorption occurs at the red edge, whereas at higher

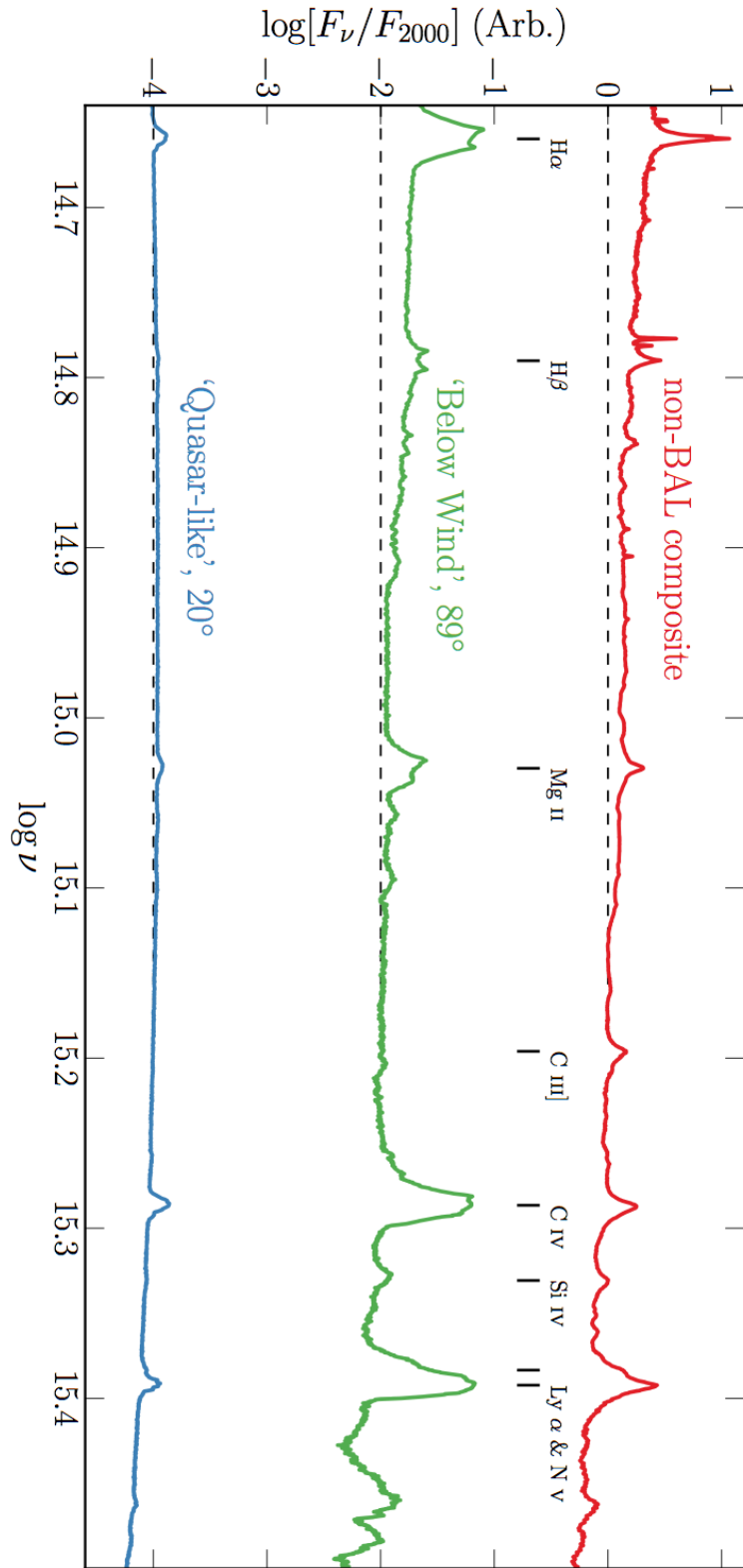


FIGURE 2.8: Synthetic spectra at two viewing angles, this time in frequency space and including the optical band, compared to the non-BAL SDSS quasar composite. The spectra are normalised to the flux at 2000Å, then an offset of 2 is applied per spectrum for clarity – the dotted lines show the zero point of F_ν/F_{2000} in each case.

Property	Synthetic, 20°	Observed (S11)
$\log L[\text{C IV}]$	44.60	44.42 ± 0.32
$\log L[\text{Mg II}]$	43.92	43.54 ± 0.28
$\log(\nu L_\nu)_{1350}$	46.42	46.01 ± 0.30
$\log(\nu L_\nu)_{3000}$	46.18	45.79 ± 0.30

TABLE 2.3: Some derived spectral properties of the fiducial model, at 20°, compared to observations. The observed values are taken from the Shen et al. (2011) SDSS DR7 Quasar catalog, and correspond to mean values with standard deviations in log space from a subsample with $8.5 > \log(M_{BH}) < 9.5$ and $1.5 < \log(L_{bol}/L_{Edd}) < 0$, where the BH mass is a C IV virial estimate. Units are logarithms of values in erg s⁻¹.

inclinations (and for the strongest BALs) the trough has a sharp edge at the terminal velocity. This offers one potential explanation for the wide range of BALQSO absorption line shapes (see e.g. [Trump et al. 2006](#); [Knigge et al. 2008](#); [Filiz Ak et al. 2014](#)).

The absorption profiles seen in BALQSOs are often non-black, but saturated, with flat bases to the absorption troughs ([Arav et al. 1999a,b](#)). This is usually explained either as partial covering of the continuum source or by scattered contributions to the BAL troughs, necessarily from an opacity source not co-spatial with the BAL forming region. The scattered light explanation is supported by spectropolarimetry results ([Lamy & Hutsemékers 2000](#)). Our spectra do not show non-black, saturated profiles. Black, saturated troughs are seen at angles $i > 73^\circ$, and the BALs are non-saturated at lower inclinations. The reasons for this are inherent in the construction of the model. First, the microclumping assumption does not allow for porosity in the wind, meaning that it does not naturally produce a partial covering absorber. To allow this, an alternative approach such as *macroclumping* would be required (e.g. [Hamann et al. 2008](#); [Šurlan et al. 2012](#)). Second, the wind does not have a significant scattering contribution along sightlines which do not pass through the BAL region, meaning that any scattered component to the BAL troughs is absorbed by line opacity. This suggests that either the scattering cross-section of the wind must be increased (with higher mass loss rates or covering factors), or that an additional source of electron opacity is required, potentially in a polar direction above the disc. I note the scattering contribution from plasma in polar regions is significant in some ‘outflow-from-inflow’ simulations ([Kurosawa & Proga 2009](#); [Sim et al. 2012](#)).

2.3.2.2 Broad emission lines ('quasar-like' angles)

Unlike H13, significant collisionally excited line emission now emerges at low inclinations in the synthetic spectra, particular in the C IV and N V lines. Strong Ly α and weak He II 1640Å lines are also observed as a result of the improved treatment of recombination using macro-atoms. In the context of unification, this is a promising result, and shows that a biconical wind can produce significant emission at 'quasar-like' angles. To demonstrate this further, I show line luminosities and monochromatic continuum luminosities from the synthetic spectra in Table 2.3. These are compared to mean values from a subsample of the SDSS DR7 quasar catalog (Shen et al. 2011) with BH mass and Eddington fraction estimates similar to the fiducial model values (see caption). The spectra do not contain the strong C III] 1909Å line seen in the quasar composite spectra, but this is due to a limitation of the current treatment of C; semi-forbidden (intercombination) lines are not included in this modelling.

In Fig. 2.8, I show an F_ν spectrum with broader waveband coverage that includes the optical, showing that the synthetic spectra also exhibit H α and H β emission. In this panel, I include a low inclination and also a very high inclination spectrum, which looks underneath the wind cone. This model shows strong line emission with very similar widths and line ratios to the quasar composites, and the Balmer lines are double peaked, due to velocity projection effects. Such double-peaked lines are seen in so-called 'disc emitter' systems (e.g. Eracleous & Halpern 1994) but not the majority of AGN. The line equivalent widths (EWs) increase at high inclination due to a weakened continuum from wind attenuation, disc foreshortening and limb darkening. This effect also leads to a redder continuum slope, as seen in quasars, which is due to Balmer continuum and Balmer and Fe II line emission. This extreme 89° viewing angle cannot represent a typical quasar within a unified model, but does show that a model such as this can naturally reproduce quasar emission lines if the emissivity of the wind is increased *with respect to the disc continuum*. In addition, it neatly demonstrates how a stratified outflow can naturally reproduce the range of ionization states seen in quasars.

Despite a number of successes, there are some properties of the synthetic spectra that are at odds with the observations. First, the ratios of the EW of the Ly α and Mg II 2800Å lines to the EW of C IV 1550Å are much lower than in the composite spectra. Similar problems have also been seen in simpler photoionization models for

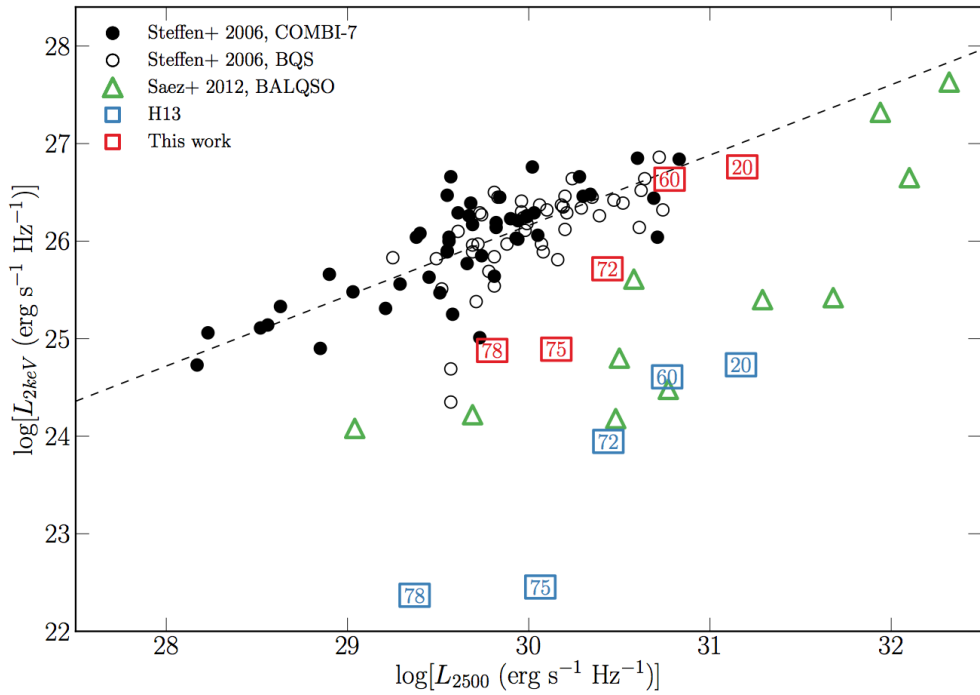


FIGURE 2.9: X-ray (2 keV) luminosity of the clumped model (red squares) and the H13 model (blue squares), plotted against monochromatic luminosity at 2500Å. The points are labeled according to inclination; angles $> 70^\circ$ correspond to BALs in this scheme (see figure 4). Also plotted are measurements from the COMBI-7 AGN and the BQS samples (Steffen et al. 2006) and the Saez et al. (2012) sample of BALQSOs. The dotted line shows the best fit relation for non-BALQSOs from Steffen et al. (2006).

the BLR (Netzer 1990). It may be that a larger region of very dense ($n_e \sim 10^{10} \text{ cm}^{-3}$) material is needed, which could correspond to a disc atmosphere or ‘transition region’ (see e.g. Murray et al. 1995; Knigge et al. 1998b). While modest changes to geometry may permit this, the initial grid search did not find a parameter space in which the Ly α or Mg II EWs were significantly higher (see section 2.4.1). Second, EWs increase with inclination (see Fig. 2.6 and Fig. 2.8; also Fig. 2.10). This is discussed further in section 2.4.2.

2.3.3 X-ray Properties

The main motivation for adding clumping to the model was to avoid over-ionization of the wind in the presence of strong X-rays. Having verified that strong BALs appear in the synthetic spectra, it is also important to assess whether the X-ray properties of this fiducial model agree well with quasar and BALQSO samples for the relevant inclinations.

Fig. 2.9 shows the emergent monochromatic luminosity (L_ν) at 2 keV and plotted against L_ν at 2500Å for a number of different viewing angles in the model. The monochromatic luminosities are calculated from the synthetic spectra and thus include the effects of wind reprocessing and attenuation. In addition to model outputs, I also show the BALQSO sample of Saez et al. (2012) and luminous AGN and quasar samples from Steffen et al. (2006). The best fit relation from Steffen et al. (2006) is also shown. For low inclination, ‘quasar-like’ viewing angles, the model properties are in excellent agreement with AGN samples. The slight gradient from 20° to 60° in the models is caused by a combination of disc foreshortening and limb-darkening (resulting in a lower L_{2500} for higher inclinations), and the fact that the disk is opaque, and thus the X-ray source subtends a smaller solid angle at high inclinations (resulting in a lower L_{2keV} for higher inclinations).

The high inclination, ‘BALQSO-like’ viewing angles show moderate agreement with the data, and are X-ray weak due to bound-free absorption and electron scattering in the wind. Typically, BALQSOs show strong X-ray absorption with columns of $N_H \sim 10^{23} \text{ cm}^{-2}$ (Green & Mathur 1996; Mathur et al. 2000; Green et al. 2001; Grupe et al. 2003). This is often cited as evidence that the BAL outflow is shielded from the X-ray source, especially as sources with strong X-ray absorption tend to exhibit deep BAL troughs and high outflow velocities (Brandt et al. 2000; Laor & Brandt 2002; Gallagher et al. 2006). Our results imply that the clumpy BAL outflow itself can be responsible for the strong X-ray absorption, and supports Hamann et al.’s (2013) suggestion that geometric effects explain the weaker X-ray absorption in mini-BALs compared to BALQSOs.

2.3.4 LoBALs and Ionization Stratification

At high inclinations, the synthetic spectra exhibit blue-shifted BALs in Al III and Mg II – the absorption lines seen in LoBALQSOs – and even show absorption in Fe II at the highest inclinations. Line profiles in velocity space for C IV, Al III and Mg II, are shown in Fig. 2.10 for a range of BALQSO viewing angles. Ionization stratification of the wind causes lower ionization material to have a smaller covering factor, as demonstrated by figures 2.4 and 2.10. This confirms the behaviour expected from a unification model such as Elvis (2000). LoBALs are only present at viewing angles close to edge-on ($i > 75^\circ$),

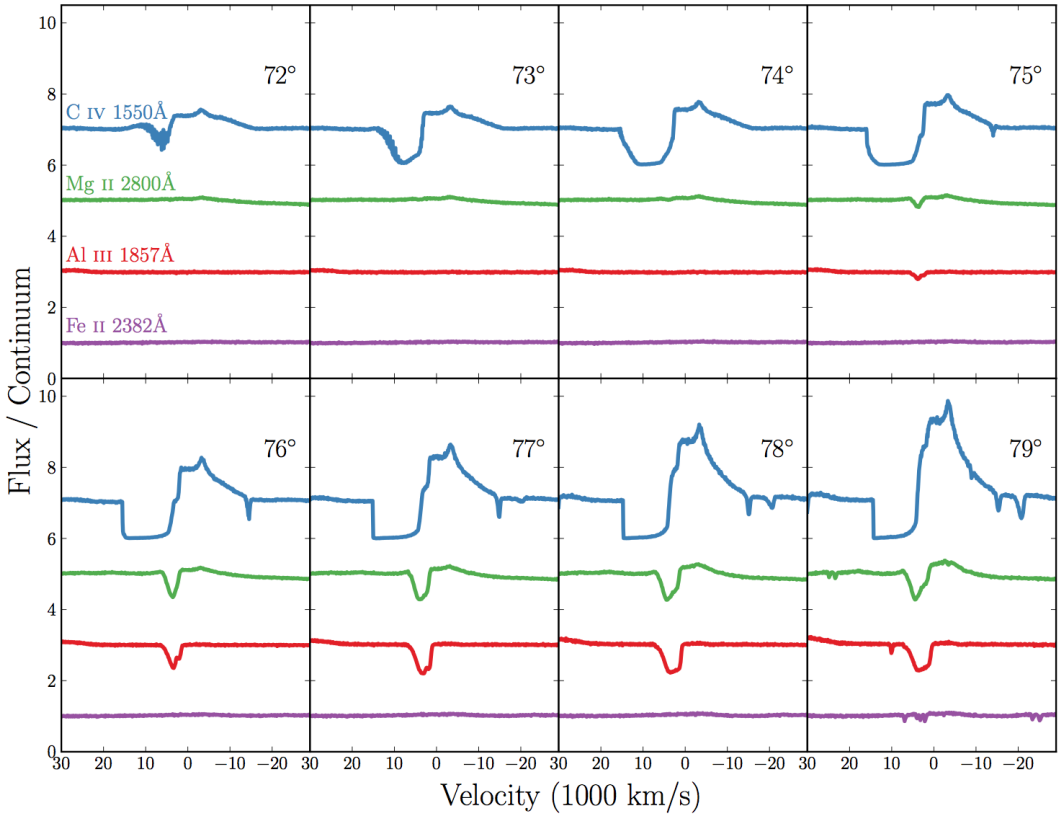


FIGURE 2.10: C IV, Mg II, Al III and Fe II line profiles for viewing angles from 72° – 79° . The profiles are plotted relative to the local continuum with an offset applied for clarity. Lower ionization profiles appear at a subset of high inclinations, compared to the ubiquitous C IV profile.

as predicted by polarisation results (Brotherton et al. 1997). As observed in a BALQSO sample by Filiz Ak et al. (2014), the model BAL troughs are wider and deeper when low ionization absorption features are present, and high ionization lines have higher blue-edge velocities than the low ionization species. There is also a correlation between the strength of LoBAL features and the amount of continuum attenuation at that sightline, particularly blueward of the Lyman edge as the low ionization base intersects the line-of-sight. A model such as this therefore predicts that LoBALQSOs and FeLoBALQSOs have stronger Lyman edge absorption and are more Compton-thick than HiBALQSOs and Type 1 quasars. An edge-on scenario also offers a potential explanation for the rarity of LoBAL and FeLoBAL quasars, due to a foreshortened and attenuated continuum, although BAL fraction inferences are fraught with complex selection effects (Goodrich 1997; Krolik & Voit 1998).

2.4 Discussion

2.4.1 Parameter Sensitivity

Having selected an individual fiducial model from the simulation grid, it is important to briefly explore how specialised this model is, and how small parameter changes can affect the synthetic spectra. Fig. 2.11 shows the EW at a low inclination, and BI at a high inclination for the simulation grid. A few conclusions can be drawn from this plot straight away. First, almost all the models with $f_V = 0.1$ are over-ionized, and fail to produce strong C IV BALs or emission lines. Second, it is difficult to significantly increase line emission while keeping the luminosity and mass loss rate of the system fixed. I show an additional point on figure 7 corresponding to a model with an order of magnitude higher X-ray luminosity and double the mass loss rate. As expected, this results in far higher line EWs, but fails to produce BALs because the collisionally excited emission swamps the BAL profile. In addition, this model would lie well above the expected $L_{2kev} - L_{2500}$ relation in figure 5. Such a high X-ray luminosity could therefore not be the cause of the strong line emission seen in *all* Type 1 quasars.

The parameter search presented here is by no means exhaustive, and conclusions may be limited by the specific parameterisation of the outflow kinematics used. Nevertheless, I suggest that the angular distribution of both the line and continuum emission is perhaps the crucial aspect to understand. With this in mind, obtaining reliable orientation indicators appears to be a crucial observational task if we are to further our understanding of BAL outflows and their connection, or lack thereof, to the broad line region.

2.4.2 Inclination Trends: FWHM and EW

EW increases with inclination in the fiducial model. This trend means that even though significantly denser models can match the line EWs fairly well at low inclinations, they will then possess overly strong red wings to the BAL P-Cygni profiles at high inclinations. The fact that the EW increase in this model are directly related to limb-darkening and foreshortening of the continuum. This appears to contradict observations, which show remarkably uniform emission line properties in quasars and BALQSOs (Weymann et al. 1991; DiPompeo et al. 2012a).

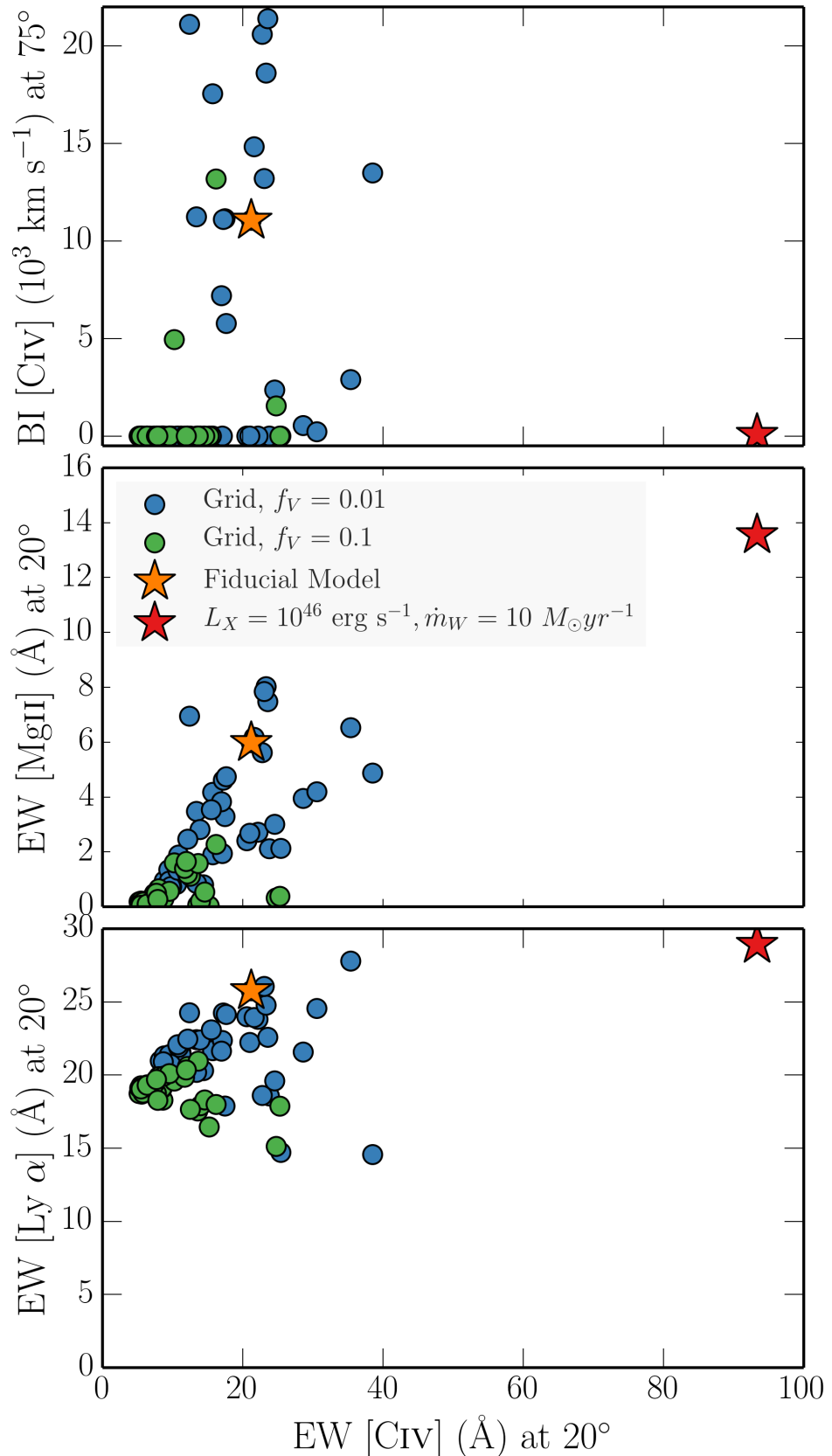


FIGURE 2.11: The EW of the C IV 1550 Å line at 20° plotted against a) the BI of C IV 1550 Å at 75°, b) the EW of the Mg II 2800 Å line at 20° and c) the EW of Ly α at 20°. The circles correspond to the simulation grid for two different values of f_V , and the fiducial model is marked with an orange star. I also show a higher X-ray luminosity model and a higher mass loss rate with a red star.

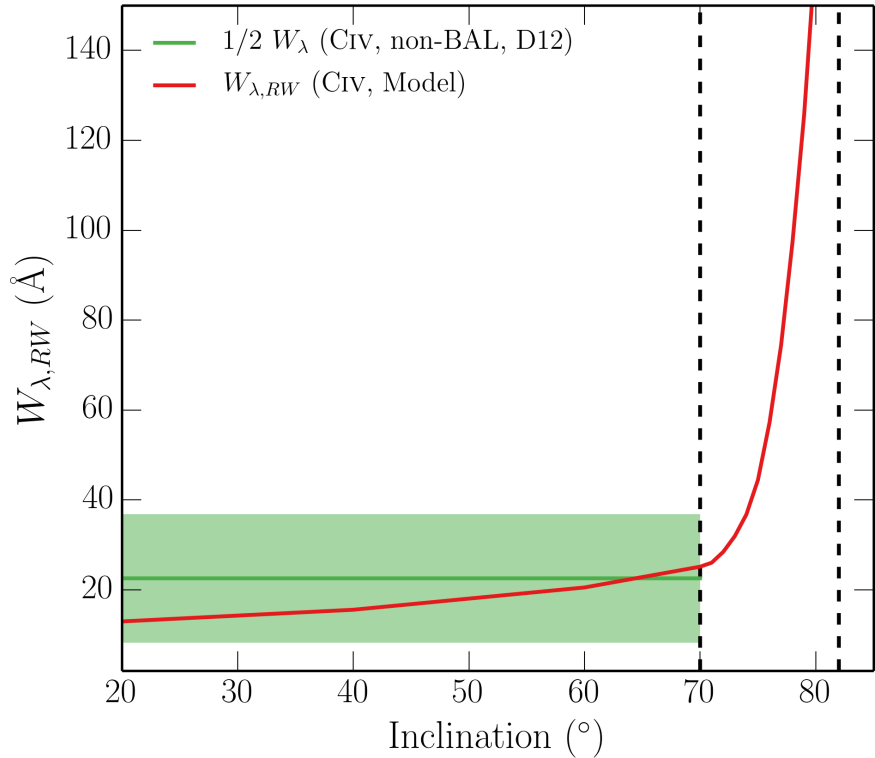


FIGURE 2.12: $W_{\lambda,RW}$ as a function of inclination in the fiducial model, compared to $1/2$ EW from the quasar sample of Di Pompeo et al. (2012; D12).

In order to quantitatively assess how emission lines change with inclination when blue-shifted absorption may affect the line profile, I define the ‘red wing equivalent width’ ($W_{\lambda,RW}$) as

$$W_{\lambda,RW} = \int_{\lambda_0}^{\lambda'} \left(1 - \frac{F_\lambda}{F_0} \right) d\lambda \quad (2.5)$$

where F_0 is the continuum flux and the integral is calculated from λ_0 , line centre, to a wavelength λ' where the flux has returned to the continuum level. This quantity is shown as a function of inclination in Fig. 2.12 for the C IV UV line. The $W_{\lambda,RW}$ expected from isotropic line emission and a foreshortened and limb darkened disc and $1/2$ equivalent widths from DiPompeo et al. (2012a) are also shown.

The variation of EW with inclination is significantly larger than the variation across the quasar population. The angular distribution of the disc continuum and line emission is clearly crucially important in determining the emergent broad line EWs, as suggested by, e.g., the analysis of Risaliti et al. (2011). I shall explore this question further in chapter 6.

2.4.2.1 FWHM and Black Hole Mass Estimates

In a recent study, [Yong et al. \(2016\)](#) used the SV93 wind prescription assess the variation of full-width at half-maximum (FWHM) of H β (and resultant BH mass estimates) with inclination in a disc wind model. Although their model is fairly simple – it does not include, for example, full radiative transfer or ionization physics – this analysis still gives interesting insights into how emission lines from a disc wind might bias BH mass estimates.

If the BLR gas is virialised, as often assumed, then the black hole mass is related to the velocity dispersion, Δv , of the gas by

$$M_{BH} = f \frac{\Delta v^2 R_{BLR}}{G}, \quad (2.6)$$

where R_{BLR} is some appropriate emissivity-weighted radius and is often either assumed, estimated from ionization arguments or calculated from reverberation mapping. When using FWHM to estimate the velocity dispersion the above equation can be rewritten as

$$M_{BH} = f_{FWHM} \left[c \frac{(FWHM)}{\lambda_0} \right]^2 \frac{R_{BLR}}{G}, \quad (2.7)$$

where λ_0 is the central wavelength of the line in question and the FWHM is in the same wavelength units. In a model such as this the BH mass is known, and determines the escape velocities and rotational motions of the outflow. Thus, using a typical radius for line formation in the model it is trivial to calculate f_{FWHM} for each viewing angle. Fig. 2.13 shows f_{FWHM} as a function of inclination for the C IV, Mg II and H α emission lines in the fiducial model, assuming $R_{BLR} = 10^{17}$ cm. For C IV and Mg II the wind angles are not plotted as BAL profiles affect the measurement, and I have compared to H α rather than H β due to the low H β luminosity at some viewing angles. Nevertheless, this value should trace f_{FWHM} from H β fairly well.

The values from the model presented here agree fairly well with the predictions of [Yong et al. \(2016\)](#) from their simpler analysis, suggesting that, at least in this specific set-up, radiative transfer and ionization has a minimal role in determining the emergent FWHM. Instead, the effect is dominated by velocity projection effects. The reason for the significantly lower values for Mg II is that it is actually formed well inside $R_{BLR} =$

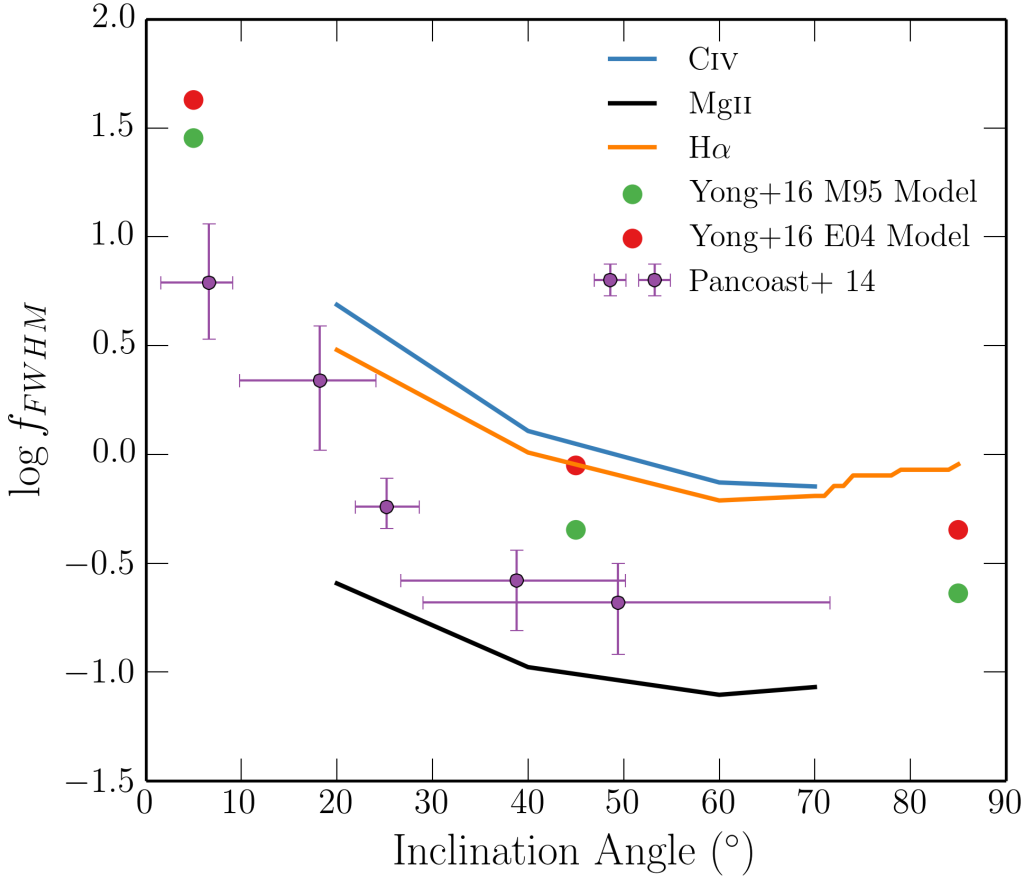


FIGURE 2.13: f_{FWHM} as a function of inclination from the fiducial model for three different lines, compared to values from Yong et al. 2016 and Pancoast et al. 2014.

10^{17} cm, highlighting the dangers of using a single BLR radius for BH mass estimates from different lines.

2.5 Summary And Conclusions

I have carried out MCRT simulations using a simple prescription for a biconical disc wind, with the aim of expanding on the work of H13. To do this, two main improvements were necessary: First, I included a simple treatment of clumping, and second, the modelling of recombination lines was improved by treating H and He as ‘macro-atoms’. Having selected a fiducial model from an initial simulation grid, I assessed the viability of such a model for geometric unification of quasars, and found the following main points:

1. Clumping moderates the ionization state sufficiently to allow for the formation of strong UV BALs while agreeing well with the X-ray properties of luminous AGN and quasars.
2. A clumpy outflow model naturally reproduces the range of ionization states expected in quasars, due to its stratified density and temperature structure. LoBAL line profiles are seen at a subset of viewing angles, and Fe II absorption is seen at particularly high inclinations.
3. The synthetic spectra show Ly α line and weak He II 1640Å line as a result of the improved treatment of recombination using macro-atoms. Balmer emission lines and a Balmer recombination continuum are also seen in the optical spectrum, but this is only really significant at high inclination where the continuum is suppressed.
4. The higher X-ray luminosity causes a significant increase in the strength of the collisionally excited emission lines produced by the model. However, the equivalent-width ratios of the emission lines do not match observations, suggesting that a greater volume of dense ($n_e \sim 10^{10} \text{ cm}^{-3}$) material may be required.
5. The line EWs in the synthetic spectra increase with inclination. BAL and non-BAL quasar composites have comparable EWs, so the fiducial model fails to reproduce this behaviour. If the BLR emits fairly isotropically then for a foreshortened, limb-darkened accretion disc it is not possible to achieve line ratios at low inclinations that are comparable to those at high inclinations. I suggest that understanding the angular distribution of line and continuum emission is a crucial question for theoretical models.

This work confirms a number of expected outcomes from a geometric unification model, and suggests that a simple biconical geometry such as this can come close to explaining much of the phenomenology of quasars. However, these conclusions pose some challenges to a picture in which BALQSOs are explained by an *equatorial* wind rising from a classical thin disc, and suggest the angular distribution of emission is important to understand if this geometry is to be refuted or confirmed. I suggest that obtaining reliable observational orientation indicators and exploring a wider parameter space of outflow geometries in simulations are obvious avenues for future work.

Chapter 3

Quasar Emission Lines as Probes of Orientation and Unification

This chapter is based on a paper in preparation:

Matthews J. H., Knigge C., ‘Quasar Emission Lines as Probes of Orientation and Unification’, to be submitted to MNRAS.

3.1 Introduction

In the previous chapter, I presented tests of geometric unification models using MCRT and photoionization simulations. One of the key results from that analysis is that trends with inclination prohibit models with equatorial outflows matching observations, as the EW of the emission lines tend to increase with inclination. This trend has clear implications for the geometries of BAL outflows; the viewing angle may determine many of the selection effects at work and must therefore be understood before the true covering factor of BAL outflows can be accurately determined. The covering factor and opening angle of the outflow are important quantities to measure in order to calculate the feedback efficiency (e.g. [Borguet et al. 2012](#)), and make inferences about the outflow physics (e.g. [Proga 2005](#)).

Unlike in galactic accretion disc systems, measuring inclinations for quasars and AGN is notoriously difficult, and obtaining reliable orientation indicators is thus an important

observational goal for the community. Perhaps as a result of this problem, directly opposing geometries have been proposed for BAL outflows (see section ??). Here, I use observational data from the Sloan Digital Sky Survey to constrain the inclinations of BAL quasars. Similar attempts have been made previously with different diagnostics; for example, by considering radio properties (Zhou et al. 2006; DiPompeo et al. 2012b), polarisation (Brotherton et al. 2006) and general emission line properties (DiPompeo et al. 2012a).

This chapter is structured as follows. First, I describe the data sample and selection criteria being used. I begin by simply examining the distributions of the EW of the O III 5007Å emission line, EW[O III], and comparing the BAL and non-BAL quasar distributions. In section 3.3 I review the angular distribution of continuum emission one would expect from simple α -disc models, as well as exploring the same quantity in more advanced disc models computed with AGNSPEC. I then use these theoretical angular distributions applied to a simple toy model in section 3.4, and conduct MC simulations in an attempt to fit the observed BAL and non-BAL quasar distributions of EW[O III], using a similar approach to Risaliti et al. (2011, hereafter R11). In section 3.5 I discuss the results in the context of radio and polarisation measurements of AGN, as well as exploring the location of BAL quasars in ‘Eigenvector 1’ parameter space. Finally, in section 3.6, I summarise the findings.

3.2 Data Sample

The data sample is based upon the Shen et al. (2011, hereafter S11) catalog of 105,783 quasars from the The Sloan Digital Sky Survey (SDSS) Data Release 7 (DR7). As I will use emission line diagnostics in this study, this sample must be further divided according to which emission lines are present in the SDSS wavelength range at a given redshift. Sample A contains all quasars within the redshift range $0.35 < z < 0.83$, such that the Mg II 2800A and O III 5007Å line EWs are both measured, and Mg II BAL identification is possible. Sample B contains all quasars within the redshift range $1.45 < z < 2.28$, such that the EWs and presence of BALs in Mg II 2800A and CIV 1550A are both measurable. The details of these samples are shown in table 1.

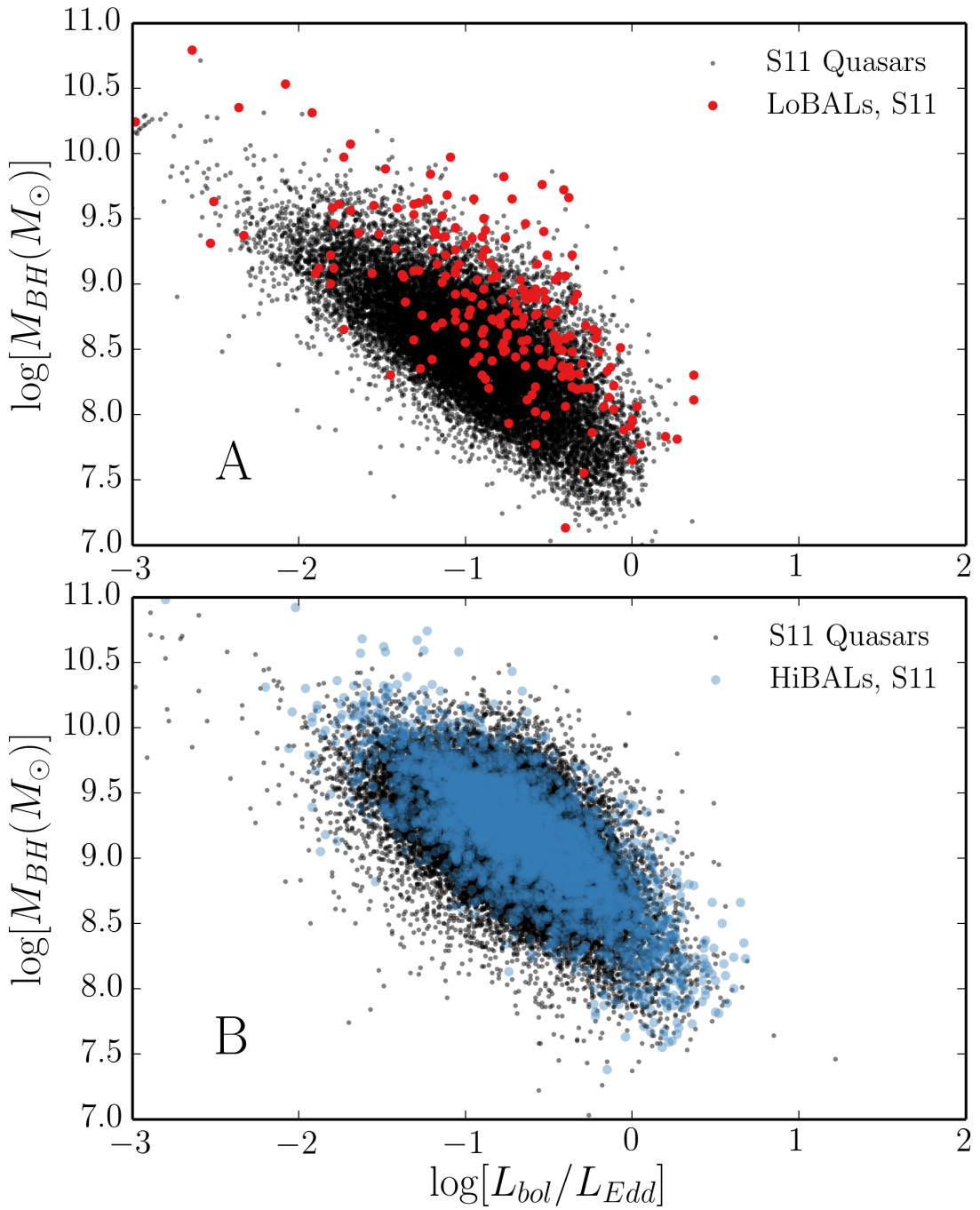


FIGURE 3.1: BH mass and Eddington fraction for the BAL samples plotted over the overall quasar sample from S11.

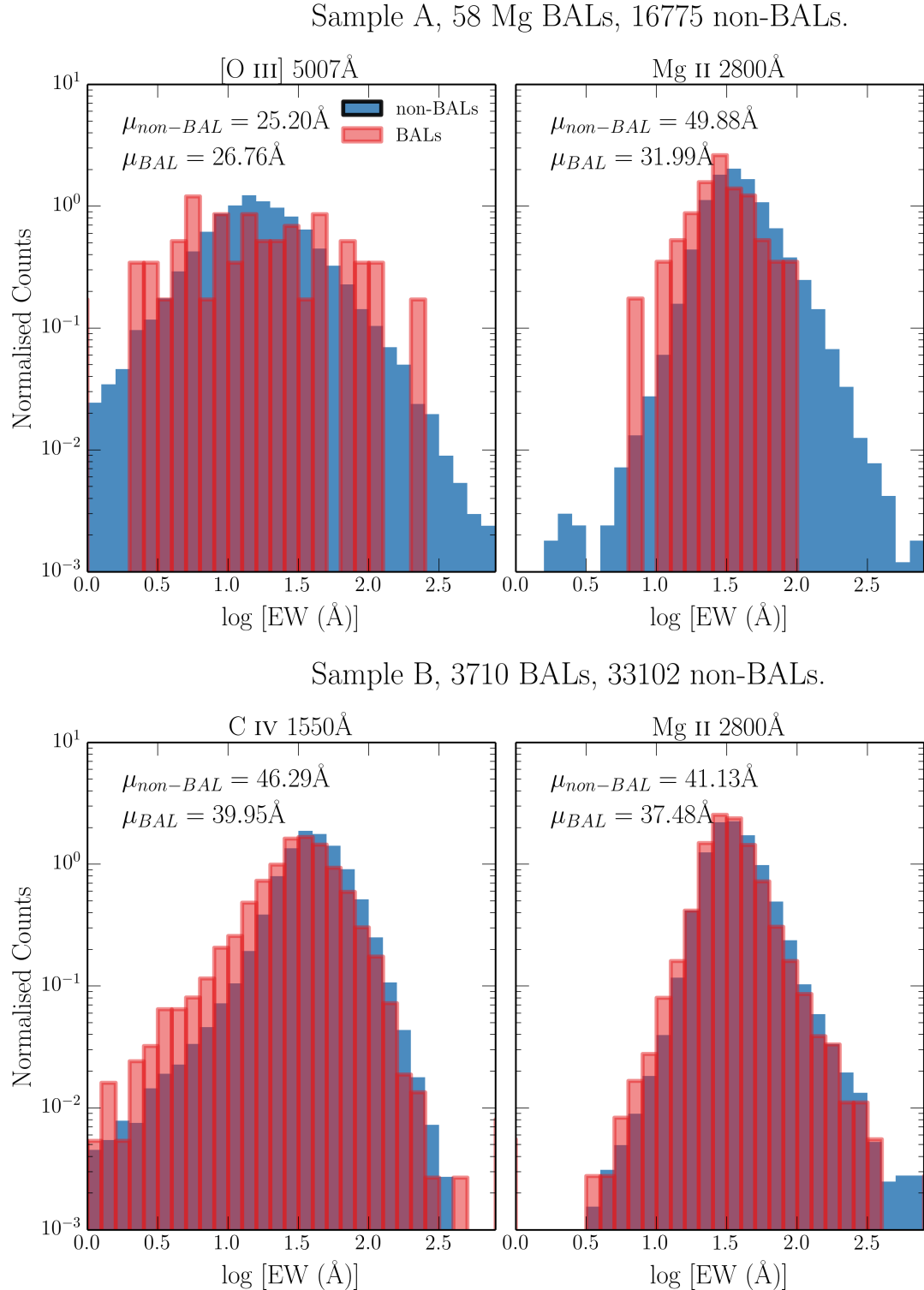


FIGURE 3.2: Histograms of equivalent widths for three emission lines from the two different samples.

In attempting to draw broad conclusions about unification models as a whole, we would like to be able to construct a large homogenous dataset of *HiBAL* and non-BAL quasars, both with O III 5007Å EWs. Unfortunately, the wavelength limits of SDSS do not allow this. One of the problems with using just LoBAL quasars as tests of unification is that there is evidence that they are drawn from a different population than normal quasars, perhaps suggesting an *evolutionary* origin. Examples include anomalously high LoBAL fractions in dust-reddened quasar samples ([Urrutia et al. 2009](#)) and infra-red selected samples ([Dai et al. 2012](#)); although see also [Lazarova et al. \(2012\)](#)). To partially address this issue, I also build a small sample of HiBAL quasars in SDSS by cross-matching the S11 catalog with BALs identified in the HST COS archive. BALs were selected from the COS spectra using the balnicity index, BI , defined in equation ???. HST objects were designated as HiBALS by satisfying the condition that $BI > 0$ in one of CIV, NV, SiIV. The mass and Eddington fraction measurements from S11, with errorbars, are shown against the background distribution of all quasars.

Fig. 2 shows histograms of a number of different emission line properties for samples A and B. As discussed by previous authors (e.g. [Weymann et al. 1991](#)), I find that BAL and non-BAL quasars really do seem to possess very similar emission line properties. The EW is related to the ‘face-on’ equivalent width, EW_0 by the equation

$$EW = EW_0 / \epsilon(\theta) \quad (3.1)$$

where θ is the viewing angle with respect to the symmetry axis and $\epsilon(\theta)$ is the ‘angular emissivity function’, which describes how the continuum luminosity from the disc varies as a function of viewing angle. For a foreshortened disc this is simply $\epsilon(\theta) = \cos \theta$.

Thus, if BAL quasars are viewed from a larger viewing angle on average then one would expect them to possess higher EWs, with a broader distribution. It is already apparent from figure 1 that the BAL distribution mean is not systematically higher than the non-BAL mean – in fact, it is lower. This is not expected from a model in which the continuum is foreshortened and BAL outflows are at all equatorial. This problem is examined further in section 3.4. First, I will examine the motivations for different forms of $\epsilon(\theta)$ in AGN and quasars.

3.3 The Angular Distribution of Emission from an Accretion Disc

The most widely-used theoretical model for an accretion disc was proposed by Shakura & Sunyaev (1973; hereafter SS73). There are a number of well-documented problems when fitting AGN SEDs with SS73 accretion disc models (REFs), and there are also tensions with the ‘accretion disc size’ relation from time lags (Edelson et al. 2015) and microlensing (Morgan et al. 2010). Despite these problems, Capellupo et al. (2015) recently had some success fitting VLT XSHOOTER spectra of AGN when the effects of GR, mass-loss and comptonisation were included. In this section, I start by discussing the angular distribution of emission from an SS73 disc, before discussing opacity and GR effects. In order to explore these effects, I use AGNSPEC (Hubeny et al. 2000; Davis & Hubeny 2006; Davis et al. 2007). I stress that the discussion here is not limited to SS73 discs; the only real condition for the expected angular distributions derived here is that the disc is geometrically thin and optically thick.

3.3.1 Standard Thin Disc Models

Any geometrically thin, optically thick disc will appear foreshortened and limb darkened (if temperature decreases with height from the central disc plane). Foreshortening is a simple $\cos \theta$ geometric effect, where θ is the inclination with respect to the vertical z axis, which is perpendicular to the disc plane. Limb darkening, $\eta(\theta)$, is given by

$$\eta(\theta) = a(1 + b \cos \theta), \quad (3.2)$$

where a is a normalisation constant and b governs the strength of the limb darkening. $b = 3/2$, known as the Eddington approximation tends to give good agreement with solar observations (e.g. Mihalas 1978). The two effects can be combined to give an angular emissivity function, of

$$\epsilon(\theta) = a \cos \theta \left(1 + \frac{3}{2} \cos \theta\right). \quad (3.3)$$

3.3.2 Including GR, Comptonisation and Opacity Effects

In reality, limb darkening is not frequency independent and depends on the bound-free and bound-bound opacities in the disc. In addition, it has been shown that GR can ‘isotropize’ the radiation field in XRBs (Zhang et al. 1997; Muñoz-Darias et al. 2013), in some cases overcoming foreshortening effects. To assess the impact of GR and disc opacities on $\epsilon(\theta)$ I use AGNSPEC models, which uses stellar atmosphere calculations to calculate the SED in a series of annuli, before using the KERRTRANS code to calculate the emergent SED by ray-tracing along Kerr geodesics. Fig. 3.3 shows $\epsilon(\theta)$ as a function of θ for AGNSPEC models for minimally and maximally spinning BHs, compared to foreshortened and limb-darkened predictions for SS73 models. Clearly, there is very little effect; the accretion disc is still strongly anisotropic in the relevant wavebands.

3.4 Predicted EW Distributions Compared to Observations

3.4.1 Fitting the Quasar Distribution

Risaliti et al. (2011, hereafter R11) analysed the EW[O III] distribution of 6029 quasars in SDSS DR5. They demonstrated that a foreshortened disc and isotropic O III 5007Å line produces a high EW tail to the distribution with a characteristic slope of $\Gamma_{EW} = -3.5$. In order to first reproduce their result and discuss its implications, I have created a sample according to their selection criteria. The criteria are that the object in question lies in the redshift range 0.01 to 0.8, have an absolute magnitude $M_i > 22$, an apparent magnitude $m_i > 19.1$, and signal to noise per pixel of greater than 5. Using the updated SDSS quasar sample of S11, this defines a sample of 14,424 quasars.

To fit the distribution, I conduct the following procedure, which is similar to the method R11 use to demonstrate that the power law tail is expected.

1. A set of isotropic angles is chosen such that $P(\theta) \propto d\Omega(\theta)$. If $\theta < \theta_1$ then the fake object is designated as unobscured, and otherwise the object is ignored.

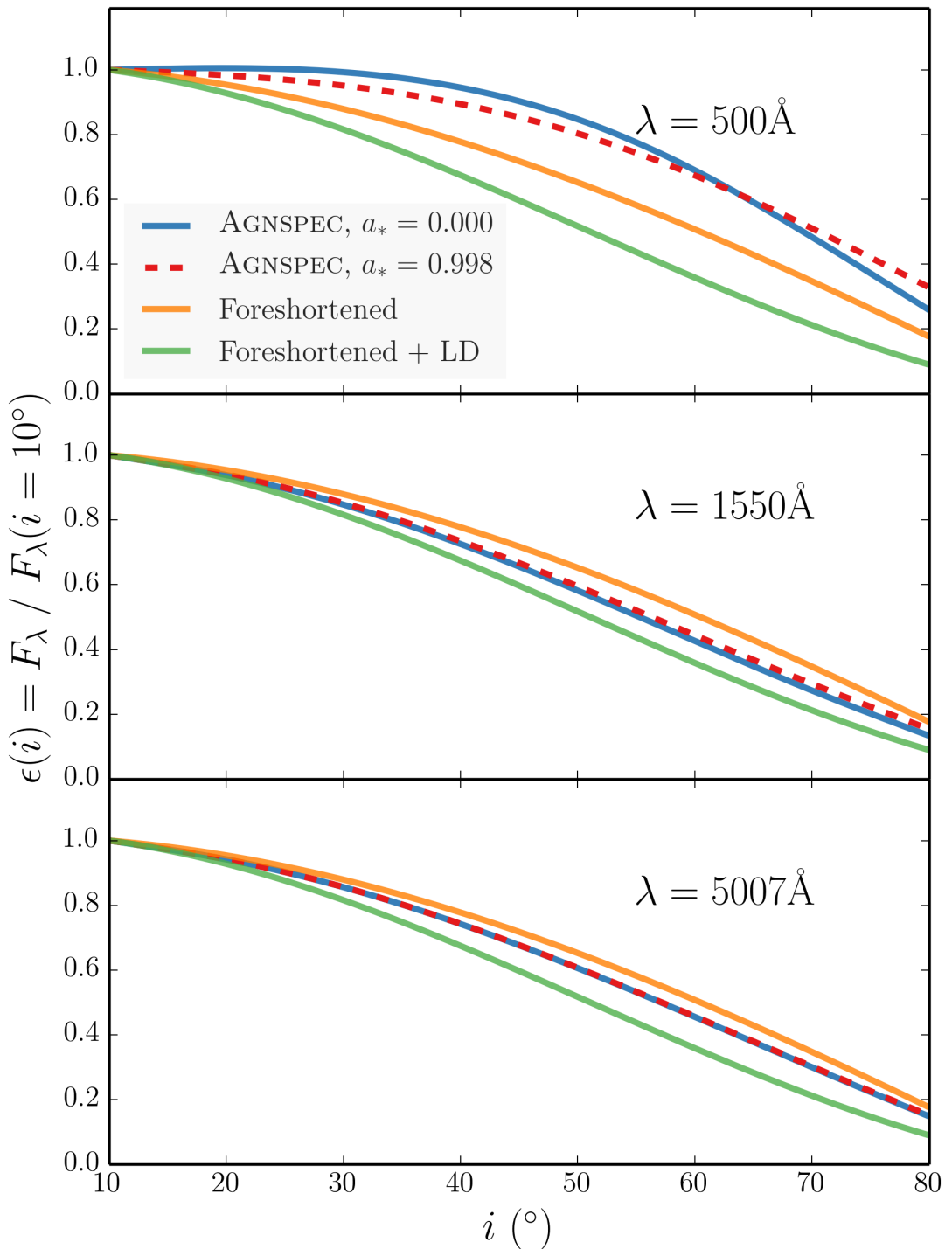


FIGURE 3.3: Monochromatic continuum luminosities from AGNSPEC and classical thin disc models.

2. To be included in the sample, the object also has to survive a selection test to simulate the distribution of angles in a flux-limited sample. This is done by drawing a random sample from the real quasar sample, and calculating a ‘doubly observed continuum flux’, F_O at 5100\AA (rest frame), such that $F_O = F_{5100} \epsilon(\theta)$. The flux limit is set at $5 \times 10^{-13} \text{ erg s}^{-1} \text{ cm}^{-1} \text{ \AA}^{-1}$, but the results are fairly insensitive to the limit chosen.
3. For each mock sample, an EW_* is drawn from an intrinsic (i.e. ‘face-on’) EW distribution for quasars. This is assumed to be a gaussian. The mean, μ_* , and width, σ_* , of this Gaussian can either be set arbitrarily – for example, to demonstrate trends in mock data – or obtained from a χ^2 fit to the observed EW distribution.
4. A mock EW is estimated such that $\text{EW} = \text{EW}_0/\epsilon(\theta)$, and this process is repeated to build up a mock sample of 10^6 objects.

The result of this numerical experiment is, as found by R11, a distribution with a high EW tail of slope -3.5 . We can now vary the maximum angle, θ_1 , and examine how this tail changes. Mock data for a series of cutoff angles is shown in Fig. ??, for two intrinsic Gaussians. The power law behaviour is only seen when the maximum angle is sufficiently large, and a rapid decay in the distribution is observed at a characteristic EW related to both the width and mean of the intrinsic distribution as well as the cosine of the maximum angle. The top panel has μ_* and σ_* of the R11 Model 1, whereas the bottom panel shows a narrower distribution to illustrate the earlier onset of the high EW cutoff. In principle, this cutoff could be used to infer information about the viewing angle distribution of quasars, but this is complicated by poor statistics in the tail, selection effects and lack of knowledge about the true face-on distribution.

Fig. 3.5 shows the result of a χ^2 minimization fit to the R11 sample. A good fit is achieved with similar values to the intrinsic gaussian than those used by R11.

3.4.2 Comparing non-BAL and BAL Distributions

In order to compare the observed distributions to those expected for BALs and non-BALs I repeat the process described in section ?? with a few key differences

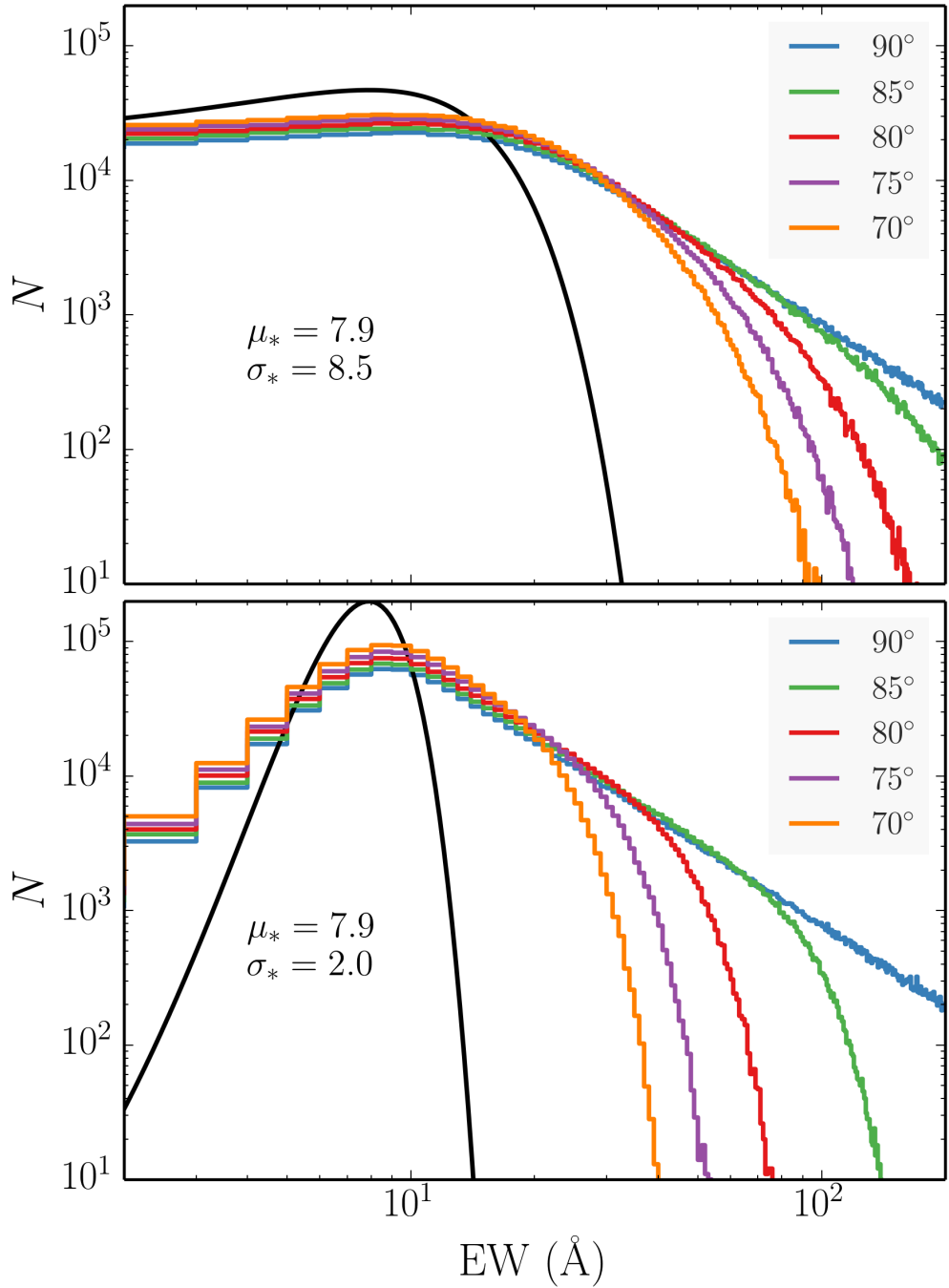


FIGURE 3.4: Theoretical Ew distributions from the numerical experiment described in section ?? for a few different maximum angles. The results in the top panel use the same intrinsic distribution as Model 1 from R11 (shown in black), whereas the bottom panel shows the distributions obtained from a narrower intrinsic Gaussian. By the time the maximum angle is limited to around 70° the cutoff is clear even at moderate values of EW.

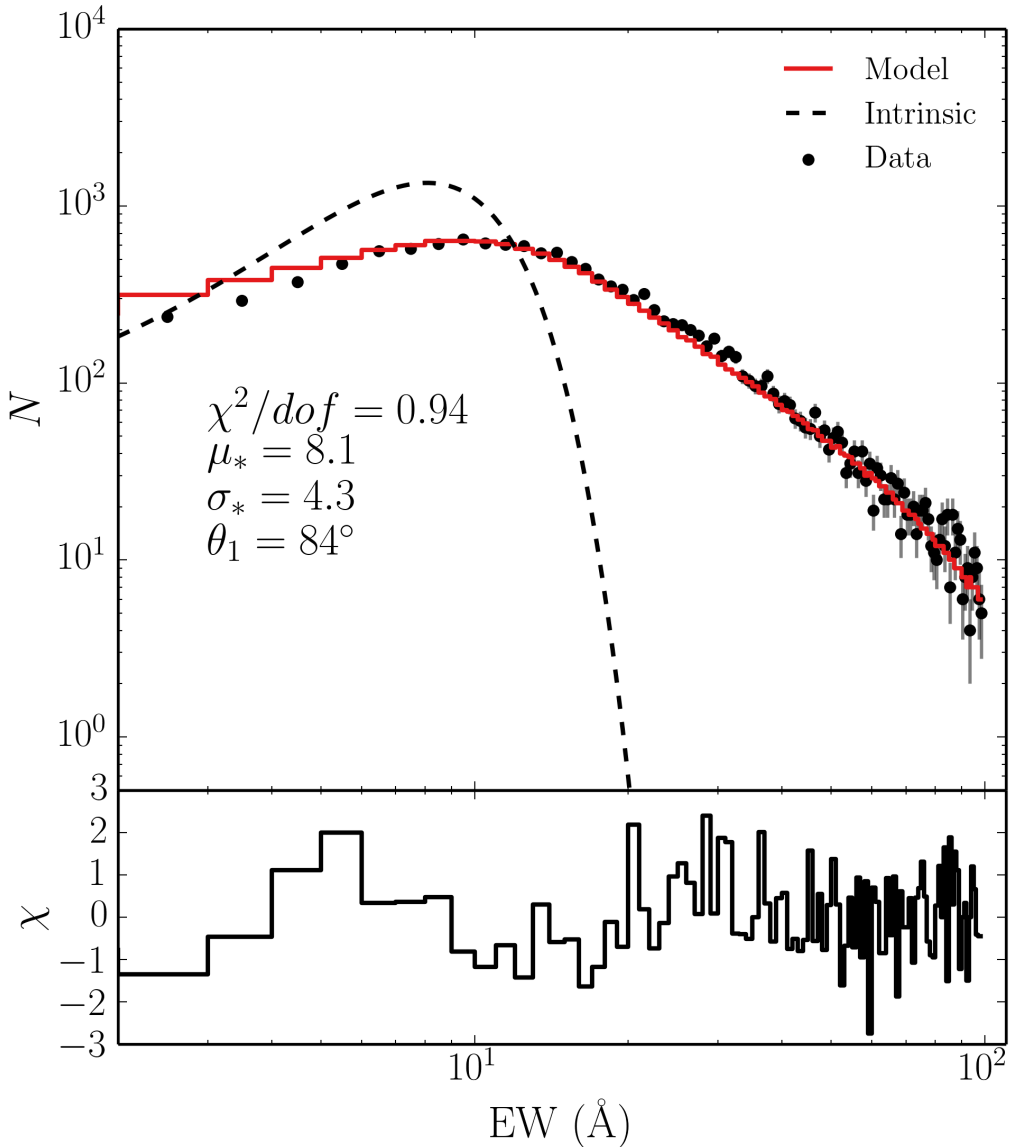


FIGURE 3.5: The EW distribution of quasars in the R11 sample (red errorbars) and the best fit model with a maximum viewing angle of 84°.

I assume $\epsilon(\theta) = \cos \theta$, as this is the conservative estimate from section 3.3. The Monte Carlo simulation undergoes the following steps:

1. A set of isotropic angles is chosen such that $P(\theta) \propto d\Omega(\theta)$. If $\theta_{min} < \theta < \theta_{max}$ then the fake object is flagged as a mock BAL. If $\theta < \theta_{min}$ then the fake object is designated a non-BAL, and otherwise the object is ignored. To be included in the sample, the object also has to survive a selection test based on a arbitrary flux selection limit, to simulate the distribution of angles in a flux-limited sample.

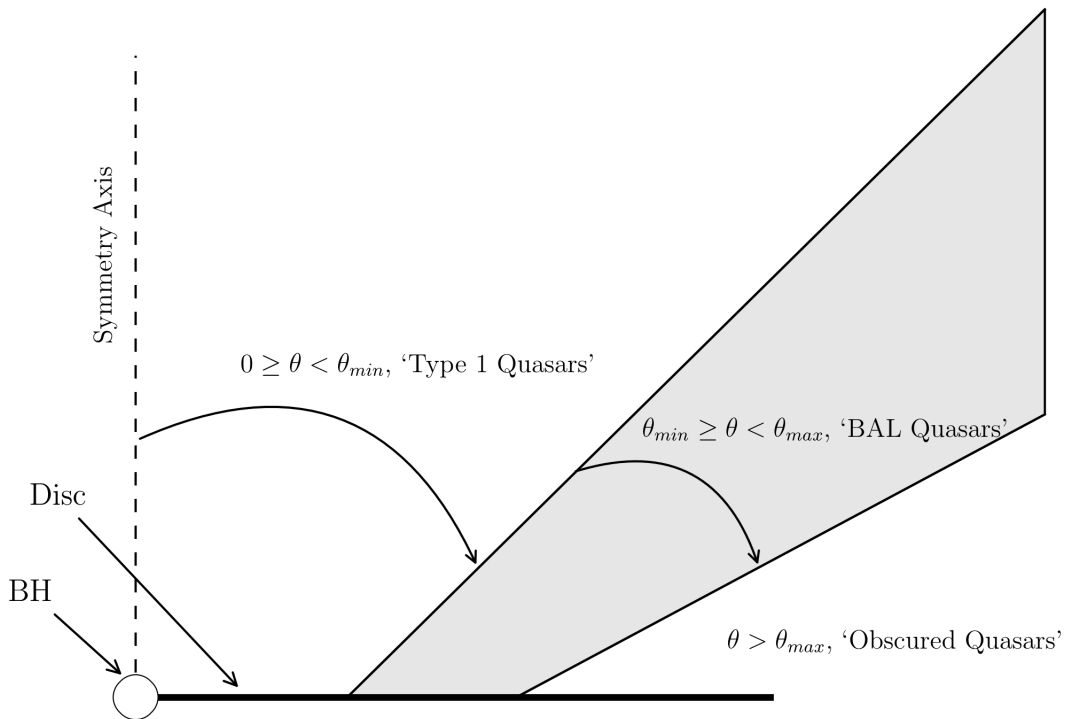


FIGURE 3.6: The geometry of the toy model used to carry out the Monte Carlo simulations

2. I then construct a best estimate of the intrinsic (i.e. ‘face-on’) EW distribution for non-BAL quasars. This is done via a χ^2 minimisation, by finding the gaussian with μ and σ which best reproduces the observed distribution when convolved with the non-BAL angles generated in the previous step. a χ^2 minimisation.
3. For each mock sample, a EW_0 is drawn from the intrinsic gaussian.
4. A mock EW is estimated such that $EW = EW_0/\epsilon(\theta)$, and this process is repeated to build up a mock sample of objects.
5. The number of objects in the mock sample with $\theta_{min} < \theta < \theta_{max}$ is recorded, providing an estimate of the expected BAL fraction for this wind geometry. This already includes a selection effect for the weaker continuum flux.
6. The value of the K-S test statistic is recorded, in which the mock BAL sample is compared to the real BAL sample. The mean and variance of the mock sample is

also recorded. This allows us to ascertain which regions of parameter space best fit the observed BAL distribution

This process is repeated for a grid of θ_{min} and θ_{max} . The results are shown in figure 3.7, in which the mean, standard deviation and f_{BAL} are shown as a function of θ_{min} and θ_{max} . First, I find that the quasar EW distribution cannot be well-fitted unless quasars are viewed from a wide range of angles, right up to edge-on. The best fit is obtained for $\theta_{min} = 85^\circ$ and is shown in Fig. 3.5.

Although the quasar EW distribution can be fitted with the above model, neither the true distribution of viewing angles or the intrinsic ‘face-on’ EW distribution of the emission line in question is known. If an intrinsic, face-on distribution could be constructed then the Kolmogorov-Smirnov test and χ^2 minimization could be used to place constraints placed on BAL and non-BAL viewing angles. Furthermore, the distribution of C IV quasar EW cannot

Despite these difficulties, it is still relatively easy to demonstrate that the EW distribution in BAL quasars is not well produced by a model in which the accretion disc is foreshortened and BAL quasars are viewed from high inclinations. I will show this by conducting a simple Monte Carlo experiment to ascertain which geometries best reproduce the observed distributions. Throughout these simulations,

3.4.3 EW[O iii] in LoBAL quasars

As expected, equatorial viewing angles are strongly disfavoured, and furthermore, it is only possible to fit the tail to the EW[O III] distribution if non-BAL quasars are allowed to be viewed from high inclinations. However, any conclusions are somewhat limited by the lack of knowledge about the intrinsic face-on distribution of EW[O III], or equivalently, the orientations of the quasars themselves. If either of these quantities were known then specific viewing angles of BAL outflows could be

An additional limitation is due to the SDSS wavelength coverage and means that only LoBALs can be used when EW[O III] is present. I would suggest that future observational programs might look to build up a large sample of EW[O III] measurements for HiBAL quasars. In the mean time, I will turn to the UV broad emission lines to examine if the above conclusions also hold sway when it is possible to consider HiBAL quasars.

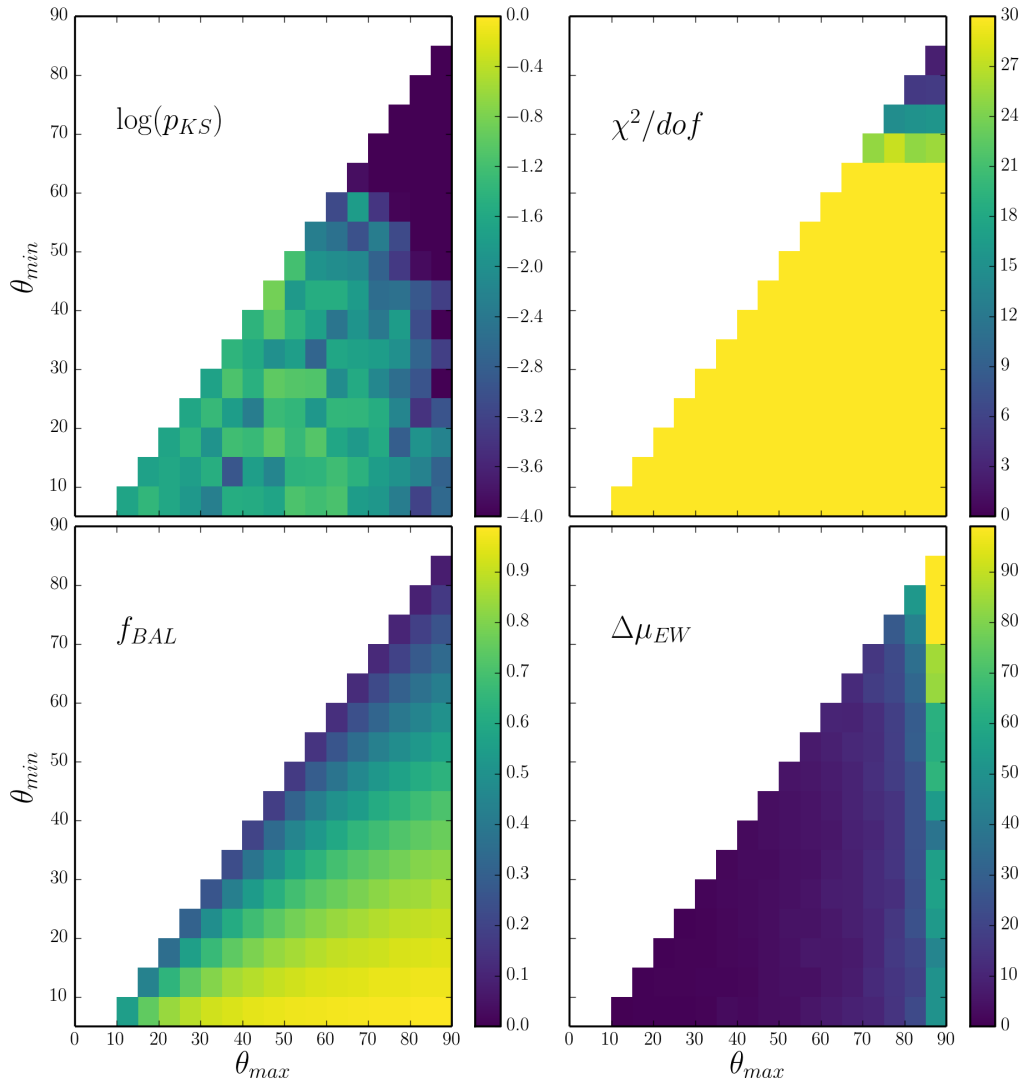


FIGURE 3.7: Heatmap showing the results

3.4.4 Broad Emission Lines in HiBAL quasars

The situation involving broad emission lines is somewhat different, as the lines are dipole permitted transitions and can thus be optically thick.

3.5 Discussion

I have demonstrated that the EW distributions of the O III 5007Å emission line in quasars is not consistent with a model in which BAL quasars are viewed from equatorial angles and the continuum emission originates from a foreshortened accretion disc. This conclusion would be strengthened were I to include limb darkening. This conclusion

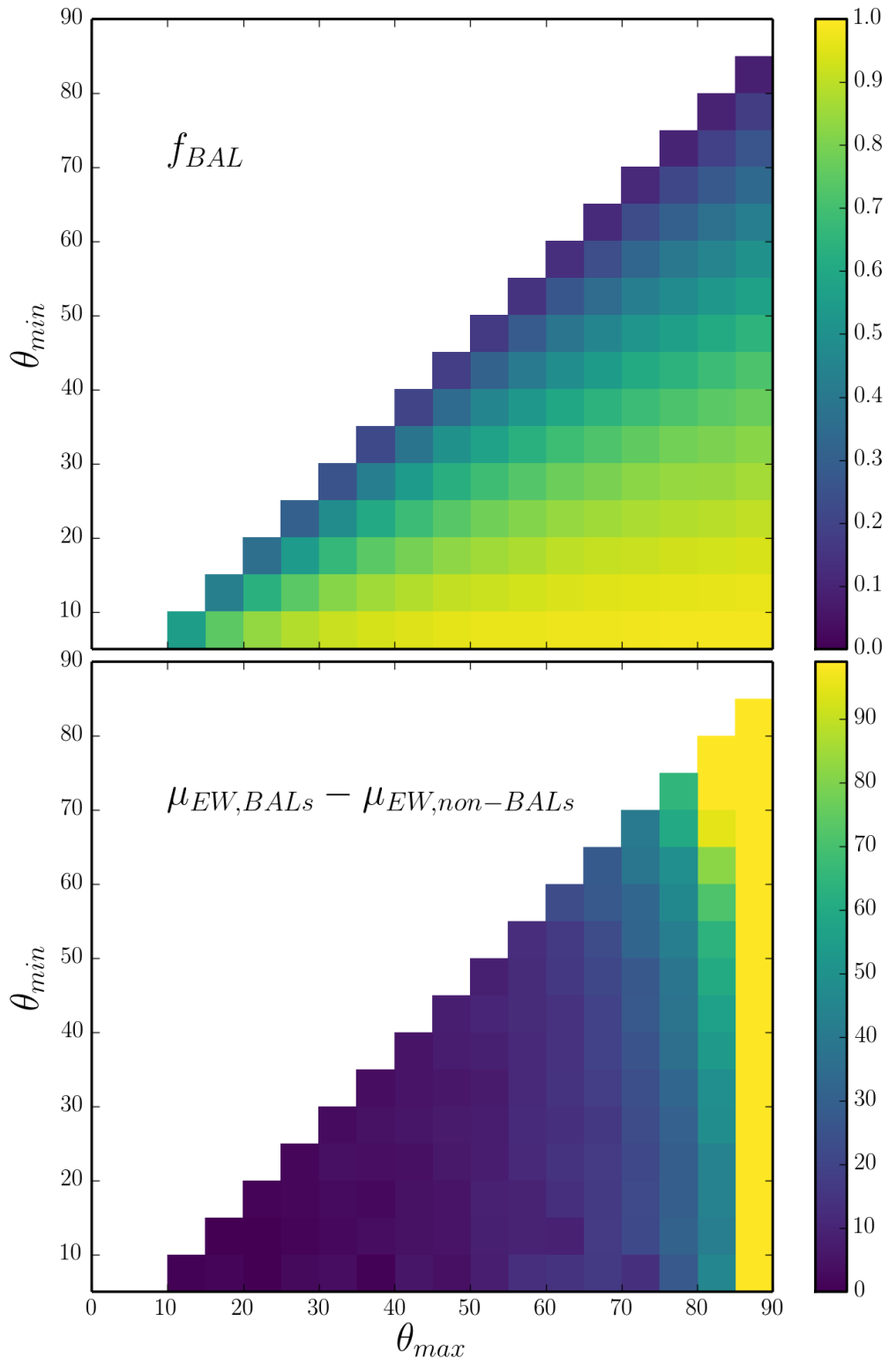


FIGURE 3.8: Contour plots from the Monte Carlo simulations.

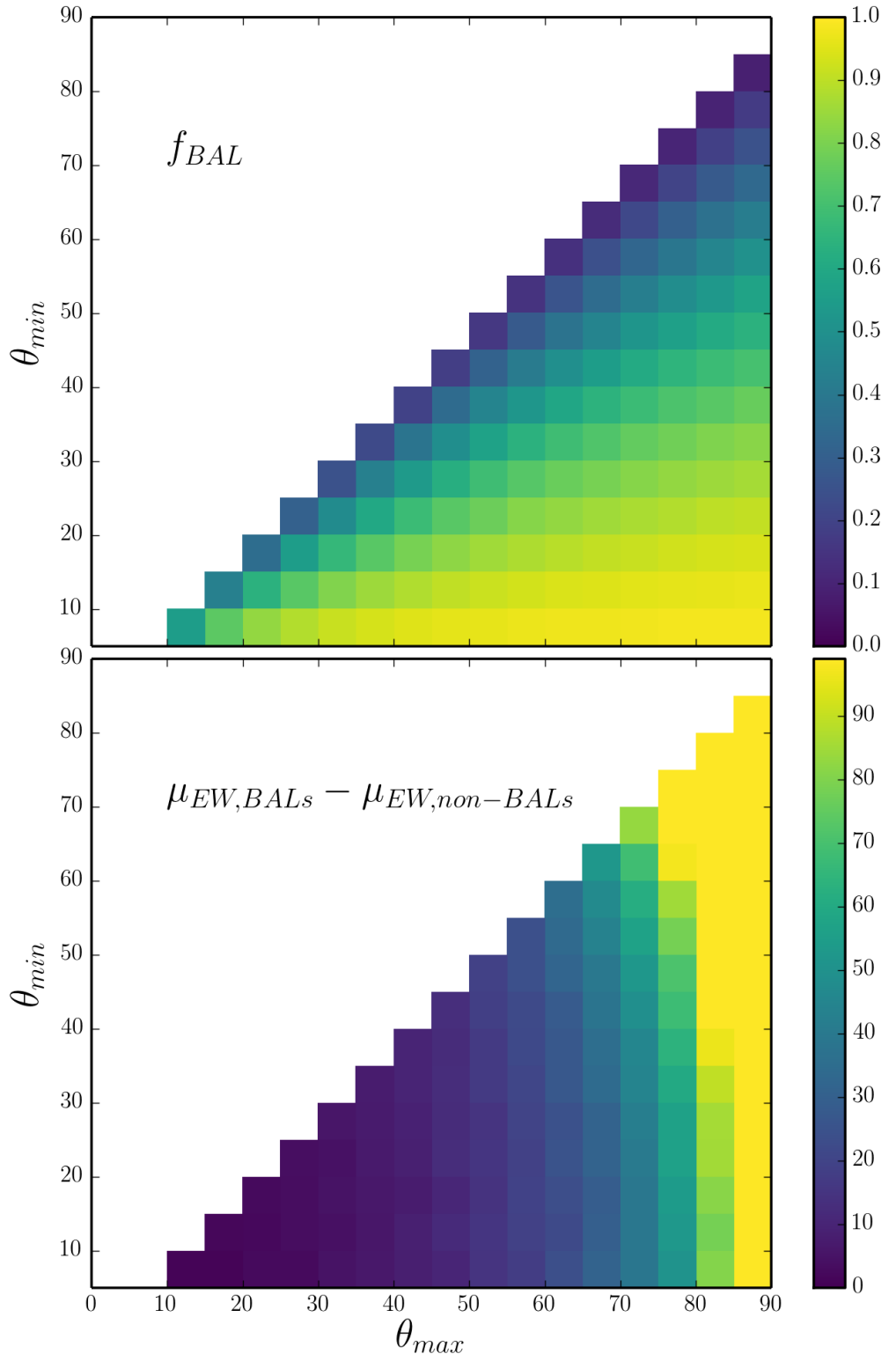


FIGURE 3.9: Contour plots from the Monte Carlo simulations.

Par. A	Par. B	$r_{corr,AB}$ (non- BALs)	$r_{corr,AB}$ (BALs)
$\log[\text{EW}[\text{O III}]]$	$\text{FWHM}[\text{H}\beta]$	0.14	0.18
$\log[\text{EW}[\text{O III}]]$	R_{FeII}	-0.51	-0.67
$\text{FWHM}[\text{H}\beta]$	R_{FeII}	-0.26	-0.42

TABLE 3.1: Eigenvector 1 correlation coefficients

is extendible to the broad emission lines, with the caveat that those lines are dipole transitions and so opacity effects can change the angular distribution of emission. I will now explore how the above results compare to other observations of quasars that are expected to probe system orientation.

3.5.1 Eigenvector 1

Eigenvector 1 (EV1) is a fundamental parameter space for AGN and quasars (Boroson & Green 1992; Sulentic et al. 2000; Marziani et al. 2001; Shen & Ho 2014). It relates the FWHM of H β , FWHM[H β], the relative iron strength, R_{FeII} and the EW[O III]. Both EW[O III] and FWHM[H β] have been used as orientation indicators, and so comparing the BAL EV1 distribution to the non-BAL EV1 distribution is particularly interesting.

Fig. 3.10 shows the quasar distribution from sample A in EV1 parameter space, with BAL quasars from samples A and B overplotted. (Shen & Ho 2014, hereafter SH14) propose that the main inclination driver in the parameter space is FWHM[H β], and that high inclination sources should thus cluster around a diagonal line from the lower right to upper left quadrants. Conversely, R11's analysis instead suggests that high inclination sources should cluster around high EW OIII widths. As EW[O III] and FWHM[H β] are very weakly correlated (Spearman's rank coefficient of 0.13), this means they should lie to the left of the parameter space. Inspection of the figure clearly shows that BAL quasars are not only found in one region of the EV1 parameter space.

In order to assess this more quantitatively, I have shown contours of quasar counts overlaid on the scatter plot. The contours correspond to the number of objects in each bin, where the bins are of size $\Delta R_{\text{FeII}} = 0.2$ and $\Delta \text{FWHM}[\text{H}\beta] = 500 \text{km s}^{-1}$. The percentage of quasars falling within the inner contour is 45%, whereas only 18% of BAL quasars fall in the space. Conversely, 24% of BAL quasars fall outside the outermost contour compared to 10% of non-BAL quasars. It would therefore appear that BAL quasars are

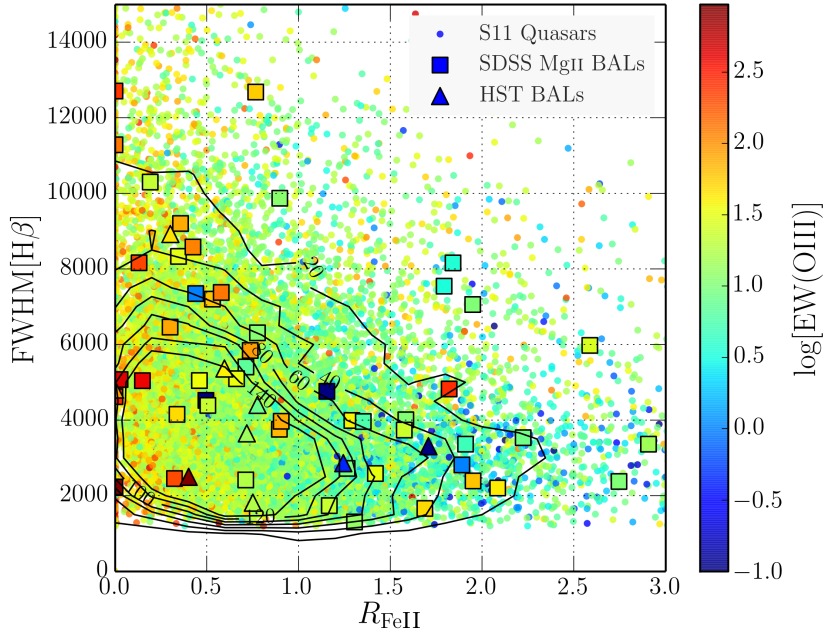


FIGURE 3.10: Eigenvector 1 for BAL and non-BAL quasars. FWHM of the $H\beta$ line plotted against the relative iron strength, R_{FeII} . The colour coding corresponds to the EW of OIII. The dots mark all quasars from sample A, while the squares mark those with Mg II BALs. The triangles show the HST BAL quasars from sample B.

preferentially clustered towards the high-mass and high-inclination end of EV1 space (under the interpretation of SH14). This is further illustrated by Fig. 3.11, which shows the LoBAL fraction in the same bins, compared to the mean LoBAL fraction. This is again suggestive of an overdensity towards the upper right of the parameter space. It is also clear that a unification picture in which BAL quasars are viewed exclusively from high inclinations is ruled out, under both the R11 and SH14 interpretations.

Larger datasets, preferably including HiBAL quasars with EV1 measurements, are needed in order to properly constrain the EV1 behaviour of BAL quasars. However, overall, the behaviour of $\text{FWHM}[\text{H}\beta]$ strengthens the above conclusion that BAL quasars are not always viewed from extreme inclinations.

3.5.2 Radio Observations

Fig. ? shows the equivalent width distributions in radio-loud quasars, split into core or lobe dominated. This designation is commonly used as an orientation indicator (Orr & Browne 1982; Wills & Brotherton 1995). Although th

In this case, we can see that A full investigation of this is beyond the scope

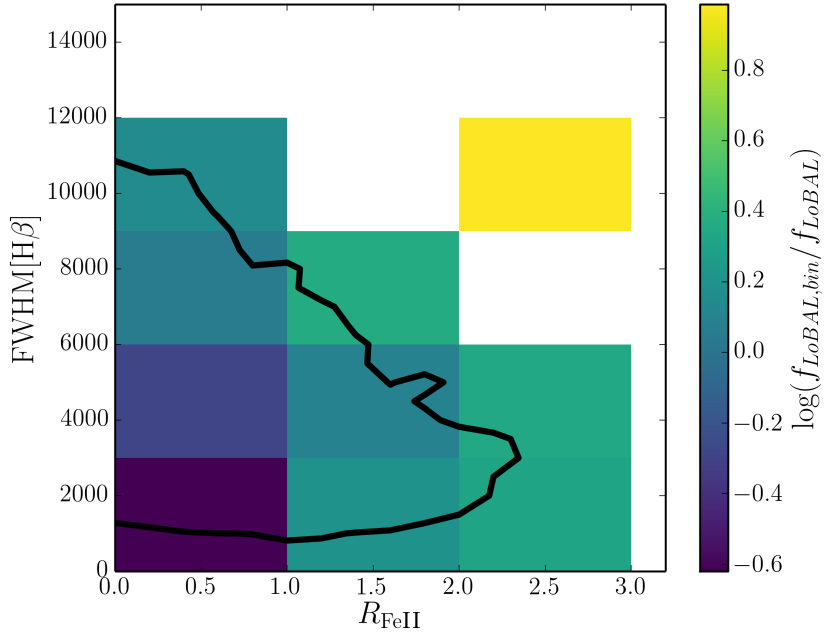


FIGURE 3.11: LoBAL fraction compared to mean LoBAL fraction in Eigenvector 1 space. The contour shows the outermost contour from Fig. 3.10 for reference.

3.5.3 Polarisation

Polarisation measurements of BAL quasars tend to show two properties. The first is a polarisation angle of $\gtrsim 60^\circ$ with respect to the radio jet axis in RL source (Brotherton et al. 2006). The second is a polarisation percentage of around 2.4 times greater, on average, than the non-BAL population. The polarisation percentages of a sample of BAL quasars from REF are compared to the Type I and Type II AGN populations from REF in Fig. 3.12.

The polarisation properties of BAL quasars offer some of the best insights into the geometries of BAL outflows, some of which appear to be in contrast with the conclusions drawn from emission line and radio properties.

3.5.4 Theoretical Considerations

Discuss Proga models: They tend to rise fairly equatorially (see eg. PK04) Talk to Nick?

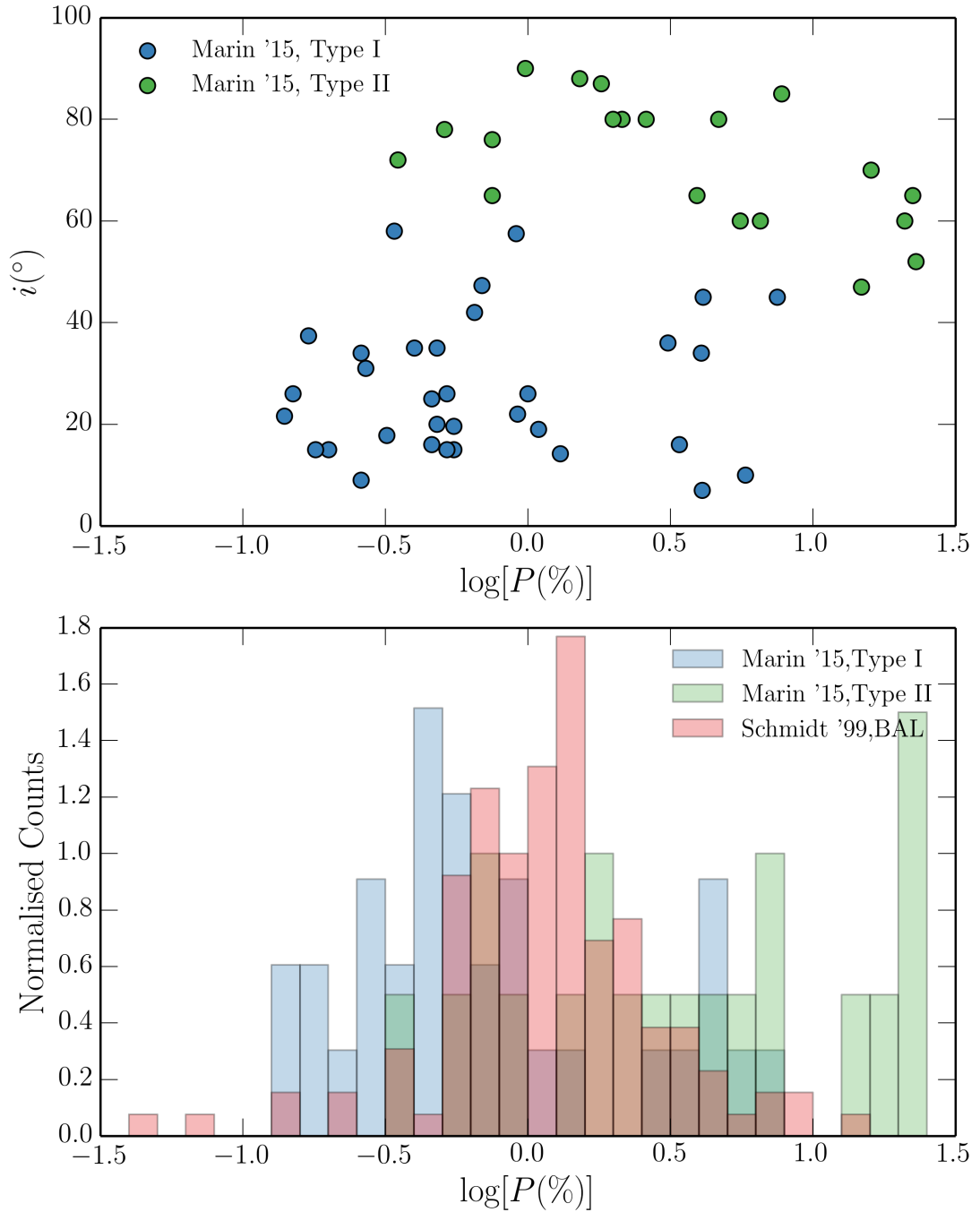


FIGURE 3.12: *Top:* Polarisation percentages as a function of measured inclination from Marin et al. (2015) for Type I and Type II AGN. *Bottom:* Histograms of polarisation percentages for BAL quasars from Schmidt et al. (1999) together with the Marin et al. (2015) AGN sample.

3.6 Conclusions

I have explored the emission line properties of BAL and non-BAL quasars and found that they are inconsistent with a unification picture in which BAL outflows rise equatorially from a foreshortened or limb darkened accretion disc. Based on these findings, it is possible to construct a few possible scenarios that are not ruled out by the above results. These conclusions have the caveat that I have assumed that conclusions drawn about LoBAL quasars can be extended to BAL quasars in general.

- *Scenario 1:* The quasar continuum is roughly isotropic, which is not expected from a geometrically thin, optically thick accretion disc. I have demonstrated that general relativistic effects cannot account for this discrepancy in the UV. Reprocessing by surrounding dense plasma with a large covering factor or limb brightening in the disc may provide possible explanations which this analysis cannot yet confirm or refute.
- *Scenario 2:* Quasar discs are strongly anisotropic, as expected from a geometrically thin, optically thick accretion disc. In this case, BAL outflows cannot only emerge at extreme inclinations and should instead be seen at very similar angles to non-BAL quasars. Polarisation measurements need to be reconciled with this hypothesis. I recommend that future RT modelling efforts explore different outflow geometries and that detailed polarisation modelling is undertaken to constrain the outflow opening angles.
- *Scenario 3:* The geometric unification model does not explain the incidence of BALs in quasars, or requires an additional component which is *time-dependent*, such as an evolutionary or accretion state origin for BAL outflows. In this scenario, BAL quasars would be seen from very similar angles to non-BAL quasars. However, the evidence for this is limited and there is no good model for why outflows would exist only for $\sim 20\%$ of a quasar's lifetime. Even if this is the case, then the covering factor of the outflow still needs to be constrained in order to estimate the BAL duty cycle.

Regardless of the conclusions about BAL quasars and their outflow geometries, this analysis allows conclusions to be drawn about the *overall* quasar population. In scenario

1, the EW[O III] distribution of quasars cannot be driven by inclination as suggested by (Risaliti et al. 2011). It is also clear from the work presented here that $\log R$, EW[O III] and FWHM H β are *cannot all* be reliable orientation indicators. Furthermore, if a geometric unification does explain BAL quasars, then absorption effects cannot be responsible for the observed EW[O III] distribution. The above conclusions each pose a different challenge to the current understanding of, respectively, accretion physics, polarisation measurements and geometric unification models. This work therefore adds to the growing evidence that our simplest models are not sufficient to describe the overall quasars and that alternatives should be sought.

Chapter 4

Conclusions and Future Work

“...and the credits rave as the critics roll.”

Mike Vennart, Silent/Transparent

I began this thesis with the fundamental tenet that accreting systems and their associated outflows are astrophysically important, but that much of the diverse phenomenology associated with such systems, as well as the underlying *physics*, is not well understood. Having attempted to address some of the issues raised in the introductory chapters, I will provide some concluding remarks. First, I will summarise my findings, before commenting on how future research can unveil the true nature of accretion discs and their winds.

A large portion of the time of this PhD has been spent maintaining, testing and developing the MCRT and ionization code, PYTHON. The first step in this thesis was

In the first study I demonstrated that accretion disc winds can have a profound impact on the optical spectra of CVs – a region of the spectrum often assumed to have nothing to do with outflows.

In chapter 5, I applied similar techniques to the question of quasar unification.

4.1 Suggestions for Future Work

4.1.1 CVs as Accretion and Outflow Laboratories

4.1.2 Improving the Treatment of Clumping

A few

4.1.3 Expanding the Capabilities of python

4.1.4 Obtaining Reliable Orientation Indicators

A wide variety of quantities have been used as AGN orientation indicators. However, many of these indicators are *model-dependent*, which is concerning given the lack of knowledge about the true origins of the multi-wavelength AGN SED. Furthermore, I showed in chapter 6 that it is not possible for EW[O III], FWHM[H β] and radio-core dominance to *all* be reliable orientation indicators due to the lack of the expected correlations between these measurements.

In order to distinguish between geometric unification, obscuration and evolutionary scenarios for the diversity of AGN it is critical to constrain their inclinations.

One of the conclusions presented in chapter 6, and also found from multiple studies (REFs), is that it is not possib

One possible way in which

4.2 Closing Remarks

Above all, this work demonstrates that *disc winds matter*. They are ubiquitous in accreting systems and appear to have a profound connection with the accretion process.

Bibliography

- Arav N., Becker R. H., Laurent-Muehleisen S. A., Gregg M. D. et al., 1999a, ApJ 524, 566
- Arav N., Korista K. T., de Kool M., Junkkarinen V. T., Begelman M. C., 1999b, ApJ 516, 27
- Beuermann K., Stasiewski U., Schwope A. D., 1992, A&A 256, 433
- Beuermann K., Thomas H.-C., 1990, A&A 230, 326
- Borguet B. C. J., Edmonds D., Arav N., Dunn J., Kriss G. A., 2012, ApJ 751, 107
- Boroson T. A., Green R. F., 1992, ApJs 80, 109
- Brandt W. N., Laor A., Wills B. J., 2000, ApJ 528, 637
- Brotherton M. S., De Breuck C., Schaefer J. J., 2006, MNRAS 372, L58
- Brotherton M. S., Tran H. D., van Breugel W., Dey A., Antonucci R., 1997, ApJ Letters 487, L113
- Capellupo D. M., Netzer H., Lira P., Trakhtenbrot B., Mejía-Restrepo J., 2015, MNRAS 446, 3427
- Dai X., Shankar F., Sivakoff G. R., 2012, ApJ 757, 180
- Davis S. W., Hubeny I., 2006, ApJs 164, 530
- Davis S. W., Woo J.-H., Blaes O. M., 2007, ApJ 668, 682
- de Kool M., Begelman M. C., 1995, ApJ 455, 448
- DiPompeo M. A., Brotherton M. S., Cales S. L., Runnoe J. C., 2012a, MNRAS 427, 1135

- DiPompeo M. A., Brotherton M. S., De Breuck C., 2012b, ApJ 752, 6
- Edelson R., Gelbord J. M., Horne K., McHardy I. M. et al., 2015, ApJ 806, 129
- Elvis M., 2000, ApJ 545, 63
- Eracleous M., Halpern J. P., 1994, ApJs 90, 1
- Filiz Ak N., Brandt W. N., Hall P. B., Schneider D. P. et al., 2014, ApJ 791, 88
- Frank J., King A. R., 1981, MNRAS 195, 227
- Gallagher S. C., Brandt W. N., Chartas G., Priddey R. et al., 2006, ApJ 644, 709
- Goodrich R. W., 1997, ApJ 474, 606
- Green P. J., Aldcroft T. L., Mathur S., Wilkes B. J., Elvis M., 2001, ApJ 558, 109
- Green P. J., Mathur S., 1996, ApJ 462, 637
- Groot P. J., Rutten R. G. M., van Paradijs J., 2004, A&A 417, 283
- Grupe D., Mathur S., Elvis M., 2003, AJ 126, 1159
- Hamann F., Chartas G., McGraw S., Rodriguez Hidalgo P. et al., 2013, MNRAS 435, 133
- Hamann W.-R., Koesterke L., 1998, A&A 335, 1003
- Hamann W.-R., Oskinova L. M., Feldmeier A., 2008, in W.-R. Hamann, A. Feldmeier, L. M. Oskinova (eds.), Clumping in Hot-Star Winds, 75
- Harrop-Allin M. K., Warner B., 1996, MNRAS 279, 219
- Hartley L. E., Murray J. R., Drew J. E., Long K. S., 2005, MNRAS 363, 285
- Hassall B. J. M., 1985, MNRAS 216, 335
- Higginbottom N., Knigge C., Long K. S., Sim S. A., Matthews J. H., 2013, MNRAS 436, 1390
- Hillier D. J., Miller D. L., 1999, ApJ 519, 354
- Hubeny I., Agol E., Blaes O., Krolik J. H., 2000, ApJ 533, 710
- Hubeny I., Lanz T., 1995, ApJ 439, 875

- Kaspi S., Brandt W. N., Maoz D., Netzer H. et al., 2007, ApJ 659, 997
- Knigge C., Long K. S., Wade R. A., Baptista R. et al., 1998a, ApJ 499, 414
- Knigge C., Long K. S., Wade R. A., Baptista R. et al., 1998b, ApJ 499, 414
- Knigge C., Scaringi S., Goad M. R., Cottis C. E., 2008, MNRAS 386, 1426
- Krolik J. H., Voit G. M., 1998, ApJ Letters 497, L5
- Kurosawa R., Proga D., 2009, ApJ 693, 1929
- Kurucz R. L., 1991, in L. Crivellari, I. Hubeny, D. G. Hummer (eds.), NATO ASIC Proc. 341: Stellar Atmospheres - Beyond Classical Models, 441
- La Dous C., 1989a, MNRAS 238, 935
- La Dous C., 1989b, A&A 211, 131
- Lamy H., Hutsemékers D., 2000, A&A 356, L9
- Laor A., Brandt W. N., 2002, ApJ 569, 641
- Lazarova M. S., Canalizo G., Lacy M., Sajina A., 2012, ApJ 755, 29
- Long K. S., Blair W. P., Davidsen A. F., Bowers C. W. et al., 1991, ApJ Letters 381, L25
- Long K. S., Wade R. A., Blair W. P., Davidsen A. F., Hubeny I., 1994, ApJ 426, 704
- Longmore A. J., Lee T. J., Allen D. A., Adams D. J., 1981, MNRAS 195, 825
- MacGregor K. B., Hartmann L., Raymond J. C., 1979, ApJ 231, 514
- Marziani P., Sulentic J. W., Zwitter T., Dultzin-Hacyan D., Calvani M., 2001, ApJ 558, 553
- Mathur S., Green P. J., Arav N., Brotherton M. et al., 2000, ApJ Letters 533, L79
- Matthews J. H., Knigge C., Long K. S., Sim S. A. et al., 2016, MNRAS
- Mihalas D., 1978, Stellar atmospheres /2nd edition/
- Morgan C. W., Kochanek C. S., Morgan N. D., Falco E. E., 2010, ApJ 712, 1129
- Muñoz-Darias T., Coriat M., Plant D. S., Ponti G. et al., 2013, MNRAS 432, 1330

- Murray N., Chiang J., Grossman S. A., Voit G. M., 1995, ApJ 451, 498
- Netzer H., 1990, in R. D. Blandford, H. Netzer, L. Woltjer, T. J.-L. Courvoisier, M. Mayor (eds.), Active Galactic Nuclei, p. 57
- Neustroev V. V., Suleimanov V. F., Borisov N. V., Belyakov K. V., Shearer A., 2011, MNRAS 410, 963
- Noebauer U. M., Long K. S., Sim S. A., Knigge C., 2010, ApJ 719, 1932
- O'Dowd M. J., Bate N. F., Webster R. L., Labrie K., Rogers J., 2015, ArXiv e-prints
- Orr M. J. L., Browne I. W. A., 1982, MNRAS 200, 1067
- Owocki S. P., Rybicki G. B., 1984, ApJ 284, 337
- Owocki S. P., Rybicki G. B., 1985, ApJ 299, 265
- Patterson J., Patino R., Thorstensen J. R., Harvey D. et al., 1996, AJ 111, 2422
- Prinja R. K., Ringwald F. A., Wade R. A., Knigge C., 2000, MNRAS 312, 316
- Proga D., 2005, in J.-M. Hameury, J.-P. Lasota (eds.), The Astrophysics of Cataclysmic Variables and Related Objects, Vol. 330 of *Astronomical Society of the Pacific Conference Series*, 103
- Proga D., Kallman T. R., Drew J. E., Hartley L. E., 2002, ApJ 572, 382
- Proga D., Stone J. M., Drew J. E., 1998, MNRAS 295, 595
- Reichard T. A., Richards G. T., Hall P. B., Schneider D. P. et al., 2003, AJ 126, 2594
- Ringwald F. A., Naylor T., 1998, AJ 115, 286
- Risaliti G., Salvati M., Marconi A., 2011, MNRAS 411, 2223
- Rutten R. G. M., van Paradijs J., Tinbergen J., 1992, A&A 260, 213
- Shakura N. I., Sunyaev R. A., 1973, A&A 24, 337
- Shen Y., Ho L. C., 2014, Nature 513, 210
- Shen Y., Richards G. T., Strauss M. A., Hall P. B. et al., 2011, ApJs 194, 45
- Sim S. A., Proga D., Kurosawa R., Long K. S. et al., 2012, MNRAS 426, 2859

- Smak J., 1995, ACTAA 45, 259
- Sulentic J. W., Zwitter T., Marziani P., Dultzin-Hacyan D., 2000, ApJ Letters 536, L5
- Trump J. R., Hall P. B., Reichard T. A., Richards G. T. et al., 2006, ApJs 165, 1
- Urrutia T., Becker R. H., White R. L., Glikman E. et al., 2009, ApJ 698, 1095
- Šurlan B., Hamann W.-R., Kubát J., Osokinova L. M., Feldmeier A., 2012, A&A 541, A37
- Walker M. F., 1963, ApJ 137, 485
- Weymann R. J., Morris S. L., Foltz C. B., Hewett P. C., 1991, ApJ 373, 23
- Wills B. J., Brotherton M. S., 1995, ApJ Letters 448, L81
- Yong S. Y., Webster R. L., King A. L., 2016, PASA 33, e009
- Zhang S. N., Cui W., Chen W., 1997, ApJ Letters 482, L155
- Zhou H., Wang T., Wang H., Wang J. et al., 2006, ApJ 639, 716